Université d'Ottawa · University of Ottawa

Université d'Ottawa · University of Ottawa

FACULTÉ DES ÉTUDES SUPÉRIEURES ET POSTDOCTORALES

FACULTY OF GRADUATE AND POSTDOCTORAL STUDIES

Éric DESFONDS

AUTEUR DE LA THÈSE - AUTHOR OF THESIS

M. A. Sc. (Electrical Engineering)

GRADE - DEGREE

Department of Electrical Engineering

FACULTÉ, ÉCOLE, DÉPARTEMENT - FACULTY, SCHOOL, DEPARTMENT

TITRE DE LA THÈSE - TITLE OF THE THESIS

Mueller Matrix-based system to Perform Opto-Electrical Characterization of Polarization-sensitive DWDM Photonic Integrated Circuits

T. Hall

DIRECTEUR DE LA THÈSE - THESIS SUPERVISOR

CO-DIRECTEUR DE LA THÈSE - THESIS CO-SUPERVISOR

EXAMINATEURS DE LA THÈSE - THESIS EXAMINERS

R. Gauthier

J. Yao

J.-M. De Koninck, Ph.D.

LE DOYEN DE LA FACULTÉ DES ÉTUDES SUPÉRIEURES ET POSTDOCTORALES

DEAN OF THE FACULTY OF GRADUATE AND POSTDOCTORAL STUDIES

MUELLER MATRIX-BASED SYSTEM TO PERFORM OPTO-ELECTRICAL CHARACTERIZATION OF POLARIZATION-SENSITIVE DWDM PHOTONIC INTEGRATED CIRCUITS

by

Éric Desfonds

B.A.Sc. Electrical Engineering, University of Ottawa, 2000

A thesis submitted to the

Faculty of Graduate and Postdoctoral studies of the University of Ottawa

in partial fulfillment of the requirements for the degree of

Master of Applied Sciences, Electrical Engineering

Ottawa-Carleton Institute for Electrical and Computer Engineering

2004

Your file Votre référence
ISBN: 0-494-01457-1
Our file Notre référence
ISBN: 0-494-01457-1

Desfonds, Éric (M.A.Sc. Elec. Eng.)

MUELLER MATRIX-BASED SYSTEM TO PERFORM OPTO-ELECTRICAL CHARACTERIZATION OF POLARIZATION-SENSITIVE DWDM PHOTONIC INTEGRATED CIRCUITS

Thesis directed by Canada Research Chair in Photonic Network Technology Dr. Trevor J. Hall

The implementation of a novel analysis system to characterize rapidly and accurately polarization-sensitive dense wavelength division multiplexing photonic integrated circuits is detailed within this document. The acquisition and subsequent analysis of passive optical insertion loss and absolute responsivity spectrum of MetroPhotonics Inc.'s products shall be discussed.

Polarization-maintaining fibers are typically manually calibrated and rotated to evaluate the performance of such devices under extreme orthogonal states of polarization, known as transverse electrical and transverse magnetic modes. This highly manual measurement technique has proven unsuitable for a mass production environment.

Device Mueller matrix terms used in conjunction with advanced analysis algorithms have been used to evaluate the performance of these devices for any desired state of polarization, with largely increased overall testing capacity, accuracy and repeatability.

Different novel analysis algorithms have been evaluated to isolate the orthogonal input TE and TM spectrum, while still providing the extremes of insertion loss and/or responsivity at each wavelength steps across the operating wavelength range.

The algorithms described herein to recover said spectra are novel as, to our knowledge, nothing equivalent has yet been reported in any scientific literature.

This technique has enabled the Test and Measurement group of MetroPhotonics Inc. to provide new insight in the polarization-dependent performance of different planar waveguide photonic integrated circuit products, while providing more accurate process related metrics to the fabrication and design groups. These efforts culminated in the delivery of fully calibrated MetroPhotonics SurePath™ portfolio products to customers.

À mon ange-gardien, mon grand-père, Ange-Albert Desfonds.

Acknowledgements

I would like to thank my supervisor, Dr. Trevor J. Hall, for his support throughout the production of this thesis. It is an honor to be a part of his research team, and I sincerely hope we can pursue further research projects together.

I would also like to acknowledge MetroPhotonics Inc.'s senior management. Allowing me to use this project for my thesis, even in such a highly competitive environment, demonstrates once more the vision of scientific innovation that had convinced me to join MetroPhotonic Inc. early on.

I would like to thank my colleagues from the Test and Measurement, Design, Fabrication and Assembly teams. The collective drive to solve technical problems and keep pushing the boundaries of optical integration has made every day an adventure.

Special thanks to Ted Somerville for giving me enough room to explore new ideas, Adam Densmore for verification experiments, Mike Ashman for making enlightened recommendations on writing a thesis, Nik Panter for making me laugh every day at work, and Kirill Pimenov for all of our challenging discussions on how to keep striving for further optimized numerical algorithms. All of your contributions remain invaluable.

Je veux aussi profiter de cette occasion pour remercier ma famille. Mes parents, Robert et Céline, ainsi que mon frère et ma soeur, Richard et Nancy, qui m'ont toujours soutenu et encouragé, durant toutes mes années d'études et de travail. Je veux aussi remercier ma conjointe, Claudia, pour son soutien durant la période de rédaction. Je vous aime tous plus que tout au monde et sachez qu'il m'aurait été impossible de poursuivre des études universitaires sans votre soutien. Je tiens à vous remercier du fond du coeur.

Contents

Tables

Table

Figures

Figure

Chapter 1

Introduction

The laser's invention in 1958 by Arthur L. Schawlow and Charles H. Townes of Bell Labs(40) is now recognized as the genesis of many scientific fields and multi-billion dollar industries. Originally aimed at probing the inner working of the infinitely small, the laser has revolutionized telecommunications.

Studied widely during the 19^{th} century, polarization of light had lost some of its luster in the scientific community. The generation of very intense and coherent polarized light by the laser forced physicists to reinvestigate fundamental optical phenomena. The new possibilities offered by the laser were quickly investigated and device concepts described in the scientific literature in the previous century now form the basis of many of the components still used today in modern optical systems.

With the advent of the all-optical Erbium-Doped Fiber Amplifiers (**EDFA**), in the late 1980's, a revolution within the optical telecommunications field began. It allowed for the vast deployment of multi-channel optical networks centered around the 1550nm low propagation loss window of high-quality modern glass fiber. This innovation made it possible to envision the widespread use of Wavelength Division Multiplexing (**WDM**) networks without the need for expensive electrical bit-rate dependent repeaters for each channel.

Optical component designers and manufacturers faced a new set of challenges as combining and separating multiple wavelengths required optical (de)multiplexers. The required accurate characterization of the crosstalk to and from adjacent WDM channels introduced new challenges for Test and Measurements (**T&M**) engineers and test equipment designers.

The measurement of insertion loss and centre frequency of individual filter channels was once deemed sufficient to fully characterize the performance of passive optical (de)multiplexers. More recently, the measurement of the influence of crosstalk of each individual channel upon all other adjacent channels has become essential as the number of channels within a single fiber link increases.

The desire to create even more complex components, designed to combine higher numbers of functions and channels in a single device. The integration of optical and electrical components into a single device became a significant goal and eventually a major milestone of opto-electrical component design. In a fashion analogous to the integration of functions in electrical Integrated Circuits (**ICs**), the concept of Integrated Optics has been termed for the production of Photonic Integrated Circuits (**PICs**).

Herein lies one of the most interesting challenges at the heart of many of the latest innovations in the optical components field. Only III-V semiconductor compounds, such as *InGaAsP/InP* and *GaAlAs/GaAs* have direct bandgaps corresponding to the WDM wavelength range of interest. These allow monolithic integration of active and passive functions on the same semiconductor chip.

These anisotropic compounds exhibit a relative permittivity or dielectric constant, ϵ, which varies as a function of the orientation of the electrical field of the Transverse Electro-Magnetic (**TEM**) wave traveling through them. This property makes them highly polarization dependent, or birefringent. This material property must be taken into account if the full potential of integration of active and passive functions can be fulfilled. Careful design must overcome this impact; The stochastic nature of the State of Polarization (**SoP**) of the different WDM optical signals in an optical communication system confirms the need for polarization-insensitive or polarization-compensated designs.

1.1 Objectives and scope

A novel approach used to efficiently perform optical and opto-electrical characterization of polarization-sensitive *InGaAsP/InP* DWDM PIC devices is discussed herein. Indium Phosphide (**InP**) and its associated ternary and quaternary semiconductor compounds are used by MetroPhotonics Inc. to fabricate unique PIC components. The measurement and analysis techniques presented herein can be adapted to other devices that show a clear polarization dependence, such as Arrayed-Waveguide demultiplexers (**AWG**), couplers, etc.

The diffractive echelle-grating is the main building block of all MetroPhotonics Inc. products. It allows large numbers of channels to be (de)multiplexed within a smaller chip area than other typical Planar Lightwave Circuit (**PLC**) (de)multiplexing technology. While the intricate epitaxial layer design and complex fabrication steps of PIC production remain very interesting topics, this thesis discusses the evaluation technique used to characterize their performance. This thesis also focuses on the measurement and analysis systems developed to provide accurate data to trigger design revisions and improve the performance of every generation of PIC products, while ensuring continued qualification of all semiconductor fabrication processes through statistical analysis.

The T&M group at MetroPhotonics Inc. performs different tests on dies and subassemblies throughout the production cycle, from die-level screening to final fiber-attached device calibration. The high-level of integration of passive and active functionalities found in MetroPhotonics Inc. products has forced the T&M team to bring forth innovative testing and analysis strategies.

1.1.1 State of polarization simulation engine

This thesis details the evolution of a new analysis approach based on a SoP-simulation engine, which enables the simulation of the spectrum for any desired incident SoP, by using the Mueller-matrix terms of the Device-Under-Test (**DUT**).

The measurement technique used to extract the DUT's Mueller matrix terms provides

Polarization Dependent Loss (**PDL**) spectra over a large wavelength range as first presented by Nyman *et al.* in (37), and since patented (17). This simulation engine uses the same Mueller matrix terms used to obtain the PDL spectrum to provide more insight into the polarization dependent performance of the DUT.

This research project originally and mainly aimed to isolate the optical spectrum of the two extreme orthogonal SoPs, often referred to as Transverse Electrical (**TE**) or horizontal electrical field, and Transverse Magnetic (**TM**), or vertical electrical field, modes. Different criteria were investigated to identify the most suitable and efficient algorithms to extract the spectra from the least amount of measurements required. Following the development of more advanced analysis tools, many other research projects have emerged from the combined deeper understanding and pervasive use of the Mueller matrix terms.

Passive optical insertion loss and absolute responsivity spectra were evaluated usin the SoP-simulation engine, allowing the most accurate calibration of MetroPhotonics Inc.'s SurePath Monitor™, a 43-channel DWDM power monitor for optical networks[1] . The different building blocks used to create such PIC Devices shall be discussed further in Section 2.3.

Determining the Polarization Dependent frequency (**PDf**) shift, which corresponds to the birefringence-induced centre frequency variations, remains the dominant reason to recover the TE and TM incident SoP spectra. The intrinsic birefringence, resulting from the overall boundary condition solution of the multiple epitaxial layers, must be carefully compensated to yield polarization insensitive components. More accurate and repeatable data was required to facilitate the optimization process of the polarization compensator design.

Results employed to fine-tune the polarization compensator design need to be less susceptible to operator fatigue and Polarization Maintaining (**PM**)-fiber calibration and extinction ratio limitations. More accurate PDL results were also desired to further help fine-tune the different fabrication process parameters of the compensator and overall device. New measurement techniques were required to answer these shortcomings of the PM-fiber measurement technique.

The fundamental assumption that these two orthogonal modes appropriately represent the extremes of performance of all building blocks of the overall device governs all design decisions. This assumption is common for ridge- and slab-waveguide Planar Lightwave Circuit (**PLC**) designs. Since the propagation loss for a waveguide or the absorption coefficient of a waveguide-photodetector differs for TE and TM incident SoP, and the performance for other SoPs can be obtained via linear combinations of the original TE and TM performance characteristics. The need to obtain the DUT response for incident TE and TM modes clearly becomes essential.

Implementation of software capable of simulating any desired SoP alongside different evaluation criteria, and software capable of finding the extreme orthogonal SoPs helped to address these needs. These criteria, while currently optimized for ridge-waveguide based devices, can be adjusted for other types of components or other parameters of interest. More detailed investigation of the polarization sensitivity of different performance-related parameters[2] becomes possible and more insight into the performance of the different PIC products is now available.

[1] For more details on MetroPhotonics Inc.'s SurePath™ portfolio, please consult Appendix E, which includes application notes and product bulletins.

[2] For a detailed list of optical and opto-electrical parameters, consult Appendix B.

1.1.2 Techniques to isolate the orthogonal TE and TM spectrum

Two main techniques were evaluated to isolate the overall DUT TE and TM spectrum. The first technique is based on the conventional use of Mueller calculus, which involves sampling a large number of incident SoPs, where each SoP represents a point on the Poincaré sphere. For each of these points the output insertion loss or responsivity spectrum is simulated. From the resulting simulated spectra, specific parameters, such as centre frequency and insertion loss, can be evaluated. As will be shown in Chapter 4, the extreme values of these two parameters can be used to isolate the TE and TM modes.

The second technique focuses on numerical optimization methods. This technique is designed to determine the most different set of orthogonal Stokes vectors found on the surface of the Poincaré sphere. This optimization approach does not rely on performance parameter definitions, instead only the spectra simulated using acquired Mueller matrix terms are used to isolate the TE and TM modes. The absence of any performance parameter evaluation greatly reduces the burden of lengthy calculations. This technique insures orthogonality of the Stokes vectors corresponding to the TE and TM solution.

By using eigenvalues and eigenvectors solving techniques, a novel numerical approach further reduces the problem of determining the TE and TM spectrum to solving a simple optimization problem, as discussed in Section 4.4. This method has proven very efficient in determining the TE and TM incident SoP, without the need to sample several individual incident SoPs upon the surface of the Poincaré sphere. This algorithm has demonstrated enough efficiency and mathematical simplicity such that it is considered for integration into the firmware of several test instruments.

1.2 Structure of document

The fundamentals of optical networking, polarization of light, an introduction to MetroPhotonics Inc.'s PIC building blocks, product fabrication and testing procedures are introduced in Chapter 2. This shall help the reader understand the challenges of testing throughout the production cycle of PIC products as well as the added complexity due to the integration of active and passive functions within the same DUT.

Chapter 3 will briefly discuss different measurement techniques. This Chapter introduces Mueller matrix terms and the Poincaré sphere in more details. It will show how the ratio of data acquired, as a function of testing-time, can be largely increased by using matrix-based polarization-dependent measurement techniques.

Throughout Chapter 4, the inner workings of the SoP-simulation engine, as well as the implementation of the different analysis criteria and numerical algorithms used to extract the TE and TM modes are detailed. Results shown using different visualization tools shall help the reader decipher the respective strengths and weaknesses of these analysis techniques.

Results from a sample of the typical verification experiments, will be presented in Chapter 5. These results will verify that the algorithms used to determine the TE and TM modes were sufficient. All MetroPhotonics Inc. devices are now characterized based on these techniques, henceforth several thousand device channels have been characterized since the inception of this approach. Both optical insertion loss, electrical photocurrent and resulting absolute responsivity spectra for different MetroPhotonics Inc. products have been analyzed and compared to other measurement techniques, for verification purposes. Results were also compared to design simulations of PDf to further prove the efficiency of these algorithms as they are found to match the predicted performance results. Testing reports from many of MetroPhotonics Inc.'s customers further gave credence to our novel measurement techniques. These customers include Tier-1 Telecom System Original Equipment Manufacturers (**OEMs**) and research groups, and Metrophotonics Inc.'s products have reached different levels of evaluation and integration into different subsystems.

Chapter 6 concludes by presenting many of the scientific innovations and contributions that resulted from this project. Also presented are some of the projects being considered to further enhance current software and hardware implementations that may be considered in the near future.

Appendices have been included to help streamline the main body of this document; included is a list of acronyms, the expansions of some of the mathematical equations, definitions for optical and opto-electrical spectrum-related parameters, LabVIEW software examples, and some of MetroPhotonics Inc.'s Product Bulletins and Datasheets.

Chapter 2

Fundamentals

This chapter outlines the fundamental concepts discussed throughout this document. Basic WDM optical networking concepts are introduced first, followed by a brief introduction of single-mode operation and design of opto-electrical components alongside the concept of polarization of light; these concepts must be kept in mind while reading more about the different building blocks used by MetroPhotonics Inc. to build integrated PIC devices, which in turn are discussed. A description of the different fabrication steps, testing requirements and challenges related to MetroPhotonics Inc. products concludes this chapter. These will show how novel measurement and analysis techniques are essential for large production volumes and must be flexible enough to be adapted to the DUT's evolution throughout its production cycle.

2.1 Optical networking

Optical fiber links have been in use since the late 1970's during which time they were used mostly in the same fashion as copper wires, with a single sender and receiver sharing a common physical link.

The same concerns optical network designers had then still remain. One of the most critical characteristics of an optical fiber is its attenuation as a function of distance and wavelength. This is shown in Figure 2.1, (29, Figure 1-7), for different generations of fibers. Early fiber fabrication techniques only allowed the use of the 800 to 900nm wavelength range, which is often referred to as the first window of operation of optical fibers. In this wavelength range, optical fiber communication links were only deployed over short distances, as attenuation averaged over 10dB/km limiting the distances that can be traveled upon an optical link with acceptable signal degradation and data recovery. Furthermore, since only Multi-Mode Fiber (MMF) was fabricated, the bandwidth of these optical fiber links was severely limited due to the high probability of intermodal dispersion and resulting intersymbol interference.

Enhancements in fiber fabrication techniques, namely reduction of the concentration of water particles and metallic impurities in the fiber material, enabled fiber manufacturers to reach new levels of attenuation in the 1100 to 1600nm wavelength range, with propagation losses now averaging around 0.2 to 0.5dB/km. This made possible the transfer of data over hundreds of kilometers without the need for optical amplification. Even with ultra-purifying processing techniques, water particles and associated hydroxyl ions subsist generating an absorption peak

Figure 2.1: Evolution of optical fiber attenuation

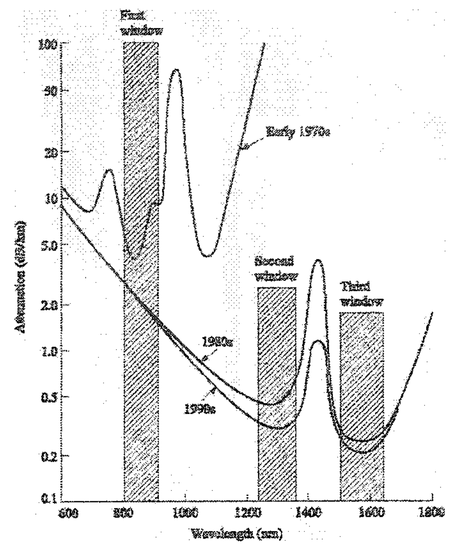

around 1400nm. This peak is present in most fibers laid out in current optical network builds. This attenuation peak separates the second and third windows of optical telecommunications.

As for microwave bands, letters have been used to identify these different operating windows. Table 2.1 shows their name and wavelength ranges. Current MetroPhotonics Inc. products are mainly used in the C- and L-bands to take advantage of the high-channel count capabilities of the echelle-grating demultiplexer and current market drivers.

Table 2.1: Optical fiber communication band designations

Letter	**Long format**	**Start λ**	**Stop λ**	**Type of communications**
O-band	Original Band	1260nm	1360nm	Single Channel CWDM
E-band	Extended Band	1360nm	1460nm	CWDM
S-band	Short Band	1460nm	1530nm	Future band for DWDM
C-band	Conventional Band	1530nm	1565nm	Current DWDM/CWDM
L-band	Long Band	1565nm	1625nm	Emerging band for DWDM

Prior to the deployment of all-optical fiber amplifiers, high capacity Time-Division Multiplexing (**TDM**) was the preferred scheme used for very high capacity links. It is still used to this day for Synchronous Optical NETworks (**SONET**), which handles most telephone networks currently in use all around the world. Whilst most data transmission rate records use a single channel, with very precise picosecond (**ps**) or even femtosecond (**fs**) optical pulse-widths multiplexed using precise timing electronics and assignment of individual time slots to different channels. These high-bandwidth scheme remain mostly used in research labs to this day, yet are slowly deployed where WDM may not be suitable.

The vast deployment of all-optical fiber amplifiers changed the cost associated with each wavelength or channel deployed. These allowed the removal of expensive electrical repeaters, also called **3R**-equipment (Repeat-Regenerate-Retime) for each individual data channel, to avoid data deterioration. Often placed after each 80 to 100km length of fiber, these expensive devices would convert the optical data streams back to the electrical domain, and regenerate a new signal. By avoiding the process of conversion from Optical to Electrical and back to Optical (**O-E-O**), all-optical amplifiers allowed the inclusion of many more wavelength in each fiber link where only one had historically been used in an economically sound fashion.

The inclusion of many more individual wavelength channels requires the use of an optical (de)multiplexer to combine into and separate from a single fiber. WDM greatly extends the bandwidth and capacity of the individual fibers. Coarse WDM (**CWDM**) and Dense WDM (**DWDM**) respectively represent farther or closer spaced channels in the wavelength domain and are common schemes used to combine multiple channels within a single fiber link.

Figure 2.2 shows a typical WDM communication scheme where four individual channels, each representing distinct data streams, are combined using a multiplexer (**Mux**). As these signals travel down the fiber link they are amplified through a chain of EDFAs until they are demultiplexed (**DeMux**) so that the individual data streams can be recovered.

Figure 2.2: Typical WDM communication scheme

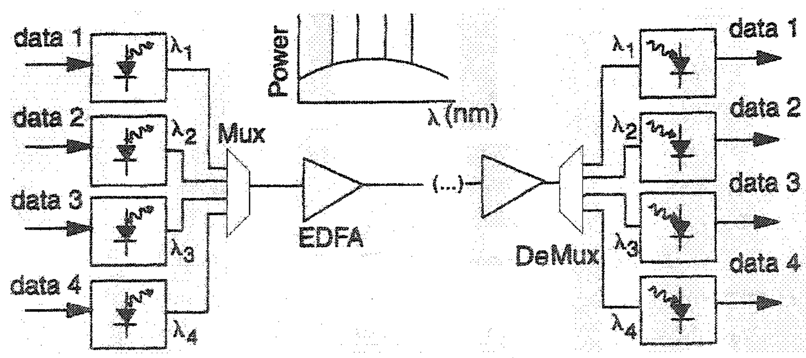

The efficiency of combining and separating the individual data streams at the transmitting and receiving nodes remains a fundamental problem for WDM optical network designers.

Clearly, WDM requires optical network architectures to be based around new design rules. Instead of using the copper wires philosophy, where a single cable would carry a single carrier signal, each fiber can potentially replace hundreds of copper wires. The optical fiber bandwidth had only begun to be exploited when using a single wavelength; the potential to share multiple channels over a single fiber holds the promise to end existing bandwidth-shortage issues.

2.2 Single-mode operation and polarization of light

The polarization of a lightwave is determined by the electrical field orientation, $\vec{E}$, of the TEM wave as seen in Figure 2.3, (29, Figure 2-2). The electrical field of the TEM lightwave is typically the only component of the lightwave detected by photodetectors used in optical telecommunications networks.

Figure 2.3: TEM wave representation

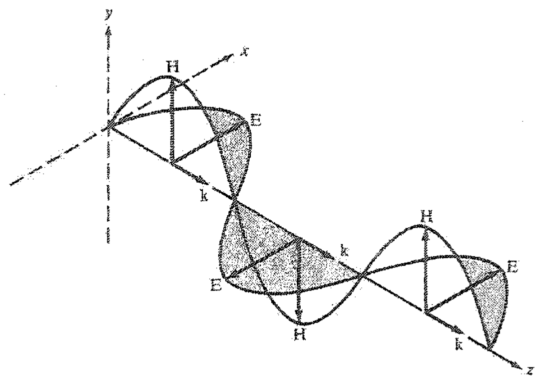

Modeling the light propagation through an optical component is based on wave optics and guided modes. Modes are three-dimensional electrical field configurations typically characterized by a single propagation constant related to wave velocity. A mode represents one of the possible solution to Maxwell's equations as a function of the different boundary conditions of the epitaxial layer design of the opto-electrical component waveguide or refractive index profile of an optical fiber, for example. Modes represent the various possible patterns of propagating or standing electromagnetic fields. Each is characterized by its frequency, SoP and electrical and magnetic field strengths, and depends on the refractive indexes, dielectric constants, magnetic permeabilities and the waveguide geometry.

Solutions to Maxwell's equations yield the electrical and magnetic fields of the TEM wave; A commonly used notation is the Linear Polarized (**LP**) approach. These modes are TEM waves in which both the electric and magnetic fields are perpendicular to the direction of propagation and in which the electric fields are oriented in one azimuthal direction only. Linear polarization being guided within MetroPhotonics Inc. products hence will be used to excite the DUT in our SoP-simulation engine.

Single-mode operation of all PIC building blocks is desired. The fundamental mode LP_{01}, also called TE_0 or TEM_{00}, is the first mode guided in such structures. The fundamental mode exists at any frequency, while higher-order modes may only propagate at frequency larger than the cut-off frequency, or shorter than the cut-off wavelength. The next higher-order mode, LP_{11}, is avoided by carefully optimizing the cut-off frequency of the fundamental mode. Figure 2.4 shows the fundamental and higher order modes propagating through a optical slab waveguide or optical fiber.

While a single mode of light can be guided by the MetroPhotonics Inc. devices, the orientation of the electrical field has an impact on the propagation of the lightwave. As light interacts with matter, the SoP of the incident lightwave influences the interaction of light with the matter in many fashions. As an example, the amount of light reflected at the boundary between two different materials is dependent on the SoP of the incident wave. A simple way to explore this involves a closer investigation of the index of refraction of the material, defined as the ratio of the speed of light and effective wave velocity of the lightwave within the material.

Figure 2.4: Fundamental and higher-order modes propagation

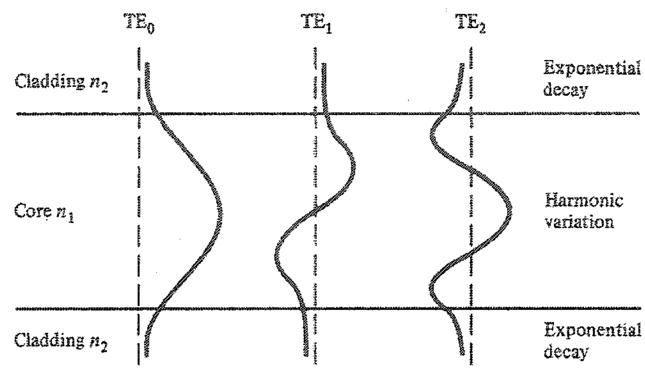

It is often quoted in terms of the electric permittivity or dielectric constant, ϵ, and magnetic permeability, μ, which is close to 1 in materials commonly used for fiber optic components design, hence:

$$n = \sqrt{\epsilon\mu} \cong \sqrt{\epsilon}$$

The index of refraction of anisotropic materials, such as InP, depends on the orientation of this electrical field. As seen in Equation 2.1, the general notation for the dielectric constant is a tensor. Thus the spatial orientation of the electrical field, $\overrightarrow{E}$, does impact the overall propagation characteristics within a given medium, by varying the net electrical flux density, $\overrightarrow{D}$, as governed by Maxwell's equation expressed in a dielectric material:

$$\begin{bmatrix} D_x \\ D_y \\ D_z \end{bmatrix} = \epsilon_0 \begin{bmatrix} \epsilon_x & 0 & 0 \\ 0 & \epsilon_y & 0 \\ 0 & 0 & \epsilon_z \end{bmatrix} \begin{bmatrix} E_x \\ E_y \\ E_z \end{bmatrix} \quad (2.1)$$

The orientation of the electrical field of this fundamental mode is thus used to define the TE and TM states of the individual building blocks and the overall DUT response. Throughout this discussion, the following definitions for the TE and TM modes will be used. A TEM wave with its electrical field component in the x-axis is TE, while if the magnetic field is in the x-direction it is a TM wave. Equivalently a magnetic field or electrical field in the y-axis direction indicated a TE or TM wave respectively. The z-axis points in the propagation direction of the TEM lightwave. Figure 2.5 shows the orientation of a TE (horizontal) and TM (vertical) mode within an optical fiber. The mapping used in MetroPhotonics Inc. devices will be discussed in Section 2.3.

While the cut-off frequency of the fundamental mode is carefully designed to allow a single-mode throughout the MetroPhotonics Inc. products, its propagation is affected by the variation in effective index of refraction as a function of the orientation of the electrical field. This implies that lightwaves of different incident SoP travel at different effective wave velocities. Linearly polarized light of TE or TM polarizations end up traveling at different speeds. The separation into two distinct polarization-dependent wave velocities is termed the inherent birefringence of the material.

Figure 2.5: Fundamental mode electrical field orientation

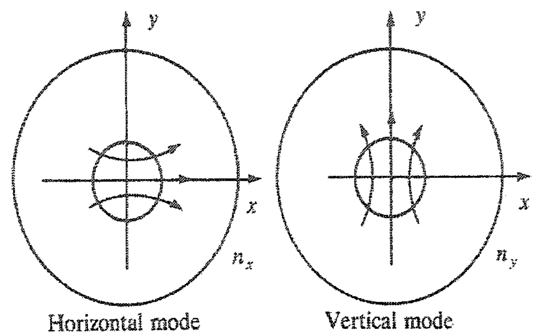

This impact must be counteracted if PIC products are to be made polarization-insensitive. All building blocks of MetroPhotonics Inc. PIC products are carefully designed to be as isotropic as possible. Each building blocks has a well defined axis of orientation with the fast and slow axes consistently at 90 degrees from each other by design. All structures also have their fast and slow axes aligned to each others. None of these rotates or changes the SoP within the device. The generally accepted assumption is that if a TE eigenmode is used to excite the DUT, the output light will remain of TE orientation.

The use of passive transparent ridge-waveguides typically yield asymmetric propagation modes. As shown in Figure 2.6 by the ellipsoid fundamental mode located under the InP ridge. This impact, alongside every other building blocks' influence, is cumulative and yields the overall DUT polarization-dependent response. The polarization compensator is used to compensate any TE and TM propagation difference throughout the DUT, yet the design of the waveguide structure aims to obtain the same mode field distribution for both orthogonal SoP.

2.2.1 Stokes vectors and Poincaré sphere

A very common method used to represent the SoP is the Stokes vectors, which are noted as $\begin{bmatrix} S_0 & S_1 & S_2 & S_3 \end{bmatrix}$. Each of the different terms of a Stokes vector represent the following:

- ▷ S_0, represents the intensity of the incident beam;
- ▷ S_1, reflects the tendency of the light beam to be either horizontally polarized, whereby $S_1 > 0$, or vertically polarized, whereby $S_1 < 0$;
- ▷ S_2, reflects the tendency of the light beam to be either linearly polarized at 45 degrees, whereby $S_2 > 0$, or linearly polarized at -45 degrees, whereby $S_2 < 0$;
- ▷ S_3, reflects the tendency of the light beam to be either right-handed circularly polarized, whereby $S_3 > 0$, or left-handed circularly polarized, whereby $S_3 < 0$.

The Poincaré sphere is a convenient graphical tool that represents polarized signals expressed as Stokes vectors in a three-dimensional real space. Figure 2.7 shows how these terms are simply matched to the x, y and z axis used in Cartesian notation. Any fully polarized light SoP

Figure 2.6: Ridge passive waveguide field distribution

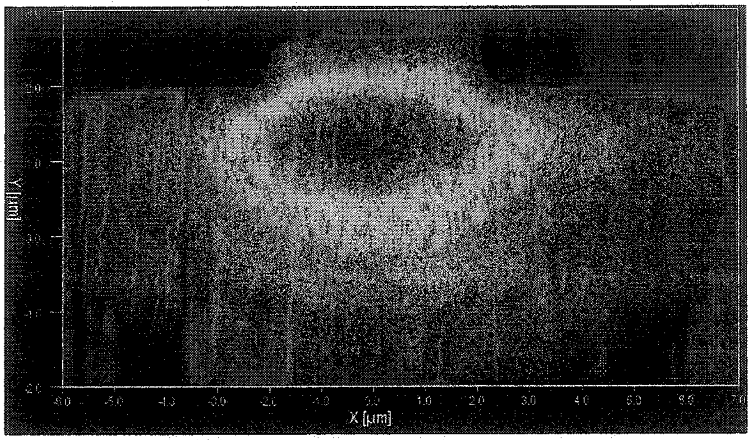

(a) Waveguide cross-section field distribution

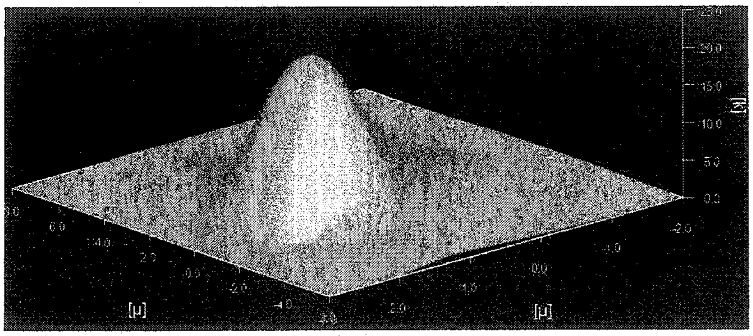

(b) Three-dimensional waveguide field distribution

Figure 2.7: Stokes vector representation upon Poincaré sphere

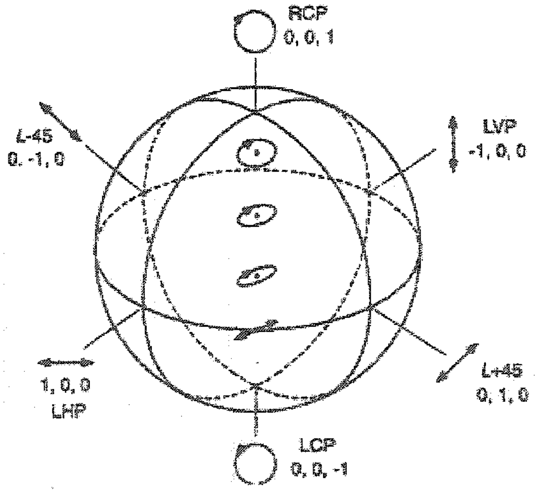

can be uniquely represented by a point on the surface of the Poincaré sphere. The coordinates of such points are the normalized Stokes parameters, S_1, S_2 and S_3.

The outer surface of the Poincaré sphere represents signals that are highly polarized such as the light produced by most lasers. Points located along the equator contain all of the linear SoPs, such as the TE and TM modes which correspond to the LHP and LVP SoPs in this figure. The poles and points between them and the equator represent circular polarizations and elliptical polarization states respectively.

Since optical signals are depolarized as they travel along the length of an optical fiber link, it is essential that all optical components found in their path have little performance degradation as a function of polarization. Consequently, each building block used to create PIC devices is optimized for incident TE and TM polarizations, as well as coupling between individual building blocks. This highly iterative process aims to obtain overall polarization-insensitive DUT responses.

2.3 Photonic integrated circuits building blocks

The substrate of all MetroPhotonics Inc. products is InP. The epitaxial layers grown atop InP substrate wafers are customized for the different building blocks required for the product to be manufactured. Each building block is interconnected with passive ridge waveguides or slab waveguides to other building blocks yielding the desired functionalities in the final PIC product.

While InP has increased optical transmission and coupling loss when compared to silica-based passive components, it does allow the integration of active components. InP and its associated compounds can be used to cover the full range of telecommunications wavelengths and allows the design of light sources, light detectors, light attenuators and light modulators. This section introduces the different building blocks and the technology required to (de)multiplex the different DWDM channels.

2.3.1 Grating-based multiplexer technologies

A (de)multiplexing device is required to add or remove wavelengths from the optical network fiber links while minimizing the impact to adjacent channels. The (de)multiplexing technology used in MetroPhotonics Inc. products is an echelle-grating (de)multiplexer, which shares the same diffractive operating principles as a free-space bulk grating. Figure 2.8 shows the SurePath Monitor™ demultiplexing the i^{th} channel by focusing it to the appropriate output waveguide.

The axes commonly used correspond to the following as seen in Figure 2.8, the x-axis goes from the top of the die to the bottom, while the z-axis goes from the left to the right (from the input waveguides towards the grating), and the y-axis goes into the page. It is common to, knowing the crystal orientation, re-arrange these axes while simulating different part of the device, but the overall mapping is as described earlier.

After the propagation of the λ_i lightwave through the input waveguide and diffraction through the slab waveguide region due to the reduced horizontal confinement, the echelle-grating reflects the incident lightwaves and creates precise phase-shifts resulting in spatial focusing as a

Figure 2.8: SurePath Monitor™ wavelength-demultiplexing schematic

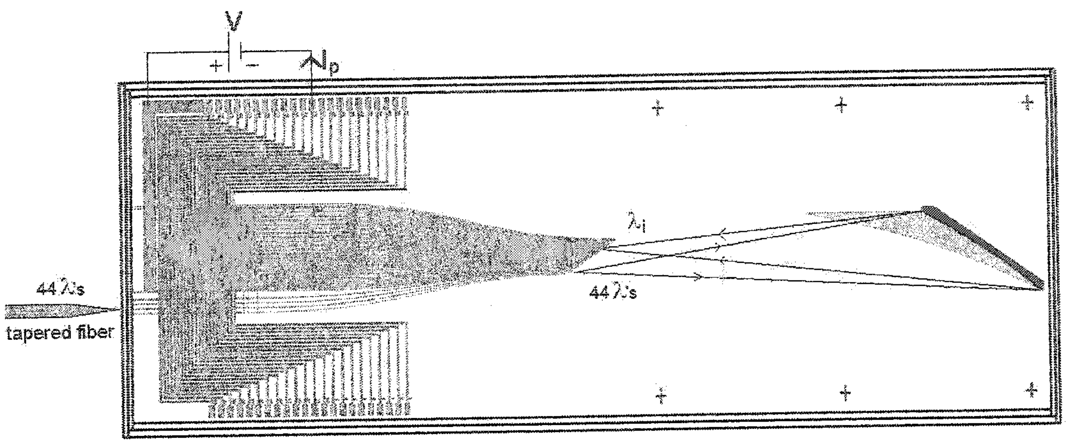

function of the incoming frequency. While based upon a Rowland circle spectrometer, the PLC-based echelle-grating has the added benefit that waveguides confine the optical modes, reducing crosstalk leakage. Tuning of the fabricated grating response involves only maintaining the slab waveguide area to a uniform temperature so that the λ_i channel is aligned to the desired output waveguide.

Phasars, also known as AWGs use many different waveguides to mimic the reflective and diffractive patterns created by echelle-grating devices. These cover much larger surface areas than echelle-grating based devices built from the same material, yet perform the same functions. The smaller size of MetroPhotonics Inc. dies offers some benefit in overall production costs, but more importantly in performance stability, as temperature uniformity across the slab waveguide is more easily maintained.

The goal of integrating an echelle-grating structure into PLCs is to apply the same type of diffractive action to telecommunication signals as echelle spectrometers used in astronomy to analyze deep-space light signals. Telecommunication WDM wavelength range involves the fabrication of precisely positioned grating teeth a few micrometers wide. As seen in the Scanning Electron Microscope (**SEM**) picture in Figure 2.9.

Figure 2.9: Echelle-grating etch

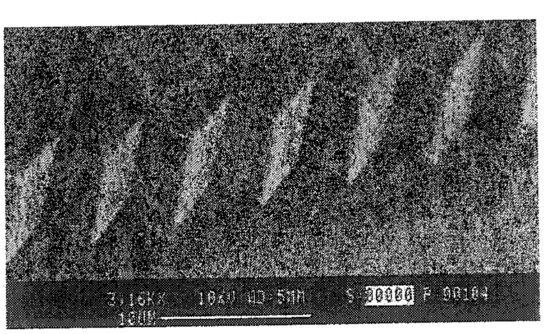

Both phasars and echelle-grating based devices demultiplex multiple wavelengths simultaneously, ensuring relatively the same insertion loss for each channel as the same diffractive effect is used for all incoming wavelengths. This parallel (de)multiplexing approach differs from discrete individual couplers or filters used for each individual channel, such as fiber Bragg gratings, for which losses add up as individual devices are added in a cascading fashion. The following review paper by Koteles (30) details the many advantages and issues related to integrated high-density etched grating-based (de)multiplexers, while design considerations of such components have been detailed by He *et al.* in (22).

Integration of passive diffractive gratings, waveguides, active detectors and/or attenuators within a single PIC device can replace multiple discrete components interconnected through fiber patchcords or lens coupling. Typically used within passive optical (de)multiplexers, MetroPhotonics Inc. focused on integrating echelle-grating (de)multiplexers with active building blocks.

2.3.2 Planar Lightwave Circuits building blocks

Non-symmetrical ridge waveguides in PLCs combined with the inherent anisotropy of InP introduces two clearly orthogonal optical modes, TE and TM. In the design of optical components, such as PLC devices, many variables must be taken into account to optimize the overall performance of the different integrated building blocks. This involves an intensive iterative process, where worse case scenarios are studied and summarized to predict the performance of the overall DUT.

Beginning at the epitaxial layer design, all building blocks are designed by taking into account the other building blocks to and from which light must be coupled. Test structures are designed and included in all fabrication runs so that almost all building blocks equivalent test structures can be sampled for Root-Cause Failure (**RCA**) analysis efforts. This design process becomes more complex when opto-electrical building blocks and their unique requirements are combined with passive functions to create PICs, hence test structures become even more essential to reach desired overall DUT response. The following are building blocks used in MetroPhotonics Inc. PIC devices, as shown in Figure 2.10. More in-depth details of individual building blocks and the overall design of the SurePath Monitor™ can be reviewed in the following papers (48; 51). The most relevant issues are discussed herein.

Waveguides and propagation loss

Propagation loss, single-mode operation and mode size of passive transparent waveguides remain major design concerns, as these are used to guide to and from individual building blocks within PIC devices. In an effort to create an appropriate propagation mode trade-offs are required to insure single-mode operation and allow efficient coupling from input fibers. More details on the design of waveguide-based devices can be found in (38).

Appropriate fibers have tapered cores and lenses to help compensated for the large difference in spot size between fiber cores and InP waveguides modes. It should be noted that the InP component fabricated by MetroPhotonics Inc. are small in size, other insertion loss contributing factors are predominant in the overall DUT insertion loss performance.

Figure 2.10: SurePath Monitor^{TM} die layout

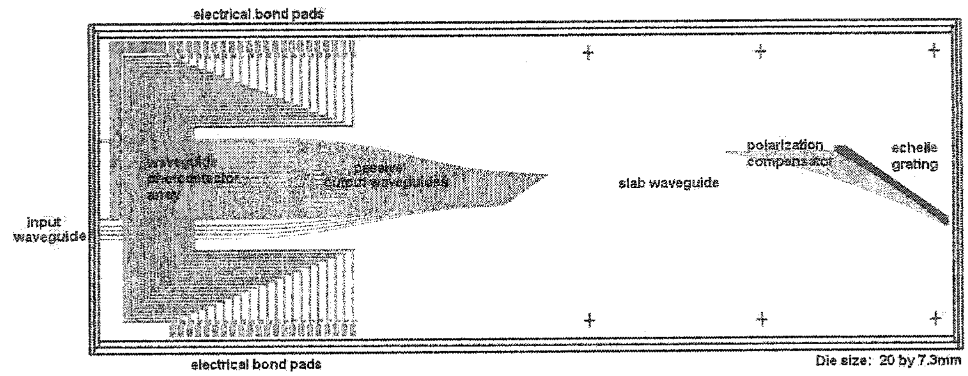

Record low loss for shallow etch ridge $InP/InGaAsP$ waveguides made possible by the very high-quality etching capabilities, which helped reduce the propagation loss in the 1550nm communication window to below 0.1dB/cm in any state of polarization(20).

Waveguide photodetector responsivity

The intrinsic waveguide photodetector responsivity remains highly dependent on polarization due to the asymmetric structure and supported optical mode. To facilitate alignment and coupling between passive and active waveguides, the active layers are grown atop the passive layers. The propagation mode is optimized so that different amounts of light enter the absorbing area of the waveguide photodetector structure as a function of the mode field distribution.

The absorption and confinement coefficients of the TE and TM modes are taken into account to ensure that the length of the absorbing layer is adjusted to fully absorb the orthogonal SoP having the lowest confinement and effective absorption coefficients, as a function of the specific product input power range of interest. This ensures very little variation in absorption for all incident SoPs, and yields acceptable overall DUT Polarization-Dependent Responsivity (**PDR**) performance. Figure 2.11 shows the difference in the supported optical mode for the passive and active waveguide photodetectors. The added asymmetry caused by the addition of active epitaxial layers explains the large difference seen in confinement and absorption coefficients for the TE and TM modes.

Details on the active and passive waveguide coupling approach preferred by Metro-Photonics Inc., as well as a review of the different associated building blocks may be reviewed in (12; 13; 47; 50).

Slab waveguide and its index of refraction

The main cause of PDf is the difference in the effective index of refraction in the slab waveguide area as a function of incident SoP. During propagation, TE and TM orientations see different effective indices due to the different layer boundary conditions and confinement coefficients. Henceforth both have different effective wave velocities.

Figure 2.11: Passive and active waveguide mode profiles

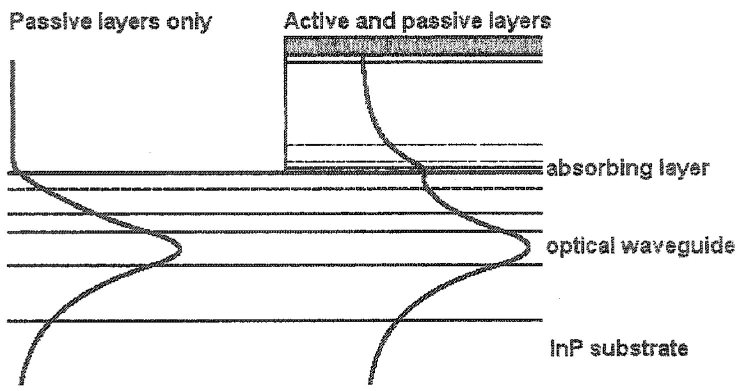

The consequence of this variation in wave velocities is noticeable by looking at the variation of insertion loss as a function of incident SoP. The overall spectrum of the TE and TM mode shows differences in the insertion loss for each frequency step and different centre frequency of their respective main filter lobe. No frequency conversion occurs, the center frequency of the main lobe, which is defined by the insertion loss as a function of frequency, will vary for different incident SoP. The presence of the compensator aims to make the path followed through the slab waveguide as closely matched as possible for the TE and TM modes, to obtain closer centre frequency results.

Temperature gradient-induced index variations or any stress affecting this area largely influence the propagation of these modes, and in the turn the overall PDf results.

Figure 2.12 shows a typical optical slab waveguide structure alongside its refractive index profile, which clearly shows the reduced horizontal confinement.

Figure 2.12: Optical slab waveguide structure

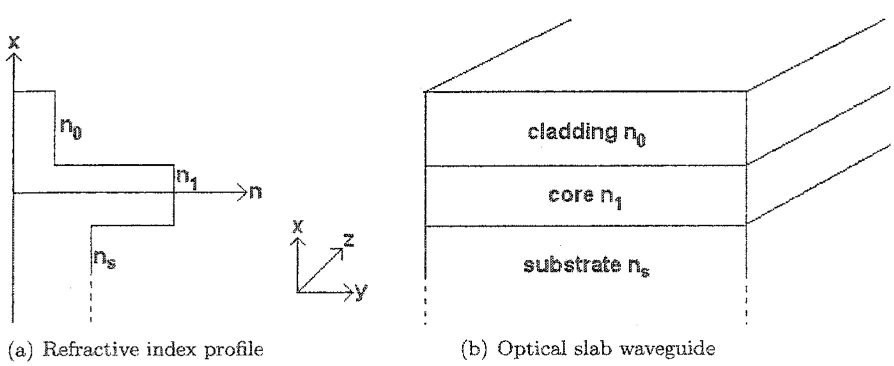

(a) Refractive index profile (b) Optical slab waveguide

Polarization compensator influence

The polarization compensator is designed to counteract the effective index difference and wave velocity difference in the slab waveguide. It is meant to compensate a large polarization dependent effect, hence it is itself highly sensitive to the incident lightwave SoP. The magnitude of the birefringence of the device, which corresponds to the difference in effective index for different SoP, is relatively large. Without quoting the effective indexes for each building block, its impact on PDf is commonly used to show its importance. Polarization-uncompensated devices typically show between 40 to 60GHz of offset between the TE and TM resulting spectra.

Its impact can be seen through the reduction of PDf to a more acceptable level. More details on the impact and design methodology of the polarization compensator can be found in (21).

Grating reflectivity and absorption

As with any other reflective surface there is a clear polarization dependence on reflectivity of the grating teeth. This must be quantified and taken into account for the compensator design to help reduce any additional PDL created by the difference in reflection and absorption as a function of the incident SoP.

While multiple designs have been explored, such as retro-reflecting InP unmetallized facets (23) or Au-covered InP facets for increased reflectivity, each show different results as a function of the polarization state of the incoming light. The extraction of the spectrum of the TE and TM modes was essential to perform RCA analysis of increased overall DUT insertion loss due to fabrication processes. Issues such as Ti-bonding and Au-thickness layer thicknesses have been evaluated by the comparison of the TE and TM spectrum.

Waveguide facet reflectivity and coatings

The input port facet suffers from the same issues as the grating although, in this case, minimized reflectivity and maximized transmission is desired. Optical return losses of -40dB are typical and desirable to avoid damage to components in the return optical path. Anti-reflection (**AR**) multi-layered coatings are typically used to minimize the polarization-dependent coupling loss from tapered fibers to the input waveguides. Their absence has clearly been a factor in obtaining more accurate results at die-level screening as etalons and wavelength-dependent standing wave artifacts could be observed in the measured spectrum of the DUT. These artifacts affect the accuracy of the centre frequency extraction.

2.4 Evolution of product and testing during production cycle

The following chapter discusses the strengths and weaknesses of the different techniques used for measuring polarization sensitive optical and opto-electrical components. To help the reader understand why some techniques were considered unsuitable for MetroPhotonics Inc. devices at different stages of their production cycle, additional details on the evolution of the SurePath Monitor™ product from die to final packaged device with attached fiber patchcord are included.

Starting with a bare InP substrate wafer, upon which epitaxial layers are grown to provide the desired functionality of MetroPhotonics Inc. product requirements. Wafers are processed using very precise multi-level lithography processes to selectively etch away different parts of the wafers to reveal the individual building blocks required to build the desired PICs. A few dozen devices can currently be fabricated on a single 4 inch wafer, during a single processing run. For more details on the fabrication steps involved, refer to (25; 26).

After processing and die cleaving, a die screening based on optical insertion loss is performed to remove devices which are expected to fail the overall responsivity and crosstalk performance specifications. Chosen dies are then attached to a ceramic carrier to help support them throughout the remaining assembly processes. Temperature sensors are also attached and wirebonded to the carrier to allow accurate temperature monitoring and control. This allows the device's spectral response to be aligned to the desired centre frequency plan. Figure 2.13 shows a SurePath Monitor™ die attached to a carrier, complete with temperature sensors. Bond pads and Au fan-out tracks on the die and carrier ease the probing of the p-contacts of the individual waveguide photodetectors integrated with the echelle-grating demultiplexer.

Figure 2.13: SurePath Monitor™ die on ceramic carrier

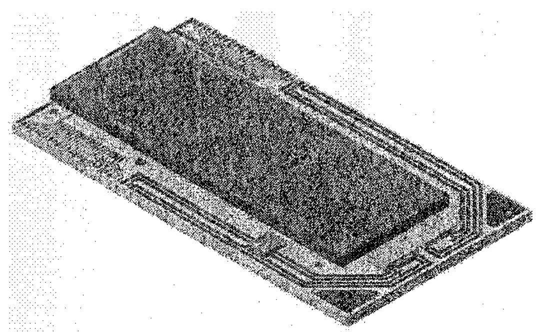

Both individual dies and dies on carrier lensed optical fibers, either PM or non-PM, can be positioned and aligned to the desired input waveguide to perform insertion loss and absolute responsivity measurements. Piezoelectric-driven positioners and precise probing equipment are required to meet the sub-nanometer (nm) alignment requirements and probing of the electrical bond pads on the carrier.

After screening the performance of the die on carrier, chosen devices are integrated into packages. A fiber patchcord is then aligned and firmly attached within the package to maintain proper alignment of the fiber. After filling the component with a combination of inert gases, a lid is attached, through a hermetic seal, to ensure stable operation over the expected lifetime of the product. As soon as a device is integrated into a package, no more passive testing is possible as the passive optical ports cannot be accessed anymore. Only responsivity measurements can be performed.

As soon as a fiber is attached no other fiber may be used to excite and characterize the device. Unfortunately, this does impact which measurement techniques can be considered as some of them require specialty fibers, such as PM-fibers, to maintain a known SoP up to the DUT input. All measurements of absolute responsivity now become relative to the input fiber connector rather than the power at the tip of the measurement input fiber.

Figure 2.14 shows both a SurePath Monitor™ after fiber attachment and as a finalized package with appropriate labels and heat sink.

Figure 2.14: SurePath Monitor^{TM} packaging

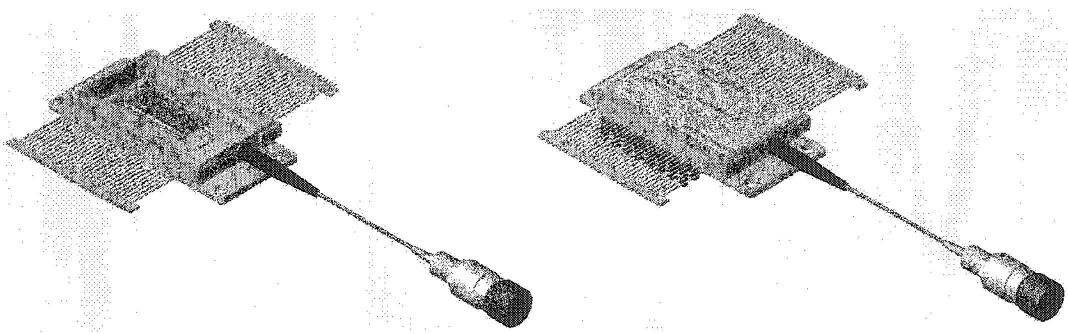

(a) Package after fiber attachment

(b) Completed package assembly

The desire to use efficient characterization techniques across the whole production cycle of the PIC devices became one of the main factors driving the system development described herein. This, of course, makes it easier to compare results at different stages.

The need to obtain the response for the incident TE and TM SoPs for both dies and completed packages, with results accurate enough to allow new levels of performance for optical network monitoring, also motivated the need for novel ideas to meet those demands. More details on the specifications of the SurePath Monitor^{TM} can be found in Appendix E.

Figure 2.15 on the following page shows the different stages of the production cycle of a SurePath Monitor^{TM} from a processed four inch wafer to a final packaged device. Additional comments on the testing challenges associated with each step are also shown. After each of these steps, a screening process complete with specific pass or fail criteria is used to determine if the subassembly can move along the production cycle or must be removed and quarantined.

Chapter 3 provides more details on the most common measurement techniques considered for MetroPhotonics Inc. products. This chapter also explains why only our Mueller matrix-based measurement and analysis system allowed measurements throughout the production cycle of the different PICs fabricated with sufficient throughput for production manufacturing volumes.

Figure 2.15: Evolution of SurePath Monitor™ from processed wafer to final package

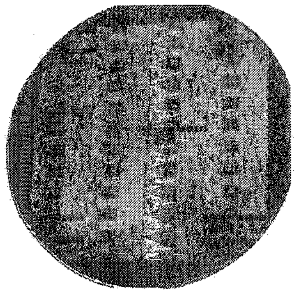

Wafer processing, some manual probing of individual dies may be accomplished to evaluate leakage/dark currents, through I-V curves measurements.

The next step involves cleaving of the wafer and anti-reflection coating of the facets and visual inspection prior to passing on to Test and Measurement group.

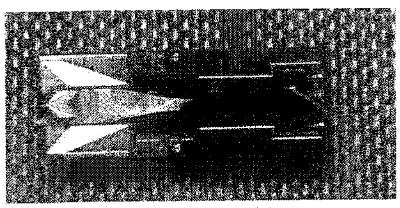

Die level testing is accomplished by stabilizing the device temperature to the nominal operating temperature.

Piezo controllers are used to align fibers to the nominal input port and passive output ports for performance screening of the optical passive elements.
(No responsivity data)

Sampling of I-V curves may be done on every 5th channel, if desired.

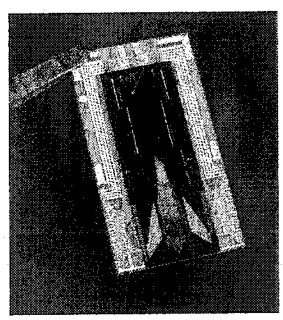

Dies are then attached to a ceramic carrier for added stability and to allow spreading out of the contact pads.

Wire bonding is then accomplished, as well as addition of two RTD elements for monitoring and control of the device temperature.

Full 44 channels responsivity spectra can be obtained, by aligning a single fiber to the appropriate input port to match the ITU grid, by using piezo controllers.
(Responsivity data only)

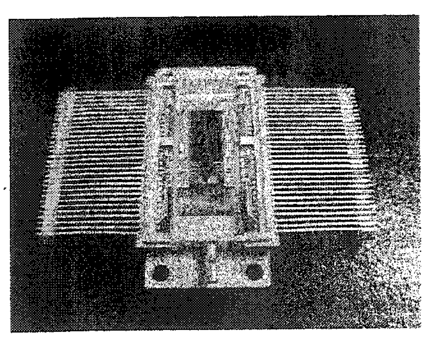

Wire-bonded chip-on-carriers are then integrated into packages and after an electrical continuity check, a fiber is attached to the device.

From this point on no fiber rotation or Polarization-maintaining fiber can be used, matrix-based approaches or polarization scrambler techniques are more suitable.

Full 43 channels responsivity spectra can be obtained.
(Responsivity data only)

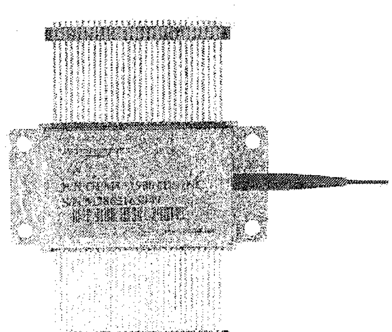

Package lid is sealed, burn-in testing is performed to avoid infancy death and final calibration reports can be created. Final temperature tuning to ITU grid is required at this stage.

Labeling and packaging for shipment is done and devices are placed in inventory.

Full 43 channels responsivity spectra can be obtained, as well as final temperature-tuning to the ITU-grid
(Responsivity data only)

Chapter 3

Measurement techniques

This chapter details some of the most common measurement techniques used to characterize the optical insertion loss and electrical response of optical and opto-electrical components. Four main techniques will be discussed alongside their strengths and weaknesses when the device performance is dependent on incident SoP. The required hardware and analysis steps required for the measurements are detailed herein. These techniques are the Optical Spectrum Analyzer (**OSA**) and optical power meter, polarization sampling, PM-fiber and the swept-wavelength polarization controller approach. It is from the later that DUT Mueller matrix terms are extracted. For definitions of typical optical and opto-electrical parameters, please refer to Appendix B.

3.1 Insertion loss measurement techniques

Accurate insertion loss measurements typically consist of the following three steps:

- ▷ calibration of the power reaching the DUT device ($P_{in}(\lambda)$ reference);
- ▷ insertion of the DUT into the optical path (addition of insertion loss from DUT);
- ▷ measurement of the optical power leaving the DUT (measurement of $P_{out}(\lambda)$).

The ratio of the reference and measurement results yields the insertion loss or optical attenuation in decibels (**dB**) as shown in Equation 3.1. Such relative measurements reduce the influence of any power fluctuations of the optical source, fiber or detector used by assuming the system remains relatively stable between the reference and measurement steps.

$$IL(\lambda) = -10\log\frac{P_{out}(\lambda)}{P_{in}(\lambda)}\ [dB] \tag{3.1}$$

Different device configurations largely influence how different measurement techniques are applied. Figure 3.1 shows different stages of testing for MetroPhotonics Inc. products, as discussed in Section 2.4. These stages include a calibration using bare-fiber or fiber patchcords, alignment to bare component with piezoelectric stages and fiber-attached measurements. For absolute responsivity measurements the use of a photocurrent meter complicates the calibration stage as fluctuations in the laser power are harder to compensate. More details on these responsivity measurement issues can be found in Section 3.3.

Figure 3.1: Different insertion loss measurement configurations

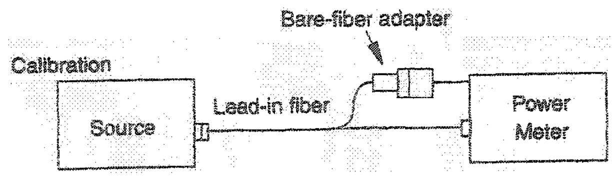

(a) Calibration measurement

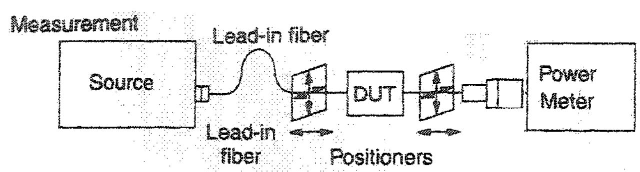

(b) Loss measurement with bare-fiber alignment to DUT

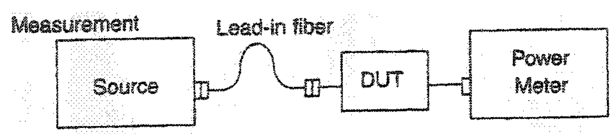

(c) Loss measurement with fiber-attached to DUT

Fiber alignment, or attachment precision, is crucial to any repeatable measurement and can be viewed as added uncertainty in the measurement results throughout the device production cycle. The aim to reduce these fluctuations through in-depth knowledge of the limitations of the test equipment and fiber types used will not be discussed in further details in this thesis, beyond issues already brought forth in Section 2.4.

3.1.1 Optical spectrum analyzer and/or optical power meter approach

The OSA measurement approach is one of the simplest and most commonly used insertion loss measurement techniques. An OSA is used to measure power as a function of wavelength. A normal OSA or power meter is used to capture the difference in resulting spectra between a reference measurement and a measurement after the introduction of a device into the optical path. In the OSA's case, much of the required analysis can be performed within the unit itself through calibration routines and built-in firmware algorithms.

Typical OSAs use mechanically rotated diffraction bulk-grating and free-space optics to perform wavelength filtering. These same concepts form the basis of the echelle-grating based demultiplexer, as discussed in Section 2.3.1. A schematic of a typical OSA based on a diffraction grating with a single slit aperture through which a photodiode collects the diffracted light can be seen in Figure 3.2.

A relative difference plot can be easily computed using two measurements. The first to one to obtain $P_{in}(\lambda)$ which can be stored on a modern OSA as a baseline reference and another to obtain $P_{out}(\lambda)$ after the addition of the DUT in the optical path.

Figure 3.2: Diffractive grating-based OSA schematic

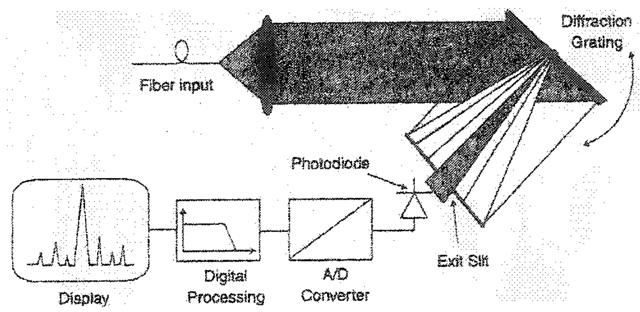

Typically a BroadBand Source (**BBS**) covering the desired wavelength span is used yielding a instantaneous result. The whole desired wavelength range can be excited and captured at once. The use of a BBS creates some considerable polarization dependent uncertainties. The generated light comes from Amplified Spontaneous Emission (**ASE**) and is typically not constant over time and highly incoherent in polarization. The observed measurement accuracy degradation lies in the fact that no *in situ* monitoring of the input power reaching the device can be implemented to compensate for such fluctuations.

Since the OSA spans a large bandwidth in every measurement, its ability to isolate minute changes related to the incident SoP is not so great. A trade-off between wavelength span and resolution must be taken into account. The number of points collected in a single scan is limited by the wavelength filtering capabilities of the OSA. These are a function of the bandwidth setting of the OSA and the photodetector used; *i.e.* the spacing between collected data points is increased if a large wavelength span is desired. Obtaining accurate results from an OSA requires in-depth knowledge of its limitation to accurately adjust these different settings as a function of the wavelength span of interest and the type of optical component being evaluated.

Failing to carefully adjust these settings has adverse effects on the measured filter shape of an optical (de)multiplexer. Modern OSAs aim to simplify the configuration steps by including programs optimized for different common types of components and applications in the OSA firmware. Yet, since even the simple task of measuring the output power and relative insertion loss involves complex integration and deconvolution algorithms to remove the impact of the diffraction grating's own filter envelope. Such results are commonly found to be inconsistent for different OSAs.

A single wavelength laser can be used to explore the performance as specific wavelength but will defeat the instantaneous snapshot capability of the OSA. A Tunable Laser Source (**TLS**) and power meter can be used in tandem to obtain single wavelength response. There is no more need for a diffractive grating as single wavelength can be measured at a time.

The OSA approach remains well suited for components which do not filter individual wavelengths nor require accurate polarization-dependent characterization. Such components should present a smooth variation of insertion loss as a function of wavelength. Examples of devices which may be characterized in this fashion are optical fibers, single wavelength filters or blockers, attenuators and isolators. These types of components are often tested at a single specific wavelength such as 1550nm for C-band components. From this result their overall performance may be inferred across the whole operating wavelength range with confidence gained through historical statistical analysis.

To further explore the polarization dependence performance of components, more accurate techniques and the generation of different incident SoPs are required. Such techniques are described in the following sections.

Table 3.1 summarizes the advantages and disadvantages of the OSA and optical meter approach.

Table 3.1: Summary of OSA/power-meter measurement approach

Advantages
Instantaneous response, full-wavelength response in a single measurement
BBS covers full range operating wavelength range
Only two measurements needed to obtain insertion loss spectrum
Well suited for wavelength insensitive components
Disadvantages
Trade-off between wavelength span and resolution; requires knowledge of OSA limitations
Incoherent source limits characterization capabilities and increases fluctuations in input power
No possible *in situ* monitoring of input power yields potentially increased error in insertion loss measurement
Complex algorithms to recover input power due to grating filter envelope influence

3.1.2 Polarization sampling approach

Two main polarization sampling techniques can be used: a direct-sampling and a mathematical-sampling approach. The sampling approach relies on the measurement of many incident SoPs to extract the desired performance parameters. Mathematical concepts using Mueller matrix calculus form the basis of the Mueller matrix-based system developed for this project, which is discussed further in Section 3.2.

A polarization scrambler can be used to allow multiple incident SoP to be sent to the DUT. A scrambler is designed to modify the SoP at its input to create all possible SoPs at its output, which can then be sent towards the DUT. A photodiode or photocurrent meter then records the values seen at the DUT output.

Polarization scramblers are often made of several motorized fiber loops. Each loop is driven by independent motors running at different speeds. This generates random output polarization states. Other configurations consist of individual waveplates rotated precisely along their fast axis to cover all possible SoP. These are often called polarization controllers as their output SoP is controlled instead of randomized. These will be discussed further in Section 4.2 on page 46. Both types are shown in Figure 3.3 on the following page.

From the maximum and minimum values of the measured output optical powers[1] at each wavelength, $P_{max}(\lambda)$ and $P_{min}(\lambda)$ expressed in linear terms, an extreme PDL spectrum can be

[1] To avoid confusion only optical powers and passive insertion losses are discussed in this section. These can be replaced by photocurrents or responsivity measurements for polarization dependent current or responsivity variation evaluation, if the optical receiver was replaced by a current sensor.

Figure 3.3: Typical configurations for polarization scramblers and controllers

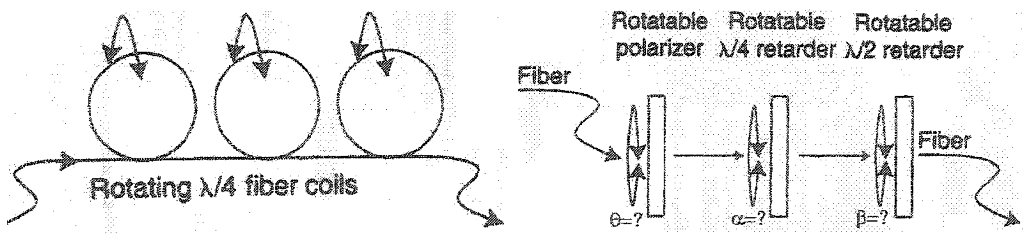

(a) Motorized fiber-loop polarization scrambler (b) Waveplate based polarization controller schematic

computed as shown in Equation 3.2:

$$PDL\left(\lambda\right) = 10\log P_{max}\left(\lambda\right) - 10\log P_{min}\left(\lambda\right) = 10\log\frac{P_{max}\left(\lambda\right)}{P_{min}\left(\lambda\right)}\left[dB\right] \qquad (3.2)$$

Figure 3.4 details a fiber-loop polarization scrambler measurement system. An optical receiver monitors the output power for extraction of the PDL for each individual wavelength PDL after the insertion of the DUT. The resulting insertion loss variation is also shown as different incident SoPs are sampled.

Figure 3.4: Typical polarization scanning setup and measurements of PDL

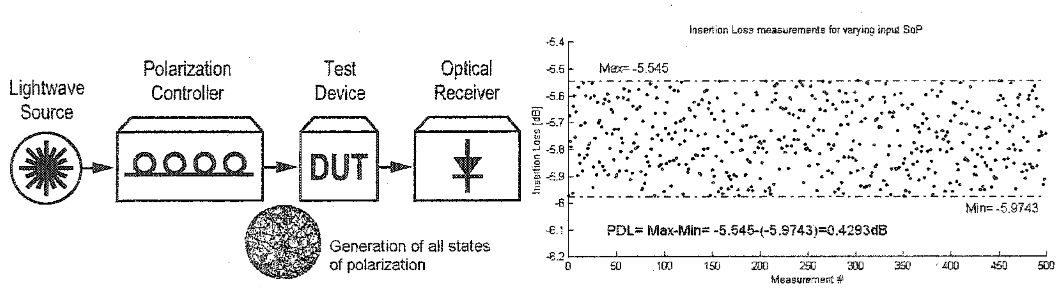

(a) Polarization scrambler measurement setup (b) Measured insertion loss variation

Sufficient knowledge of the scrambling efficiency of the polarization scrambler and the integration time, dwell time, and response time of the measurement photodiode or photocurrent meter are essential to obtain valid results. This is well suited for a component which can be characterized at a single wavelength, so that the performance over the whole operating range can be inferred. This approach has been documented and standardized in (45).

If a full spectrum is required it is best to capture a wavelength step at a time by using a TLS. For an optical filter performance test risks of fiber decoupling and potential DUT temperature fluctuations are omnipresent due to the longer testing time required. Trade-offs in wavelength step size may be considered to reduce the resolution outside of the main filter lobe while closer data points can be captured within the main lobe.

To ensure measurement accuracy, a constant input power should be delivered to the

DUT for all incident SoPs. This same assumption is required for the OSA approach. Including *in situ* monitoring of the output power of the polarization scrambler without influencing the measurement by adding optical splitters is complicated due to the polarization dependence of optical splitters and their splitting ratio.

This technique remains a stochastic approach; The measurement approach allow the extraction of the exact PDL only if an infinite number of SoPs could be individually sampled while being perfectly isolated from each other. This is not feasible. The generation of all possible incident SoPs is required to ensure the extremes of the parameter, under observation, are reached. The stochastic nature of such a measurement approach creates a new challenge. The challenge is to determine how much time is required to obtain accurate results considering the settings and limitations of the measurement equipment.

A parameter called the *maximum allowable error angle* on the Poincaré sphere, δ_{max}, is often quoted in polarization controller specifications to help resolve this dilemma. The relative PDL error, ΔPDL expressed in dB, can be computed as follows and is a function of the total absolute value of PDL:

$$\frac{\Delta PDL}{PDL} \cong -\frac{\delta_{max}^2}{2} \tag{3.3}$$

Substantial error angles can be allowed in accurate PDL measurements, as discussed in (14, Section 9.5.1). Typical polarization scrambler performance specifications result in an margin error of about 5% for about 10 seconds of sampling. The total PDL uncertainty is essentially calculated as the root-sum-square of the uncertainty of the contributing factors. Some instruments provide uncertainty specifications as low ± 0.003 to ± 0.005dB for measured PDL values of around 0.1dB

Specifications of these instruments are given as a function of typical measurement time and sensor settings. Common settings specified include the averaging and dwell time of the optical power measurement circuit. More advanced equipment such as PDL meters have built-in calibration data to ensure more accurate results by handling the settings of the internal sensors and polarization scrambling speed. More details of typical equipment used in such setups can be found in (1; 3).

Polarization independent optical power meters are also required. Many common designs of optical sensors are unsuitable for low PDL measurements. The detector's own PDR must be minimized to ensure no PDL artifact is included in the measurements. Polarization scramblers and controllers must accordingly have very low PDL to reach sufficient accuracy specifications. Measurement of the output power, while not scrambling the SoP, should be close to the output power while scrambling, as no efficient *in situ* power monitoring is possible.

The polarization scanning approach remains a very robust and accurate approach to determine the PDL of a device a single wavelength at a time. It is rather easy to implement as most available PDL meters provide both polarization scrambling and fast power meter sampling capabilities. The relatively long test time involved for each wavelength step makes this measurement method less suitable for optical components operating over large wavelength spans such as the SurePath Monitor™ product.

Figure 3.5 shows how under-sampling of the Poincaré sphere may occur while using a polarization scrambler. Measurement settings may result in averaging over large surface areas of the Poincaré sphere yielding data points which do not accurately represent the maximum and minimum insertion loss or PDL spectrum. Higher averaging of 100 instead of 20 points per wavelength step yields more accurate results, which more closely match the simulated extreme spectra as discussed in Section 3.2.3. Consequently the required measurement time is increased by a factor of five. Frequency step sizes can be varied as a function of the distance from the nominal centre frequency of the device to reduce the overall test time.

Figure 3.5: PDL spectrum measurement results with polarization scrambler

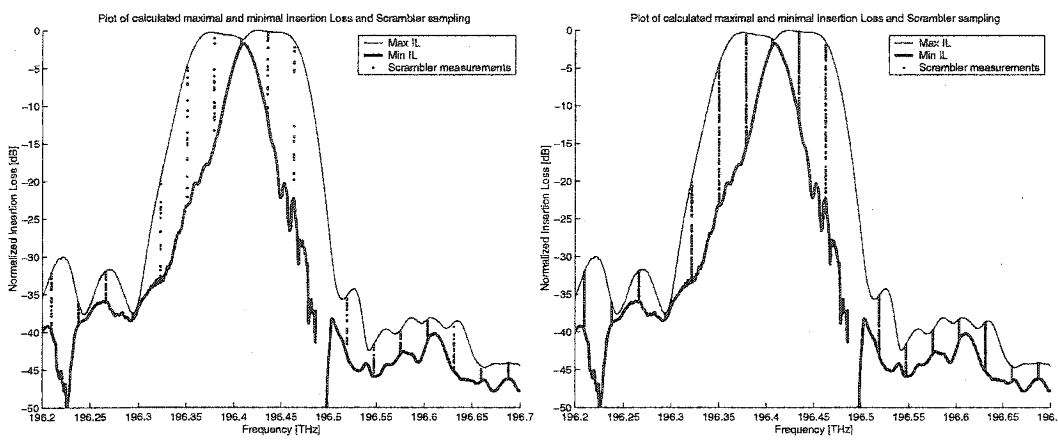

(a) Using 20 averages per frequency step

(b) Using 100 averages per frequency step

Apart from the extremes and average insertion loss results, very little additional data can be extracted from such data. Statistical analysis can be used to evaluate filter passband widths, centre frequencies, and PDf approximations given that enough data points have been taken within the main filter lobe. But, the measurement error typically remains rather large as does the lack of repeatability. This technique remains suitable for R&D-oriented test setups and calibration verifications, but unsuitable for testing at high-volume manufacturing levels for all these reasons.

The same basic sampling concepts shall be discussed further in Section 4.3, where they will be used to simulate the spectral response of a DUT for different incident SoPs. The same issues discussed here, namely the amount of points to be sampled and the related increase in simulation time, will be discussed further.

Table 3.2 summarizes the advantages and disadvantages of the polarization sampling approach.

3.1.3 Polarization-maintaining fiber approach

PM-fiber allows a linearly polarized lightwave to propagate with very little changes to its polarization state. It is mostly used for short interconnections between optical components or test equipment, such as between a TLS and a polarization-dependent modulator. They

Table 3.2: Summary of polarization scrambler measurement approach

Advantages
Potentially very accurate PDL results ($\pm mdB$)
Use of single wavelength coherent source
Automation of PDL measurement (only several seconds for each wavelength step)
Reference measurement of input power fluctuations possible (still no *in situ* monitoring)
Disadvantages
Slow measurement, only efficient for single wavelength measurements
Little parameters can be extracted with high accuracy
Stochastic approach influenced by settings of measurement system
Stochastic measurement entails risks of under-sampling of Poincaré sphere

have either non-symmetrical core or have strong internal birefringence caused by stress-applying members, which helps preserve the SoP even if additional birefringence is added through bending of the fiber. This birefringence breaks the circular symmetry of optical fiber, creating two principal transmission axes within the fiber, known as the fast and slow axes of the fiber.

Carefully calibrated these fibers can be used to measure the response of a DUT to known incident SoPs by rotation of the fiber itself. Typically TE and TM incident SoPs are used for PLC devices. Figure 3.6 shows different types of PM-fiber each with their own asymmetric index of refraction profile.

Figure 3.6: Different types of PM-fiber

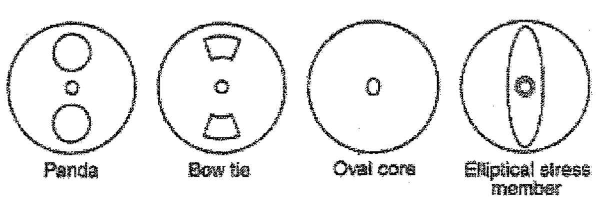

MetroPhotonics Inc.'s early PDf measurement techniques were based on an Agilent TLS capable of covering the complete wavelength operation range of interest with steps as low as 5 picometers (**pm**) in a sweeping fashion. Due to a memory limitation of the Agilent mainframe only four thousand points per sweep can be captured and stored for later recovery.

The mainframe having built-in photodetectors modules was capable of synchronizing the power measurements with the wavelength sent to the DUT, consequently greatly reducing the time required to cover large wavelength spans. Unfortunately, the mainframe memory limitation renders a full C-band scan impossible with a 5pm step. The wavelength span of the different measurement is limited since the smallest wavelength step is desired to ensure that the most accurate PDf measurement. More details on the computation of theoretical error for such extracted parameters are available in Appendix C.2. Agilent had no plans to offer direct photocurrent measurement modules which would have allowed photocurrent or responsivity measurements hence this technique was only used for optical insertion loss measurements.

To perform the PDf measurement a tapered lensed PM-fiber is first connected to the output port of the TLS and immobilized to ensure the calibrated incident SoP is not influence by fiber displacement or strain induced to the fiber core. This fiber is placed into a graded rotating chuck and then positioned at an approximate distance corresponding to the lens focal length from a polarizing beamsplitter cube. An accurate calibration of the rotation angles required to obtain TE and TM mode outputs can thus be performed if the fiber is rotated while the output intensity through the beamsplitter is monitored. Beamsplitters only let through a single linear incident SoP, and deflect the other orthogonal SoP content of the incident light. Typically used to separate the TE and TM content of an unpolarized beam polarizing beamsplitters split the incoming light into two orthogonal linearly polarized lightwaves. The incident horizontally-polarized light is transmitted, while the vertically-polarized light is reflected, both with negligible absorption.

Figure 3.7 shows how a polarizing beamsplitter can be used to isolate the horizontal and vertical component intensities. Rotation of the input PM-fiber increases the ratio of one component to the other detected at one of the outputs of the beamsplitter. Maximized transmission indicates that the rotation angle required to obtain one of the orthogonal incident SoP has been found.

Figure 3.7: Polarized beamsplitter iterative calibration setup

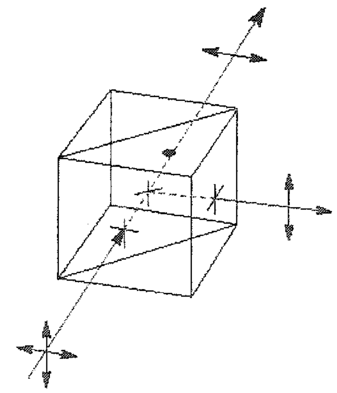

An iterative calibration technique, meant to optimize the rotation of the chuck, which maximizes the transmitted power through the beamsplitter enables the operator to calibrate the TE or TM incident SoP. This iterative process can only effectively be performed at a single wavelength as it remains highly time consuming. Once these optimized rotation angles are known, the tapered fiber can be repeatedly aligned to the input of the DUT so that a measurement with a known incident SoP is possible. The wavelength sweep and data acquisition process can be initiated after an alignment of a second fiber to the desired passive optical waveguide.

This measurement is performed for one incident SoP at a time: TE first, TM second, or vice-versa. For each incident SoP the centre frequency is extracted from the obtained spectrum so that a PDf value can be computed; *e.g.* the difference between the centre frequencies of the TE and TM polarization states corresponds to the PDf value. The actual TE and TM modes being measured the sign of the PDf can be taken into account.

The operator must perform two wavelength sweeps for each output waveguide. Between each step the output fiber must be realigned to the next output waveguide to measure the next TE or TM spectrum. Otherwise, the input fiber must be rotated and realigned to excite the same output waveguide under the remaining orthogonal incident SoP. Realignment of the fibers is essential to ensure optimal coupling efficiency for each of the measurement steps and involves some fiber handling and disconnections.

This technique offers many advantages. One of the most obvious being that the TE and TM modes are directly measured hence the sign of the PDf is known and their spectra are known. The over- and under-compensation of the inherent birefringence by the polarization compensator can be more directly evaluated in this case. Since photodetectors modules are integrated with the TLS in the same mainframe wavelength sweeping is possible instead of wavelength stepping which offers the potential to greatly increase the speed of test. While sweep rates of up to 40nm/s can easily be achieved with typical TLS systems, the speed of acquisition is dwarfed by the time required to align and rotate the input and output fibers. The memory limitation also entails larger rounding-errors as linear interpolation is used to recover more tightly spaced points. This affects the accuracy of the extracted centre frequency for each spectrum or reduced wavelength spans must be used to compensate.

The iterative fiber rotation calibration process remains time consuming and highly dependent on the patience and skills of the operator. This free-space alignment requires many steps to obtain accurate results. While this could potentially be automated through a polarization controller and calibration algorithm, the fiber itself may not maintain the same calibration over time due to environmental variations, fiber patchcord movement, fiber disconnections due to cleaning. This has a direct impact on repeatability of the measurements.

This calibration can only be done efficiently at a single wavelength. The extinction ratio of the TE and TM modes of typical PM-fibers averages around 15 to 20dB and is often wavelength dependent. This implies that some leakage of the TE mode towards the TM mode will be apparent as a function of wavelength and vice-versa. This leakage is minimized at the calibration wavelength. The high isolation of the MetroPhotonics Inc. DUT entails that a pure spectrum cannot be obtained over the complete dynamic measurement range of the photodetectors. The combination of the wavelength dependence of the extinction ratio of the PM-fiber and the fact it is typically lower than the DUT crosstalk levels returns erroneous spectra.

This measurement technique requires two alignments steps for each output waveguide which severely impacts the testing capacity. This also impacts the overall accuracy of PDf and PDL in many ways. First off, the measurement of the TE and TM spectrum may occur at different times, which increases the probability of different DUT temperatures and less accurate or repeatable centre frequencies results. Different coupling efficiency due to fiber lens eccentricities may be seen as artificial PDL artifacts. These issues create repeatability concerns, as well as increased fiber handling and potential fiber damage due to the required calibration and alignment steps.

For an early MetroPhotonics Inc. device which had six optical ports to be tested the average testing-time was about an hour. Even after many hardware and software optimizations. This yielded an average of ten minutes to capture both TE and TM for each optical port.

Another fundamental issue resides in the fact that no PM-fiber can be used in the final assembly. Furthermore, once attached the input fiber patchcord cannot be rotated at all. This creates undesirable confusion if measurement results are compared before and after fiber attachment as the coupling efficiency is different for different fiber lenses and fiber types, hence the overall insertion loss or absolute responsivity are different.

Table 3.3 summarizes the advantages and disadvantages of the PM-fiber measurement technique.

Table 3.3: Summary of PM-fiber measurement approach

Advantages
Actual TE and TM spectra measured, hence PDf results have valid sign not absolute terms
Wavelength sweeping enables faster data acquisition
Disadvantages
Extinction ratio of PM-fiber entails leakage of TE into TM mode spectrum, and vice-versa
Alignment and fiber rotation steps affect testing time, repeatability and accuracy
Calibration process highly dependent on skill set and patience of operator
Increased fiber handling and other environmental influence impact accuracy and repeatability
PM-fiber not used and fiber patchcord cannot be rotated in final package
Increased fiber handling and damage due to calibration and alignment required steps

3.2 Mueller matrix-based technique

Using similar hardware capable of wavelength sweeping and an appropriate polarization controller as described in the previous section, the insertion loss variation across all SoPs can be evaluated by extracting the DUT Mueller matrix terms instead of sampling many individual single SoP.

PDL measurement techniques based on matrix methods fall into two categories, *i.e.* those based on Mueller calculus, also known as Mueller/Stokes methods, and those based on Jones calculus. While these two techniques are mathematically equivalent for completely polarized light, only the Mueller method is applicable in the case of partially polarized light. Methods based on the Jones matrix also generally require known polarization states at both the input and output ports, while the Mueller method requires only known incident states, which reduces the complexity of the hardware required.

3.2.1 Mueller calculus basics

Mueller calculus allows the computation of the intensity and polarization of an incoming light beam after its transmission through an optical or opto-electrical component[2] .

The influence of said optical or opto-electrical component is represented by using a 4 by 4 matrix known as a Mueller matrix. The transmission of light through an arbitrary device can be expressed as the product of the Mueller matrix and input Stokes vector which represents the

[2] Optical reflections and other transmission related parameters, such as responsivity can also be determined using Mueller matrix terms, to simplify the text only optical insertion losses and optical components are discussed throughout this section.

SoP of the lightwave incident upon the component. Equation 3.4 shows the output transmission Stokes vector, using T_i terms, and the incident Stokes vector, using S_i terms:

$$\begin{bmatrix} T_0 \\ T_1 \\ T_2 \\ T_3 \end{bmatrix} = \begin{bmatrix} m_{00} & m_{01} & m_{02} & m_{03} \\ m_{10} & m_{11} & m_{12} & m_{13} \\ m_{20} & m_{21} & m_{22} & m_{23} \\ m_{30} & m_{31} & m_{32} & m_{33} \end{bmatrix} \begin{bmatrix} S_0 \\ S_1 \\ S_2 \\ S_3 \end{bmatrix} \tag{3.4}$$

Stokes vectors are defined by using the following normalized Stokes parameters:

▷ S_0 represents the total intensity of the input power

⇒ if kept constant to 1, only insertion losses from to the DUT are included in the computation

▷ S_1 represents the ratio of Linear Horizontal (**LHP**) to Linear Vertical Polarization (**LVP**)

⇒ the corresponding Stokes vectors being $\begin{bmatrix} 1 & 1 & 0 & 0 \end{bmatrix}^T$ and $\begin{bmatrix} 1 & -1 & 0 & 0 \end{bmatrix}^T$ respectively

▷ S_2 represents the ratio of Linear +45 degrees (**L+45**) to Linear -45 degrees (**L-45**) Polarization

⇒ the corresponding Stokes vectors being $\begin{bmatrix} 1 & 0 & 1 & 0 \end{bmatrix}^T$ and $\begin{bmatrix} 1 & 0 & -1 & 0 \end{bmatrix}^T$ respectively

▷ S_3 represents the ratio of Right-hand Circular (**RCP**) to Left-hand Circular (**LCP**) Polarization

⇒ the corresponding Stokes vectors being $\begin{bmatrix} 1 & 0 & 0 & 1 \end{bmatrix}^T$ and $\begin{bmatrix} 1 & 0 & 0 & -1 \end{bmatrix}^T$ respectively

Figure 2.7 shows how these different Stokes vectors are mapped onto the surface of a Poincaré sphere.

In Equation 3.4, T_0 is the intensity of the transmitted or output power. This is the only value a normal optical power meter can detect. T_1 to T_3 can only be measured with special instruments, such as a Polarimeter, as they relate to the polarization state of the output power. To only take into account the T_0 term, Equation 3.4 can be simplified as follows:

$$\begin{bmatrix} T_0 \end{bmatrix} = \begin{bmatrix} m_{00} & m_{01} & m_{02} & m_{03} \end{bmatrix} \begin{bmatrix} S_0 & S_1 & S_2 & S_3 \end{bmatrix}^T \tag{3.5}$$

Standard rules of matrix multiplication do apply, hence Equation 3.5 can be rewritten as follows:

$$T_0 = m_{00}S_0 + m_{01}S_1 + m_{02}S_2 + m_{03}S_3 \tag{3.6}$$

Using the DUT's Mueller matrix terms and modifying the incident Stokes vector allows the influence of incident SoP on the detected output power, T_0, to be simulated. Extracting the Mueller matrix terms for each desired wavelength further allows the T_0 term to be evaluated for each wavelength step. Equation 3.6's notation may be changed to reflect this, as stated in

Equation 3.7 which is the corner-stone of the SoP simulation described throughout the following Chapter.

$$T_0(\lambda) = m_{00}(\lambda) S_0 + m_{01}(\lambda) S_1 + m_{02}(\lambda) S_2 + m_{03}(\lambda) S_3 \tag{3.7}$$

3.2.2 Mueller matrix terms extraction

The technique described in the patent, (17), and since standardized in (46), allows efficient and repeatable measurements of PDL across large wavelength spans by computing the extremes of insertion loss at each wavelength step. This technique extracts the PDL spectrum by using the Mueller matrix terms seen in Equation 3.5.

These terms are extracted by applying four different linearly independent incident SoPs to the DUT. A single alignment step with no associated fiber rotation is required and apart from an initial station calibration no other operator intervention is required.

In MetroPhotonics Inc.'s initial hardware implementation of this measurement approach, the JDS Uniphase Swept Wavelength System (**SWS**) was used to perform optical device insertion loss characterizations. The SWS' unique system architecture allows the use of multiple testing receiver chassis with a single optical source. The optical signal sent contains a signal which indicates to the chassis which of the four incident SoPs is currently being sent. As recommended in (46), this system also uses optical splitters to monitor the input power to the receiver chassis. This allows further corrections for any TLS output power fluctuations since the last calibration was done and helps counteract any PDR of the photodetectors used. More details on the operation and measurement steps required to obtain accurate results when using the SWS can be reviewed in (27; 28).

Figure 3.8 shows a typical SWS hardware configuration with the Source Optics Module (**SOM**) which controls the TLS and the four-state polarization controller. The required fiber types, normal Single-Mode Fiber (**SMF**) or PM, are also presented in this figure. It should be pointed out that non-PM fiber is used to reach the different receiver chassis and to excite the DUT ensuring transmission of the circular polarization states required. While only a single receiver chassis is shown, multiple testing stations can be operated from a single SOM+TLS+polarization controller setup. A Personal Computer (**PC**) is required at each test stations to initiate the different measurements, as well as download the data from the receiver chassis' built-in memory. Different types of product configuration are shown alongside different calibration steps required.

The SWS was originally meant to perform only optical insertion loss measurements, but some SWS receiver modules were customized to attempt to measure direct photocurrents. The normally built-in photodetectors were bypassed to reach the current sampling electronics. More details can be found in Section 3.3.

The four incident SoP typically used are listed here alongside their corresponding Stokes vectors:

- ▷ LHP $\Rightarrow \begin{bmatrix} 1 & 1 & 0 & 0 \end{bmatrix}$
- ▷ LVP $\Rightarrow \begin{bmatrix} 1 & -1 & 0 & 0 \end{bmatrix}$
- ▷ L+45 $\Rightarrow \begin{bmatrix} 1 & 0 & 1 & 0 \end{bmatrix}$

Figure 3.8: SWS hardware configuration

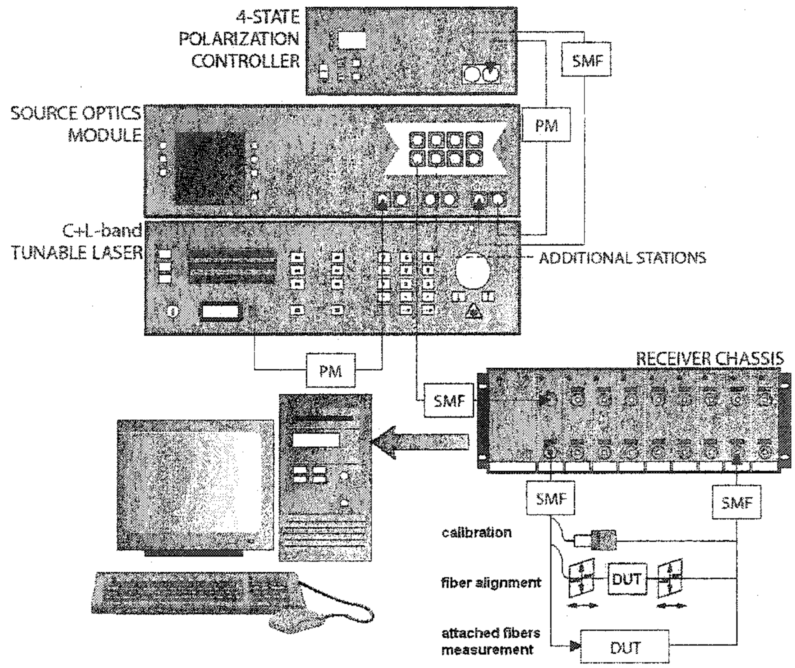

▷ LCP $\Rightarrow \begin{bmatrix} 1 & 0 & 0 & -1 \end{bmatrix}$

While these four states are carefully controlled at the output of the polarization controller the inherent retardance of the fiber patchcords used rotates them upon the Poincaré sphere. The SoP of a lightwave propagating along a normal SMF fiber does vary slightly. While it would be ideal to maintain the same SoP from the generation to the excitation point of the DUT if the same retardance effect is applied to each of the four SoP then the Mueller calculus described herein can still be applied.

Henceforth the only requirement for this technique to provide valid PDL results is that these four SoPs remain orthogonal to each other. The measurement validity depends only on the relative coordinates of the four incident SoPs not their absolute coordinates. Results are valid as long as the set of SoPs maintain relative angular separations of 90 degrees about the origin of the Poincaré sphere for each wavelength. Special care is required to ensure no polarization-dependent retardance is present in the optical path such as PM-fiber which cannot transmit circular-polarized light and would severely affect the measurement. Figure 3.9 shows the impact of a small retardance on the Poincaré sphere; point a moves to point 1, b to 2, and so on. Mueller matrix terms obtained in both cases would be equivalent. The fibers used between the SOM, TLS and polarization controller setup and the receiver chassis must be kept as immobile as possible after taking reference measurements and during measurements.

Another requirement for the extracted Mueller matrix terms to be valid is to reduce any artificial source of PDL throughout the measurement setup. A typical example of an artificial source of PDL is dirty fiber connectors. Evidence of the impact of such artifacts can be deduced

Figure 3.9: Retardance impact on initially generated SoPs

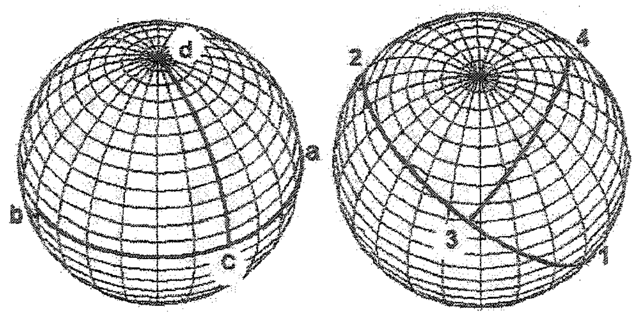

from the analysis of results obtained for damaged input waveguide facets or misaligned fibers. These result in scattered light and unresolvable Mueller matrix terms. The scattered light acting as a source of unpolarized noise which does not correlate to the corresponding individual states of polarization sent towards the DUT. The system used to guide the light towards the DUT must be kept as stable as possible to reduce its influence and avoid errors in the measurements.

The same impact can be noticed for electrical noise sources present in the measured signal. Any 60Hz electrical signal generated from wiring ground loops originally found in our SWS photocurrent measurement test station would create unresolved Mueller matrix terms. These random noise sources are uncorrelated to the incident SoP and impact the computation of the Mueller matrix terms.

Pure retardance does not impact the accuracy of the extracted Mueller matrix term. But retardance coupled with measurement system PDL-artifacts and noise sources may. Ongoing efforts to compensate for PDL artifacts by performing the measurement of a total of six incident SoPs are detailed in (7). MetroPhotonics Inc.'s PDL accuracy requirements fall well within the accuracy of a normal four incident SoPs approach. The increase in PDL accuracy when using the six-state approach does not yet provide enough incentive to suffer from a 50% increase in testing time. Careful engineering design, monitoring and maintenance of test stations help ensure repeatable and accurate measurements of PDL and early detection of artifact PDL sources.

From the four measurements obtained for each of the four incident SoPs, the Mueller matrix terms can be extracted for each wavelength step by using the following equations, where $T_{0_{(X)}}$ corresponds to the X incident SoP measured transmission:

$$m_{00}(\lambda) = \frac{T_{0_{(LHP)}}(\lambda) + T_{0_{(LVP)}}(\lambda)}{2} \tag{3.8}$$

$$m_{01}(\lambda) = \frac{T_{0_{(LHP)}}(\lambda) - T_{0_{(LVP)}}(\lambda)}{2} \tag{3.9}$$

$$m_{02}(\lambda) = T_{0_{(L+45)}}(\lambda) - \left(\frac{T_{0_{(LHP)}}(\lambda) + T_{0_{(LVP)}}(\lambda)}{2}\right) \tag{3.10}$$

$$m_{03}(\lambda) = \left(\frac{T_{0_{(LHP)}}(\lambda) + T_{0_{(LVP)}}(\lambda)}{2}\right) - T_{0_{(LCP)}}(\lambda) \qquad (3.11)$$

Figure 3.10 shows typical Mueller matrix results for a polarization-compensated and polarization-uncompensated main filter lobe as a function of wavelength. The $m_{01}(\lambda)$, $m_{02}(\lambda)$ and $m_{03}(\lambda)$ terms show much larger values for the uncompensated DUT, which entail larger spectrum fluctuations of the resulting $T_0(\lambda)$ as the incident Stokes vector varies.

Figure 3.10: Mueller matrix terms of polarization-compensated and -uncompensated DUTs

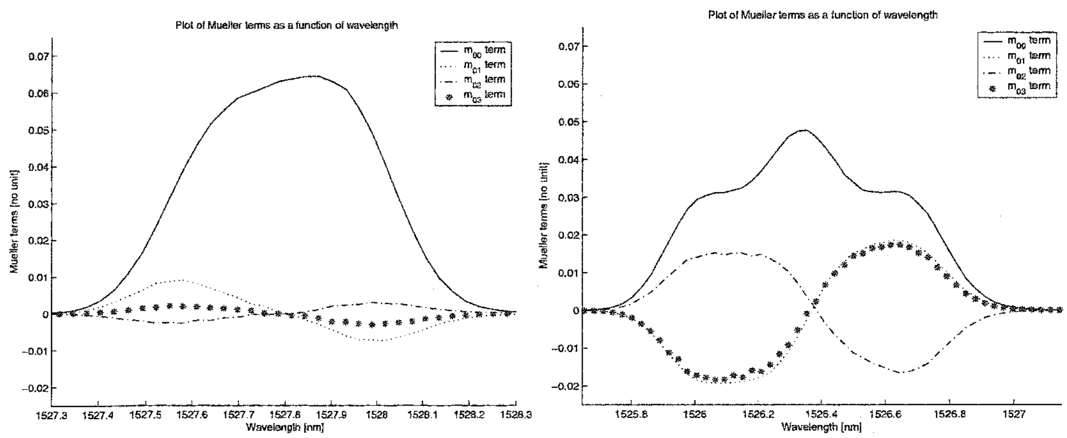

(a) Polarization-compensated DUT

(b) Polarization-uncompensated DUT

3.2.3 Polarization dependent loss measurement results

The analysis technique described in (17) aims to provide PDL results across large wavelength spans by computing the extreme values of insertion loss at each wavelength step from extracted Mueller matrix terms.

The difference between the maximum and minimum insertion loss corresponds to the PDL for each wavelength step. The resulting spectrum created from the individual maximum and minimum insertion losses at each wavelength are called the **MAX** and **MIN** spectrum respectively. At each individual wavelength step, the maximum and minimum values are termed the $T_{0_{MAX}}(\lambda)$ and $T_{0_{MIN}}(\lambda)$.

The following equations are used to extract these terms, in linear scale.

$$T_{0_{MAX}}(\lambda) = m_{00}(\lambda) + \sqrt{m_{01}^2(\lambda) + m_{02}^2(\lambda) + m_{03}^2(\lambda)} \qquad (3.12)$$

$$T_{0_{MIN}}(\lambda) = m_{00}(\lambda) - \sqrt{m_{01}^2(\lambda) + m_{02}^2(\lambda) + m_{03}^2(\lambda)} \qquad (3.13)$$

The resulting PDL can be computed for each wavelength, by using the following equation:

$$PDL(\lambda) = 10\log\left[\frac{T_{0_{MAX}}(\lambda)}{T_{0_{MIN}}(\lambda)}\right]\ [dB] \qquad (3.14)$$

PDL meters have also been built around polarization controllers and the above mentioned 4-states measurement approach, yielding PDL measurements more rapidly than the common 10 seconds measurement time per wavelength. The real testing capacity benefits of this approach come when used in conjunction with a sweeping TLS, instead of using individual steps as described in Section 3.1.2.

Figure 3.11 shows the $T_{0_{MAX}}$ and $T_{0_{MIN}}$ spectra, as well as the PDL spectrum for a polarization compensated DUT. As desired, the PDL results are minimized in the main filter lobe, which is desirable to minimize the impact on the demultiplexed channel, as a function of incident SoP. The PDL curve never reaches the 0dB point, but reaches less than 0.5dB as required by the desired ±0.5dB reported power accuracy specification of the SurePath Monitor^{TM}.

Figure 3.11: Extreme spectra and PDL spectrum of polarization-compensated DUT

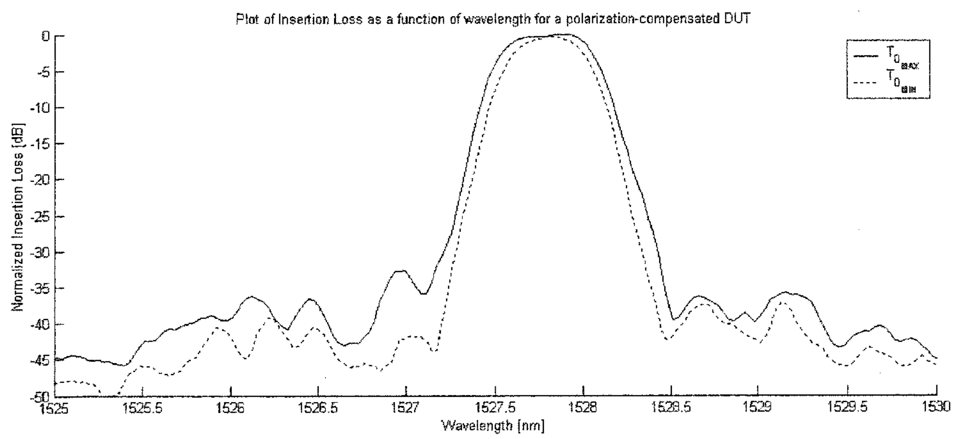

(a) Extreme spectra

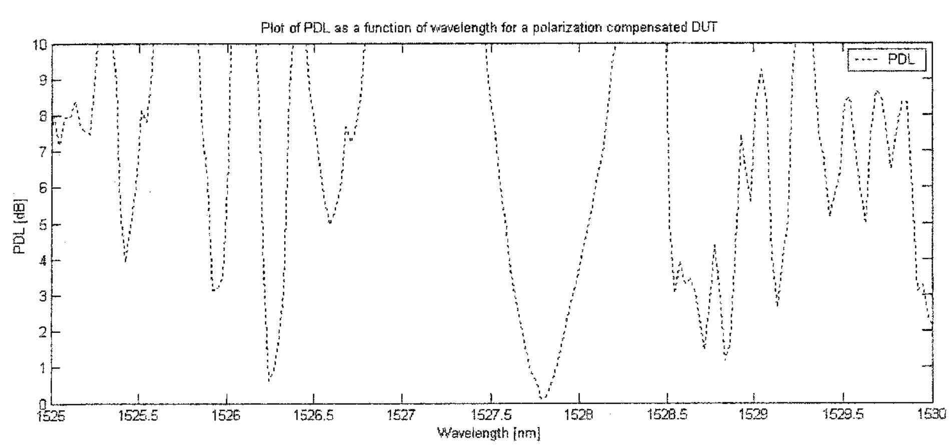

(b) PDL Spectrum

The PDL spectrum is used to ensure that the performance of the DUT can be guaranteed for any incident SoP. These same equations can be applied to both insertion loss and responsivity measurements where the PDR, as a function of wavelength, can be extracted. Figure 3.12 shows a typical single channel normalized responsivity spectrum, with the maximum and minimum responsivity at each wavelength. The two smaller peaks seen on both sides of the main peak are caused by a reticles stitching error. These could only be accurately measured after all the required enhancements to the tests stations were implemented as they represent signals intensities of a several picoamperes (**pA**), as discussed in Section 3.3.

The PDR spectrum can be used to evaluate the error in reported input power for any incident SoP as a function of the measured photocurrent, in the SurePath Monitor™ product.

Figure 3.12: Normalized single channel extreme responsivity spectrum

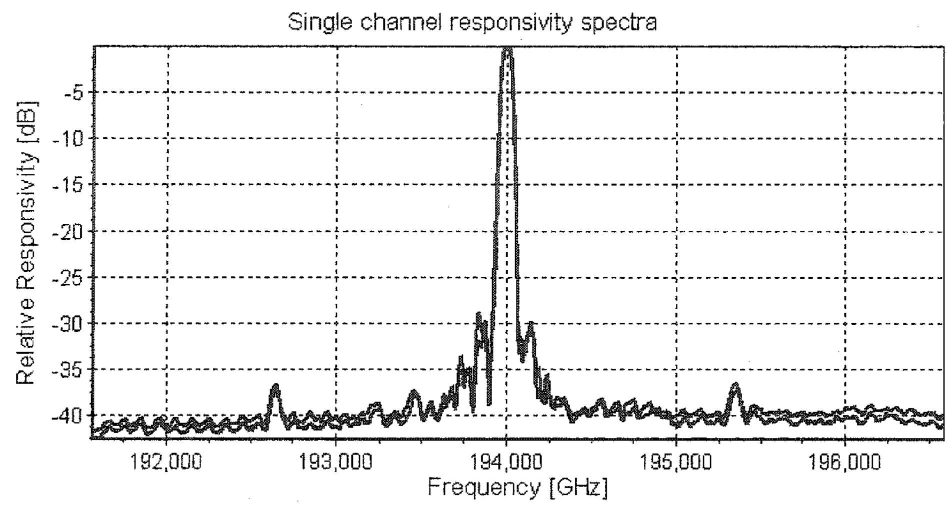

The average value of the maximum and minimum responsivity for each wavelength or frequency, $\frac{R_{0_{MAX}}(\lambda)+R_{0_{MIN}}(\lambda)}{2}$, is used to convert the photocurrent into measured power. It follows that the worst-case polarization dependent error would be half of the PDR at the wavelength of interest. The same concepts can be applied to the expected insertion loss; *i.e* the insertion loss can be expected to vary between $IL_{0_{MAX}}(\lambda)$ to $IL_{0_{MIN}}(\lambda)$ as the incident polarization is changed.

Figure 3.13 shows the superimposed extreme responsivity spectra of all 43 channels of a SurePath Monitor™ device. The worst-case crosstalk leaking into adjacent and non-adjacent channels can be evaluated and taken into account when executing input power correction algorithms. This level of accuracy in the complete C-band extreme responsivity spectrum allows unsurpassed performance when compared to other optical power monitor products. For more details on the specifications of the SurePath Monitor™, consult Appendix E.

The SWS test station, using a sweep rate of 20nm/s and fully automated through LabVIEW programming, averages about two full C-band measurements and data download per minute. The wavelength step is set to 3pm which is a giant leap in capacity when compared to PM-fiber measurement techniques. Furthermore, fully automating the sampling of the electrical building blocks by using an external switching architecture, offers even more throughput. Table 3.4 shows the approximate time needed for the three main measurement techniques that

Figure 3.13: Full normalized extreme responsivity spectrum

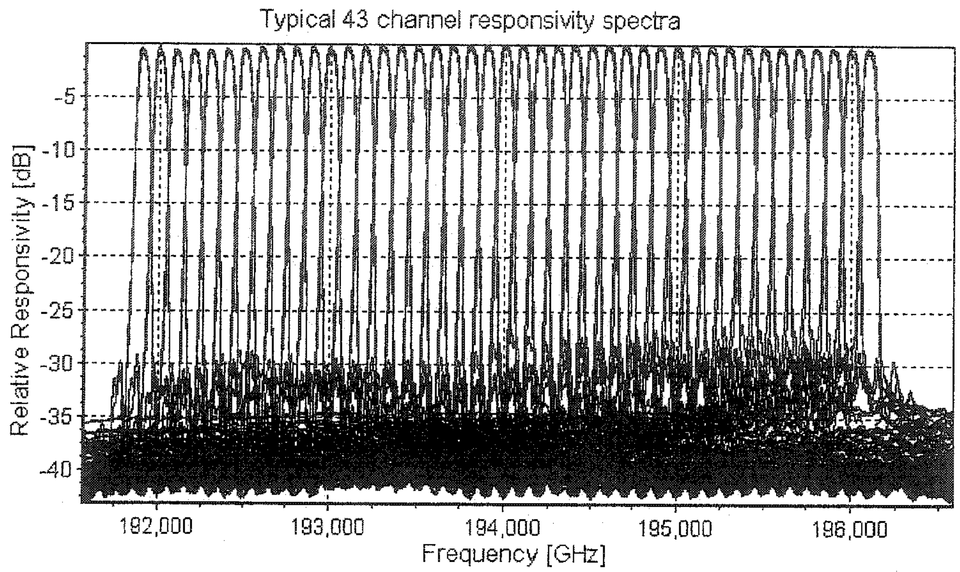

have been considered for measurement of the SurePath Monitor™ product.

Table 3.4: Time required for different measurement techniques

Measurement technique	λ step	averaging time per λ	time per channel	Equivalent time per channel
Polarization sampling	variable	≈10 seconds	variable	≈42 hours
PM-fiber technique	5 pm	N/A	≈10 minutes	≈38 minutes
Mueller matrix-based technique	3 pm	N/A	≈30 seconds	≈30 seconds

The time required for each technique was scaled linearly to allow direct comparison techniques if equivalent test requirements were to be used. Being the most stringent, the default Mueller matrix-based technique measurement settings were used. The measurement from 1525 to 1570nm with 3pm steps, which yields 15,000 data points. The testing capacity impact to obtain equivalent results using the polarization sampling or PM-fiber techniques is obvious and further shows why matrix-based measurement techniques greatly increase the ratio of data acquired for a reference period of testing time.

Clearly, techniques used early on with MetroPhotonics Inc. to determine the polarization dependent of performance different devices became too tedious as production volumes increased. Some of these techniques are simply not suited for devices which operate over a large range of wavelengths with high channel counts. Too many trade-offs in wavelength range and accuracy have to be taken into account. Only matrix-based techniques have proven to be economically sound solutions to manage large-volume production testing of PIC devices.

Table 3.5 summarizes the advantages and disadvantages of the Mueller matrix-based measurement techniques.

Table 3.5: Summary of Mueller matrix-based measurement technique

Advantages
Wavelength sweeping enables faster data acquisition
Single fiber alignment required, reduced potential of fiber handling and damage
PDL/PDR results obtained for full operating wavelength range, no compromise of wavelength step, or risk of undersampling, alongside $T_{0_{MAX}}(\lambda)$ and $T_{0_{MIN}}(\lambda)$ spectra
Technique can be used from die screening to final package assembly, since no fiber rotation requirement, ensuring more traceable results throughout the production cycle
No risk of operator fatigue as polarization variation is automated, and not dependent on operator skills, nor patience during calibration steps
Mueller matrix terms can be extracted for future analysis, as discussed in Chapter 4
Disadvantages
More complex calibration technique and hardware requirements, yet fully automated
Four-SoP approach has risk of increased artifact PDL error, while alternative six-SoP approach increases test time by 50% but compensated for such artifacts
TE and TM spectrum not measured directly, but, as seen in Chapter 4, Mueller matrix terms can be used to simulate them

3.3 Photocurrent and responsivity measurements

The SWS system was originally designed to perform optical insertion loss measurements. The T&M group attempted to convert this station to perform photocurrent and absolute responsivity measurements. Instead of using the typical optical detector module heads, direct access to the positive and negative inputs of the built-in logarithmic TransImpedance Amplifiers (**TIA**) used to convert the photocurrent to a voltage, was made possible through custom-made modules.

Some fundamentals issues were uncovered late into this project. These issues explain why the overall accuracy of the SWS absolute responsivity measurements was not satisfactory, although its precision is as specified for the normal passive optical insertion loss measurements.

Special measurements were used to extract an approximate set of Mueller matrix terms representing the input power to the DUT for all four orthogonal states. This was performed by measuring the spectra in the absence of any excitation towards the reference detector, by basically placing the dust cap back onto the reference detector to block all incoming light. Since the SWS firmware would limit small signals to -120dB, the signal seen at these low signal levels were related to the measured input power references saved to text files on the control PC.

Unfortunately an external cavity, or optical etalon, is present when the reference detector is being used. The cavity is removed when the actual DUT measurements are performed but the reference files stored on the control PC reintroduce a mirror image of the cavity effect into the measurement result. Additional coupling loss is also added. This affected the accuracy of the absolute responsivity calibration of the DUT. An optical etalon being present during a passive optical was acceptable as these measurement were still relative measurements. Any repeatable variation in insertion loss, which remains the same for references and measurements, would be taken into account and removed from the final insertion loss spectrum.

This special analysis was also based upon the assumption that the precise calibration of the responsivity of the reference detector would not fluctuate over time. Unfortunately, due to a high level of handling and use of different fiber connectors, a variation in coupling loss was noticed which reduces the precision of the reported absolute responsivity measurements.

As shown in Figure 2.8 on page 14, the SurePath Monitor™ p-i-n photodetectors must be reversed-biased, using V volts, so that the appropriate generated photocurrent, I_p, can be measured. The inclusion of a power supply and current measurement system may render the measurement system susceptible to issues with electromagnetic noise pickup due to inappropriate shielding. After many hardware revisions special low-capacitance triax wiring was found to be essential to avoid any impact on the bandwidth of the logarithmic TIAs. As well, high isolation solid-state switching cards were used to select the appropriate channel's p-contact and triax cabling to help reduce and maintain the noise floor down to nanoamperes (**nA**) levels and ensure the isolation between adjacent photodiodes was still within the range of gigaohms (GΩ).

Due to the fact the input power to the DUT on the SWS station could not be increased without upgrading the whole system to a new generation of the SWS, the average input power to the DUT was only around -18 to -15dBm. Considering these levels of input power combined with crosstalk performance levels of up to 40dB from the DUT, sub-nA measurement capabilities were required. Logarithmic TIAs, like the ones built-in the SWS modules, or multiple linear amplifiers in parallel were necessary to match the large dynamic range measurements required to match the crosstalk performance of the DUT.

The floating analog ground used within the SWS measurement modules, while sufficient for shielding the short connections within the normal module, was found to be insufficient to shield the required wiring necessary to connect all of the DUT's photodiodes to a switch system. This made the overall system highly sensitive to 60Hz signals due to wiring ground loops. Noise signals would show up in sweeping measurements as etalon-like fringes due to the constant sweeping rate and their sinusoidal nature. Such severe distortions affected the accuracy of extreme centre frequency and peak responsivity results, forcing a change to 10dB-levels to extract required parameters. The low input power range reduced the range of measurement between the peak of the filter response and its noise floor, as the echelle grating's own demultiplexing noise floor was dwarfed by other noise sources.

A custom-built probing station was designed to align probes to the pads on the wire-bonded ceramic carrier, enabling the selection of the desired individual channels to be characterized. Figure 3.14 shows the setup used, with the fiber being aligned and two sets of probes on each side of the DUT.

A precise but inaccurate responsivity spectrum could be extracted from the SWS generated absolute responsivity Mueller matrix terms. Additional equipment were required to measure the leakage current of the diode under no light excitation for calibration. All these issues alongside the complex analysis required to convert the relative measurements to absolute responsivity measurements forced the T&M group to explore alternative measurement equipment.

Figure 3.14: Wirebond test station setup

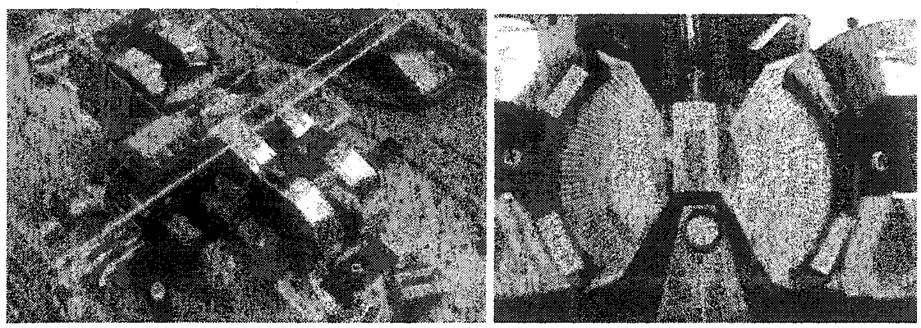

(a) Fiber alignment and probes holder stages (b) DUT on carrier with align input fiber

The dBm Optics Inc. Component Spectrum Analyzer™ (**CSA**) was chosen[3] to answers the T&M group's needs. Its approach to calibration resolved many of the issues discussed above. Based on the same Mueller matrix measurement approach, it also relied on *in situ* monitoring of the input power and wavelength of the signals reaching the DUT. This allows direct computation of responsivity Mueller matrix terms with highly increased accuracy. Built-in splitters, with very low polarization-dependent splitting ratios, are used to compute the input power to the DUT after calibration of the different patchcords found in the measurement system. This is made possible as all measurements results are available rather than only the computed relative results as for the SWS. In this fashion the CSA is comparable to an OSA measurement system as it allows complex measurements by allowing modifications of all desired settings, instead of only providing the final results of a single measurement approach.

A unique TLS is used for each individual CSA station hence the input power to the device can be largely increased to about −5dBm. Higher input power reduces the wiring shielding burden as any residual noise source, such as 60Hz noise due to wiring ground loops or other sources were now dwarfed by the optical demultiplexer's own noise floor. Subtle echelle-grating induced spectral structures, which could not be measured when using the SWS, could now be measured and analyzed with the CSA measurement results.

Furthermore, while the SWS was meant to be a multi-channel system, as seen in Figure 3.8 on page 35, the measurement of multiple active spectrum involved duplicating all the hardware required to bias the photodiodes. The CSA has its own built-in biasing sources which allows greater flexibility and facilitates multi-channel absolute responsivity measurements for the same DUT. This further increasing the testing capacity. Current benchmark testing time averages about 45 minutes for a complete 43-channel SWS measurement. This includes the measurement of the individual waveguide photodetector leakage currents using another piece of equipment. Using the CSA, the same measurement have been reduced to only 25 minutes with no intermediate step as no other piece of equipment is required. Initial results of moving to three simultaneous measurements have reduced the measurement time to around eight to ten minutes per DUT.

[3] More details on the CSA can be found in (10; 11).

The CSA also allows measurements using six incident SoPs, which has been shown (7) to increase PDL accuracy by reducing the influence of external PDL artifacts found in the optical path between the polarization controller, CSA and DUT.

Figure 3.15 shows the CSA system complete with a TLS, a polarization controller and the CSA mainframe. Also shown are the switch mainframe, triax wiring and a SurePath Monitor™ device mounted on a testing Printed Circuit Board (**PCB**). This PCB is used to ease the connection of the multi-pin butterfly package to the switch mainframe and related wiring, temperature controller and alarm temperature sensor measurement equipment.

Figure 3.15: CSA SurePath Monitor™ package test station

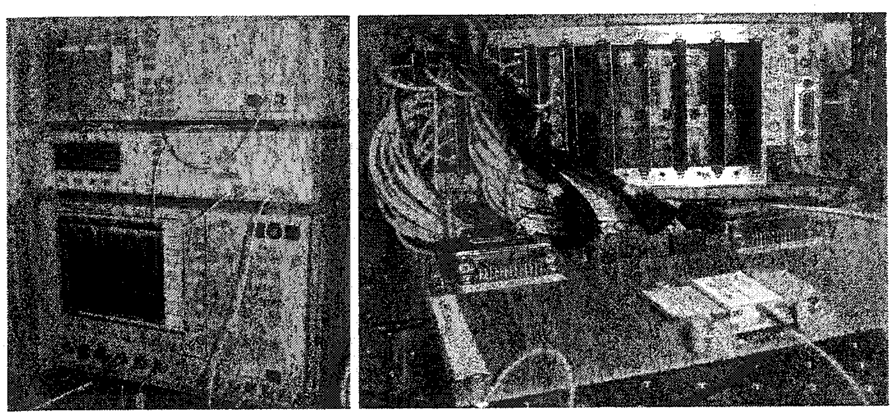

(a) TLS, SoP controller and CSA (b) Switch mainframe, wiring and DUT on PCB

In summary, the basic Mueller matrix approach can be used with many different types of polarization sensitive signals, be it optical insertion loss or opto-electrical absolute responsivity spectra. Different incarnations of the preferred embodiment, described in (17), helped considerably increase the production testing capacity of the T&M group. The CSA system enabled the T&M group to reach new levels of accuracy for responsivity results of the SurePath Monitor™ product. It was designed from the ground-up to ease the characterization of biased photodiodes over large wavelength spans in a very efficient manner. It also allows Mueller matrix terms to be extracted to allow further in depth analysis as described in Chapter 4.

Chapter 4

State of polarization simulation and TE/TM spectrum

While (17) provides an elegant and efficient technique to extract PDL information over large wavelength range by using DUT Mueller matrix terms, Mueller calculus can be applied to further explore the DUT's performance.

As described in Section 3.2.1 the variation in detected output power intensity at each wavelength, $T_0(\lambda)$, can be related to the incident SoP. This chapter focuses on the simulation engine created to obtain the resulting spectrum corresponding to any desired fully-polarized incident SoP. Details on the preferred technique used to extract the DUT's Mueller matrix terms, for all wavelength of interest, are laid out in Section 3.2.2.

One of the main goal of this project was to provide more insight into the performance of MetroPhotonics Inc. products by extracting the extreme orthogonal SoPs, namely the TE and TM spectrum.

The insertion loss extremes, computed using the Mueller matrix terms as described in Section 3.2.3, are well suited to verify that the DUT performance is within specifications for all possible incident SoPs. Yet, these extreme insertion loss spectra, $IL_{MAX}(\lambda)$ and $IL_{MIN}(\lambda)$, and the corresponding PDL spectrum are often insufficient to help optimize polarization-dependent PIC building blocks. This is also true for the optimization process of the overall performance of integrated PIC devices. For the final calibration factors for the SurePath Monitor™ product this information can be extracted from the extreme responsivity spectra.

For each step of the fabrication process flow the orthogonal TE and TM spectrum are often preferred. These allow further exploration of issues related to different assembly steps such as die-attachment, fiber alignment and packaging by investigating shape factor or PDf variations.

The TE and TM spectrum are most useful for internal design- and fabrication-oriented customers, while the extreme spectra are meant to provide accurate calibration results for external customers who are most interested in specifications across all possible incident SoPs.

4.1 Integration testing strategies and trade-offs

While optical integration enables designers to condense more functionality into smaller components, it makes the task of evaluating the individual building blocks more difficult. Only the sum of all the different parts can be evaluated efficiently. Careful design and evaluation of test structures is essential to confirm design models and improve future iterations of product designs.

This project aimed to isolate the TE and TM spectrum by following two analysis philosophies. The first is the most computationally intensive and is based on the sampling of different incident SoPs, and the generation of each corresponding spectrum using the known DUT Mueller matrix terms. From these simulated spectrum, manifestations of the TE and TM modes propagating through the device are investigated by evaluating the impact of varying the incident SoP on different performance parameters. This approach is focused on parametric analysis of spectra resulting from the Poincaré sphere sampling.

The second approach exploits the orthogonal nature of the TE and TM modes, Mueller matrix terms are analyzed to find the most orthogonal pair of incident Stokes vectors. Instead of randomly sampling the surface of the Poincaré sphere while looking for two independent points, with no guarantee that the resulting TE and TM solutions being orthogonal. This new approach only samples orthogonal pairs of incident SoPs. Based on numerical analysis of Mueller matrix terms, this technique aims to find the base set of Stokes vector, from which the spectral response of different incident SoPs can be expressed as linear combinations.

Two of these numerical approaches were evaluated. The first approach samples only half of the Poincaré sphere enforcing the orthogonality of the two SoPs by looking at the opposite point on the other half of the sphere. The pair of orthogonal incident Stokes vectors yielding a maximum normalized difference in spectra is chosen to represent the TE and TM spectrum.

The second numerical approach examined the whole surface of the Poincaré sphere taking into account all possible incident Stokes vectors. By evaluating the whole surface of the Poincaré sphere as a single system of equations, it can be shown that the solution to the maximum difference in spectra for orthogonal states is obtainable by using simple eigenvectors and eigenvalues numerical solving techniques.

Figures 4.1 and 4.2 show typical end results of these different criteria and analysis algorithms for polarization-compensated and polarization-uncompensated DUT. The TE and TM spectra of these DUTs are then extracted from the DUT Mueller matrix terms once the appropriate pair of orthogonal incident SoPs is determined. An equal mix of both of them is also shown, as a visual cue of the impact of traveling upon the Poincaré sphere.

These figures show the results of two different devices, with and without a polarization compensator, for the same channel. The presence of the polarization compensator create a centre frequency variation of around 200GHz, which explains the offset in centre frequencies of these devices.

4.2 Simulation using incident Stokes vectors

Sampling the Poincaré sphere corresponds to changing the incident Stokes vector or incident SoP, as seen in Equation 3.7 and transcribed here as Equation 4.1:

$$T_0(\lambda) = m_{00}(\lambda) S_0 + m_{01}(\lambda) S_1 + m_{02}(\lambda) S_2 + m_{03}(\lambda) S_3 \tag{4.1}$$

Keeping $S_0 = 1$, ensures only the DUT insertion loss is evaluated. The norm of the

Figure 4.1: Extreme orthogonal SoPs for a polarization-compensated DUT

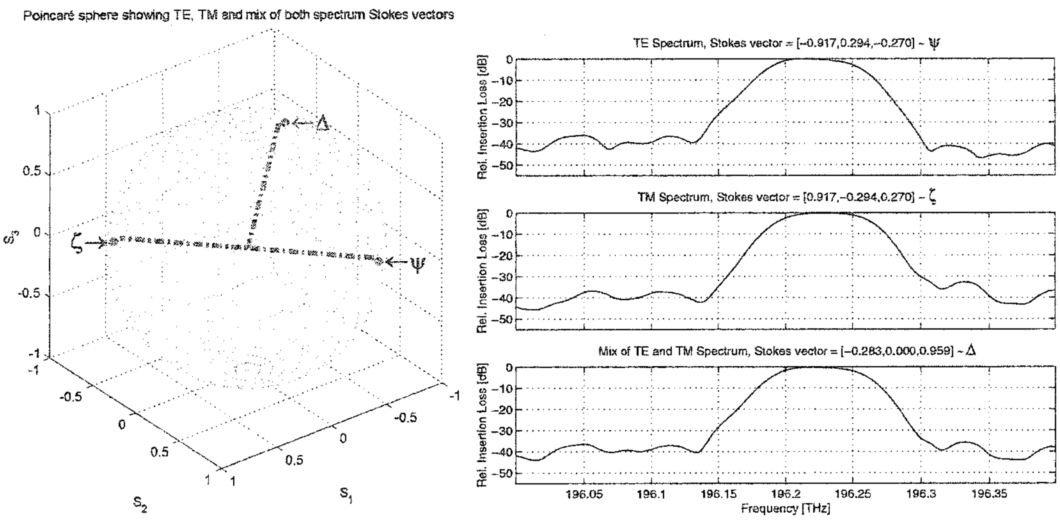

(a) Corresponding Poincaré sphere (b) Spectrum of TE, TM and mix of both

Figure 4.2: Extreme orthogonal SoPs for a polarization-uncompensated DUT

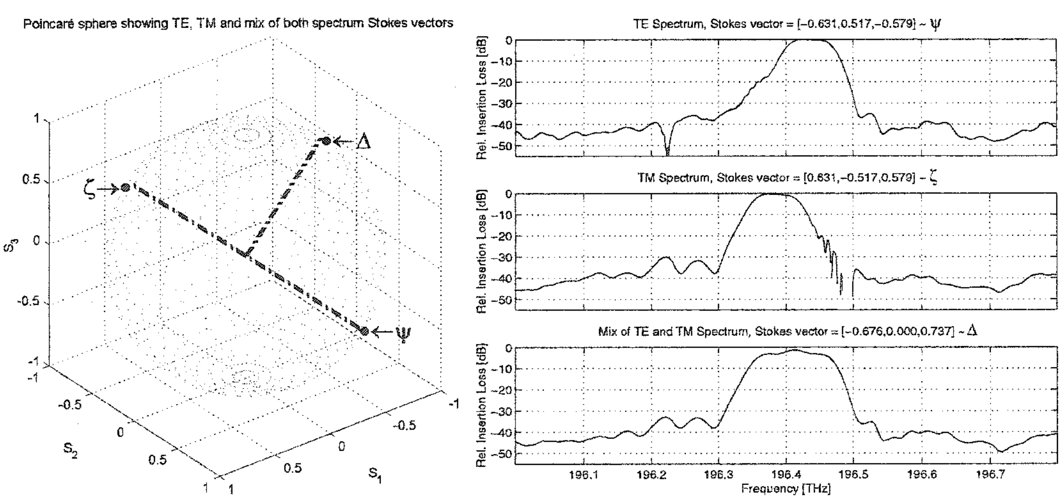

(a) Corresponding Poincaré sphere (b) Spectrum of TE, TM and mix of both

remaining Stokes vector terms, $\begin{bmatrix} S_1 & S_2 & S_3 \end{bmatrix}$, is kept equal to 1, so that all sampling occurs upon the surface of the Poincaré sphere where fully polarized SoPs are found.

A polarization modification technique used in many polarization controllers to change the SoP of an incoming beam of light is the combined rotation of two waveplates, a quarter-waveplate, $\frac{\lambda_0}{4}$, and a half-waveplate, $\frac{\lambda_0}{2}$. As shown in the notation used, these waveplates are designed for a nominal wavelength of λ_0. Satisfactory results can be obtained across a large span around this nominal wavelength with the only consequence of slightly increasing the PDL of the controller.

This approach is analogous to the influence of matching stubs towards impedances and reduction of reflections within a microwave circuit at specific design frequencies. An additional linear polarizer is often added to optimize the output power by lining it up with the nominally linear polarization of the incident laser light, as shown in Figure 4.3.

Figure 4.3: Typical schematic of waveplate-based polarization controller

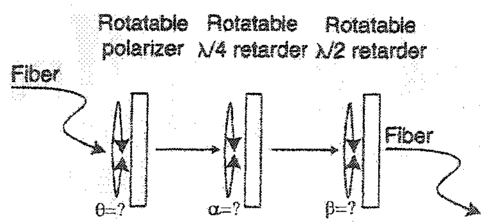

The SoP-simulation engine mimics this approach by simulating the combined influence of a quarter- and half-waveplate on linearly polarized incident light. The fast axis of the quarter-waveplate and half-waveplate are set to angles of α (varied from 0 to 180 degrees) and β (varied from 0 to 90 degrees), respectively.

This technique offers the advantage of being intuitive as it is based on a real-world architecture. Other Poincaré sphere sampling algorithms that could provide more uniform sampling were considered but abandoned as this technique was found to provide sufficient coverage of the sphere, given the fact that enough computational power was available for analysis.

As detailed in Section 3.2.1, Mueller calculus allows us to find the intensity of an emerging lightwave when the polarization state of the incoming beam and the Mueller matrix terms of the device through which it passes are known. Any fully-polarized incident SoP can be obtained by using the combined action of the incident linearly polarized light, the Mueller matrix of a quarter-waveplate, $M_{\frac{\lambda_0}{4}}(\alpha)$, and a half-waveplate, $M_{\frac{\lambda_0}{2}}(\beta)$ as shown in Equation 4.2.

$$\begin{bmatrix} S_0 \\ S_1 \\ S_2 \\ S_3 \end{bmatrix} = M_{\frac{\lambda_0}{2}}(\beta)\, M_{\frac{\lambda_0}{4}}(\alpha) \begin{bmatrix} 1 \\ 1 \\ 0 \\ 0 \end{bmatrix} \tag{4.2}$$

Expansion of the $M_{\frac{\lambda_0}{4}}(\alpha)$ and $M_{\frac{\lambda_0}{2}}(\beta)$ terms is detailed in Appendix C.1. The resulting equation is shown in Equation 4.3.

$$\begin{bmatrix} S_0 \\ S_1 \\ S_2 \\ S_3 \end{bmatrix} = \begin{bmatrix} 1 \\ \cos^2(2\alpha)\cos(4\beta) + \cos(2\alpha)\sin(2\alpha)\sin(4\beta) \\ \cos^2(2\alpha)\sin(4\beta) - \cos(2\alpha)\sin(2\alpha)\cos(4\beta) \\ -\sin(2\alpha) \end{bmatrix} \tag{4.3}$$

By using the above expansion, the $T_0(\lambda)$ term found in Equation 4.1 can be expressed as a function of the newly defined α and β angles, as follows:

$$T_0(\lambda) = m_{00}(\lambda) + m_{01}(\lambda)\, S_1(\alpha,\beta) + m_{02}(\lambda)\, S_2(\alpha,\beta) + m_{03}(\lambda)\, S_3(\alpha,\beta) \tag{4.4}$$

Equation 4.4 is the cornerstone of the SoP-simulation engine which is discussed throughout the next section.

4.3 Poincaré sphere sampling

One of the simplest sampling techniques to vary the α and β angles consists of two nested for-loops. Algorithm 1, shown in pseudo-code, details how using Equation 4.4 for each wavelength of interest, each step in α and all values of β are used to compute the $T_o(\lambda)$ function.

Algorithm 1 Sampling of Poincaré sphere using (α, β) angle pair

```
Read and parse data into individual arrays
Convert Wavelength array [nm] to Frequency array [GHz]
Set step size = step
Using random (α,β) angle pair, simulate full spectrum range

    Repeat until valid minimum insertion loss frequency found
    if more than 25 angle pairs attempted, stop program and return error

Set Centre Frequency = peak of spectra as initial guess
Create array subset: Centre Frequency ± Range [GHz]

    For i = 0 to step
    α = πi/step
        For j = 0 to step/4
            β = 2πj/step
            Compute T0(λ) ∀λ, using (α,β) pair
            Analyze T0(λ) trace to:
          ▷ store desired criterion-related parameters
          ▷ store corresponding (α,β) pair
        Next j
    Next i

Return extremes of decision criterion and corresponding (α,β) pairs
```

To further reduce the time needed to cover the whole Poincaré sphere, a reduction in simulated wavelength range is applied after a randomly selected angle pair is used to simulate the DUT response across the whole operating wavelength range. This allows an initial guess of the centre frequency to be made by looking for the peak value of the resulting simulated transmission spectrum. Following this initial simulation, a cropping window is centered upon the centre frequency estimate to reduce the wavelength range used. The most significant polarization dependent variations are assumed to occur within the main lobe of the filter shape, while more subtle impacts outside of this cropping window are ignored.

We must define a step size to control the sampling density of the α angle and nested sampling of the β angle. This variable relates directly to the computation time required to cover the whole Poincaré sphere. The number of points simulated as a function of the step variable is shown in Figure 4.4 on the following page.

Figure 4.5 shows the increase in sampling point density on the Poincaré sphere as the value of step is increased. As expected, the overall variation in spectrum becomes less significant

Figure 4.4: Number of points sampled as a function of step size

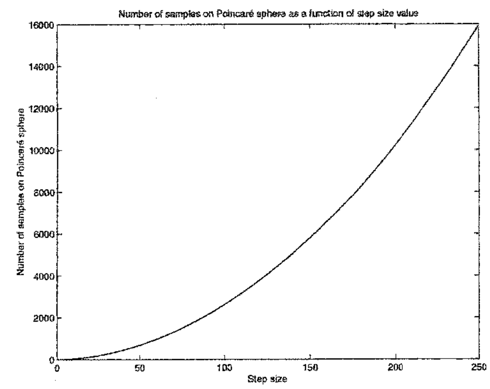

$$\text{number}= (step + 1) \left(\frac{step}{4} + 1\right)$$

as the difference between adjacent α and β angles is reduced. This approach does not provide equidistant points upon the Poincaré sphere. Sampling points end up more spaced out around the equator of the Poincaré sphere and more closely spaced at the poles of the sphere. Clearly, a trade-off between simulation-time and the accuracy of the end results must be taken into consideration. This issue is discussed further in the next section.

Figure 4.5: Coverage of Poincaré sphere as a function of number of steps

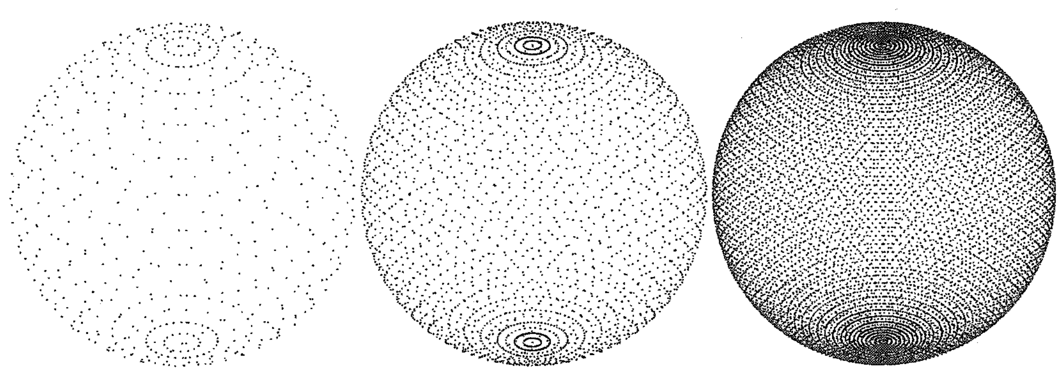

(a) Step = 60, 252 points (b) Step = 124, 4000 points (c) Step = 252, 16192 points

4.3.1 State of polarization simulation results

Throughout this section different simulation results of polarization-compensated and polarization-uncompensated DUTs are presented, for a constant value of the β angle. Figure 4.6 shows the path traveled upon the Poincaré sphere by varying α from 0 to π rad/s, while keeping $\beta = 1$rad/s, or as the half-waveplate is kept stable and the quarter-waveplate is rotated.

Figure 4.7 shows the transmission spectra using different projections for a polarization-

Figure 4.6: Coverage of Poincaré sphere for constant $\beta = 1\text{rad/s}$,

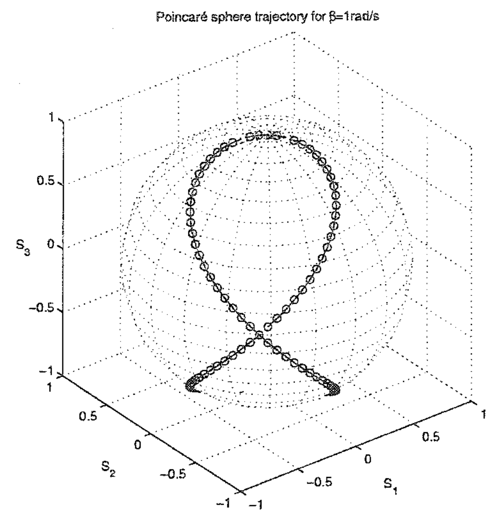

uncompensated DUT, which shows large variation in transmission spectrum as a function of the α angle. The large variation in insertion loss and centre frequency as a function of varying incident SoP is very obvious as no polarization compensator is present to minimize the polarization dependence of the transmission spectrum for different incident SoPs. The bottom subfigures show the matched results between the side-view for a constant β angle and the calculated $T_{0_{MAX}}(\lambda)$ and $T_{0_{MIN}}(\lambda)$ spectra. This limited set of simulated incident SoPs yields spectra that is confined to the limits of the extremes of insertion loss as described in Section 3.2.3.

In the same fashion, Figure 4.8 on page 53 shows the variation in transmission spectra for a polarization-compensated DUT. As expected, the variation in the centre frequency and insertion loss as a function of varying incident SoP, is much less pronounced due to the presence of the polarization compensator. The bottom subfigures also show closely matched results between the side-view for a constant β angle simulation and the calculated $T_{0_{MAX}}(\lambda)$ and $T_{0_{MIN}}(\lambda)$ spectra.

The SoP-simulation engine can be used to evaluate a DUT's performance across any desired fully-polarized incident SoP on the Poincaré sphere, simply by varying the (α, β) angle pair. The results of these simulations fall within the calculated extremes of insertion loss spectra.

Different analysis criterion combined with full coverage of the Poincaré sphere, meant to extract the extreme SoPs corresponding to the TE and TM incident SoP, can be evaluated.

4.3.2 Extreme centre frequency decision criterion

Given enough computation time, a large number of spectra can be analyzed for any given parameter. Results of this analysis may then be used to attempt to isolate the TE and TM modes.

One such parameter that can be analyzed is the centre frequency of the filter response of the channel. Careful design of the polarization compensator aims to minimize any variation of the filter shape and centre frequency for all possible incident SoPs by influencing the effective

Figure 4.7: Polarization-uncompensated spectrum for constant $\beta = 1rad/s$

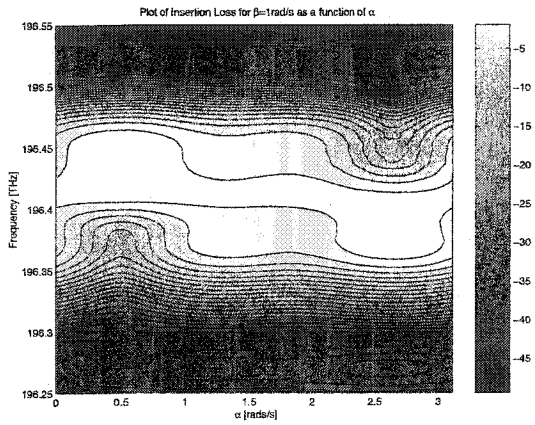

(a) Top-view or Mercator projection

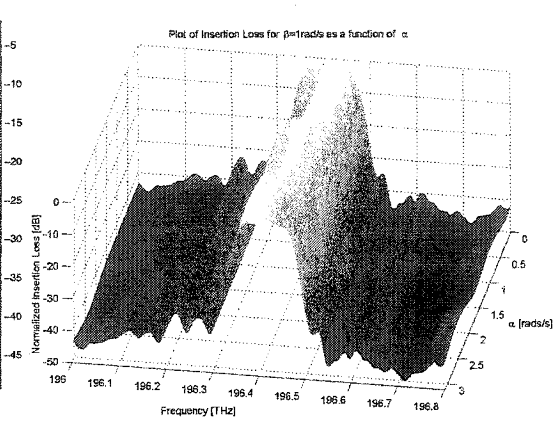

(b) 3-dimensional view

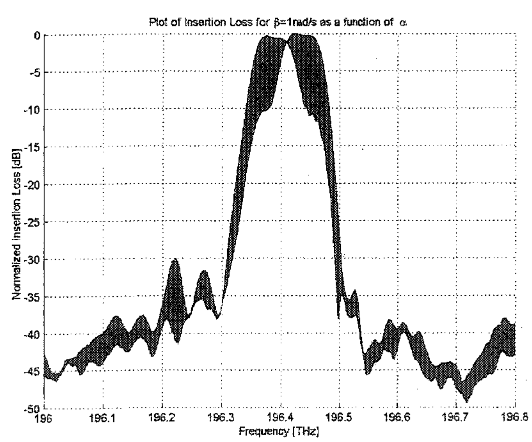

(c) Side view of simulated spectrum

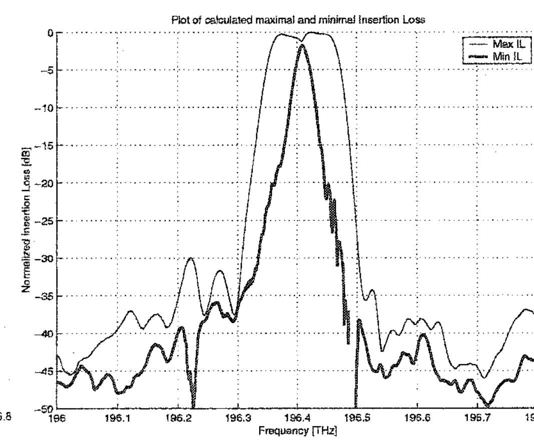

(d) Calculated maximum and minimum spectrum

wave velocities of the TE and TM modes.

The polarization compensator design aims to reduce the PDf, by over and under compensating the intrinsic birefringence of the material around a chosen central nominal wavelength. The aim is to minimize the PDf to a more acceptable level across the overall wavelength range depending on the type of PIC product being designed. Details on the design and integration of the polarization compensator have been detailed in (21).

For each (α, β) angle pair, the centre frequency, f_c, of the corresponding simulated spectrum is evaluated. As detailed in Section 4.3.1, the extremes of f_c and their corresponding (α, β) angles pair are stored. The corresponding Stokes vectors can be used to simulate the spectra over the full operating wavelength range, termed from this point on the SoP_1 and SoP_2 spectrum, which are saved to a new data file. The subtraction of the two extreme f_c yields the absolute value of PDf, or worst-case absolute PDf value.

Figure 4.9 shows the variation of the centre frequency when β is kept constant to 1rad/s,

Figure 4.8: Polarization-compensated spectrum for constant $\beta = 1rad/s$

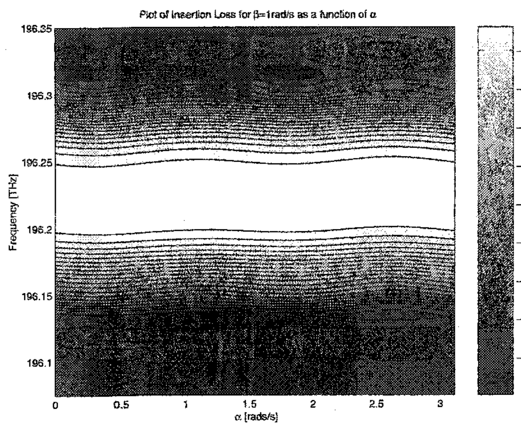

(a) Top-view or Mercator projection

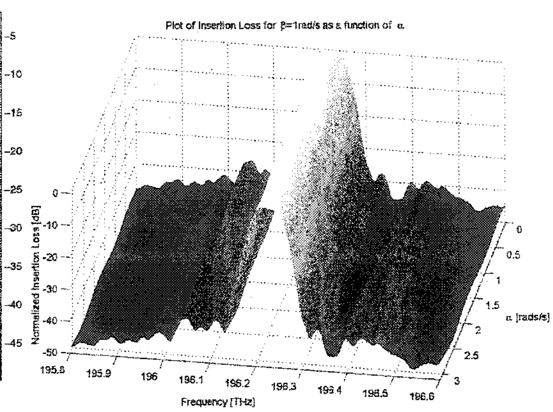

(b) Variation of compensated die insertion loss spectrum

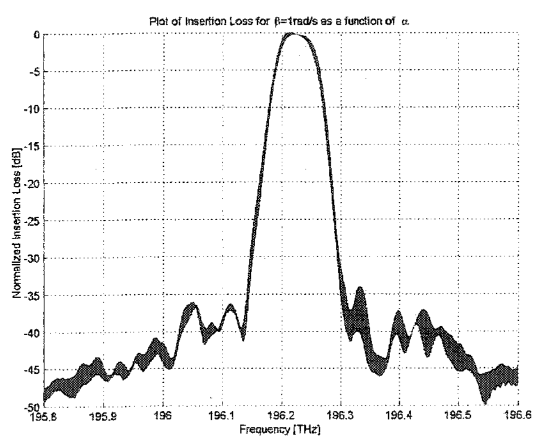

(c) Side view of simulated spectrum

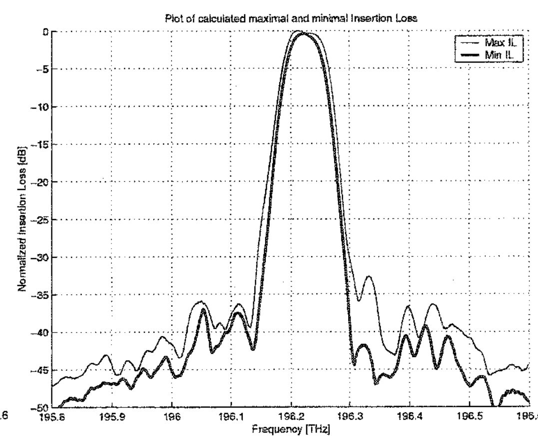

(d) Calculated maximum and minimum spectrum

and α is varied from 0 to π rads/s.

As discussed above, the choice of the step size has a direct impact on the time taken to evaluate and determine the channel's PDf. The minimum number of incident SoPs required to ensure accurate enough results has to be evaluated. Given the wavelength step in the measured spectrum when using the SWS system is 3pm, the overall error in polarization dependent centre wavelength, which is also referred to as Polarization Dependent Lambda (PDλ) was of the order of ± 2.1pm.

Step values above 300 yield no significant variation in PDλ and PDf, as seen in Figure 4.10. This is equivalent to sampling more than 22,000 incident SoPs. The same type of analysis was performed on the impact of the width of the cropping window and must be left wide enough for the different performance parameter extraction algorithms to be executed appropriately. The width of the cropping window will also influence the overall simulation time.

To ease the visualization of the impact of varying the incident SoP on the centre fre-

Figure 4.9: Plot of centre frequency for varying α angle and constant $\beta = 1\text{rad/s}$

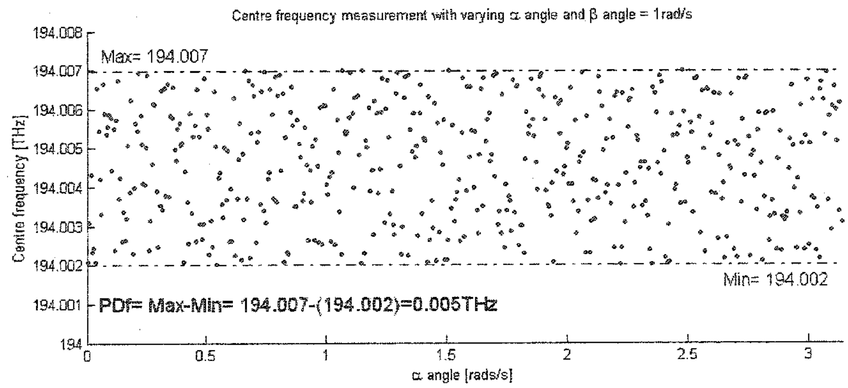

Figure 4.10: Convergence of PDλ/PDf results with increased sampling density

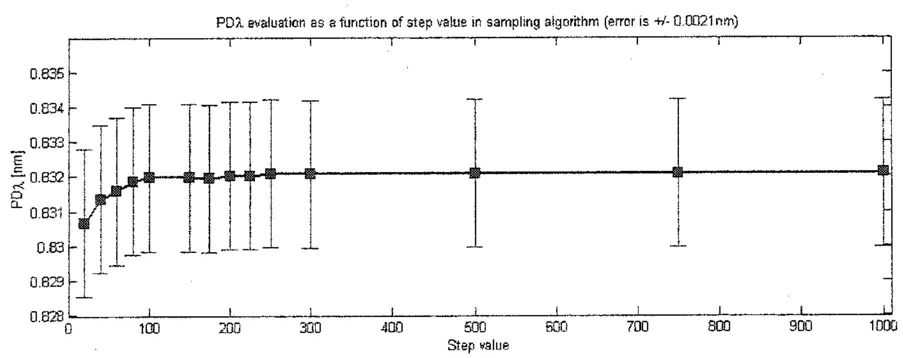

quency, a different visualization approach was used to map performance parameters across the whole Poincaré sphere. Topographic or Mercator projection-like models were used to flatten out the surface of the Poincaré sphere and ease the investigation of anomalies or unexplained variations in the parameters being investigated. It should be noted that the transposing of a 3-dimensional surface onto a 2-dimensional surface creates some unavoidable distortions, still this new projection was found to be more intuitive especially when evaluating different decision criterion.

The 3-dimensional sampling scheme based on (α, β) angle pairs and Stokes vector is converted to a 2-dimensional scheme based on spherical coordinates, and using ϕ and θ angles, as described in Figure 4.11. The corresponding equations used to convert ϕ and θ angles to the Stokes vector components S_1, S_2 and S_3 terms are also shown. Sampling is done between 0 and 2π for the θ angle (traveling along the equator) and from 0 to π for the ϕ angle (traveling from the north to the south pole).

Figure 4.12 shows the projection of the centre frequency for a polarization-uncompensated DUT, across the whole Poincaré sphere. The x- and y-axis representing the θ and ϕ angles, respectively

Figure 4.11: Spherical coordinates conversion to Stokes vectors

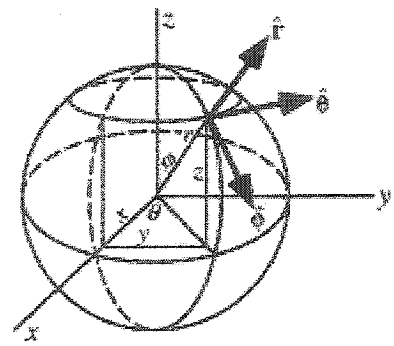

$$\begin{aligned} S_1 &= \cos(\theta)\sin(\phi) \\ S_2 &= \sin(\theta)\sin(\phi) \\ S_3 &= \cos(\phi) \end{aligned}$$

Figure 4.12: Mercator projection of centre frequency for uncompensated die

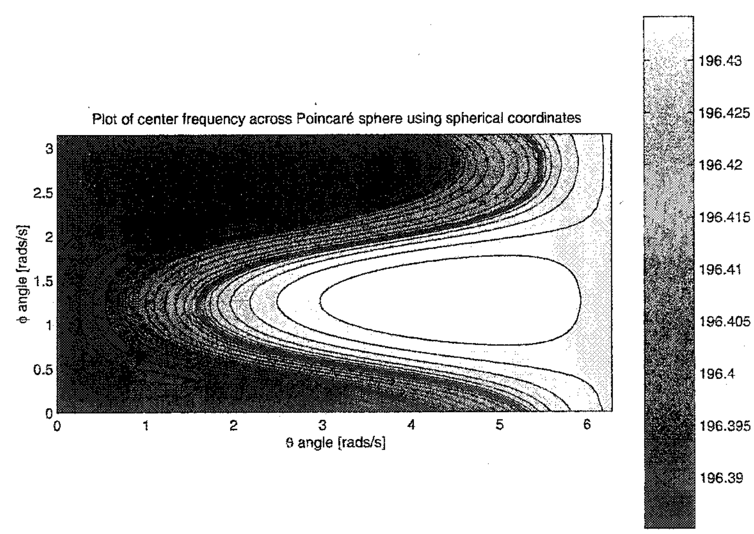

This plot shows a global maxima and minima corresponding to the largest and smallest extracted centre frequencies. These are said to be orthogonal since they are on opposite sides of the Poincaré sphere. They are approximately spaced by $\frac{\pi}{2}$rads/s in the ϕ-axis (north and south hemisphere) and by around π rads/s in the θ-axis (east and west direction). These maximas cover large areas of the Poincaré sphere showing that the step size and sampling grid density did not require to be very dense to find these extremes. It should be noted that a large surface on a Mercator projection may in fact be a small surface area upon a sphere[1] . This DUT, having

[1] This is the same distortion effect seen when the surface of the Earth is plotted onto a map in a Mercator projection. For example. the south Pole may seem as large as all of Europe and Asia. For more information on Mercator projections, visit (41).

no polarization compensator, is expected to have clearly defined extremes of centre frequency. Hence this criterion could have been used to find a close match to TE and TM incident SoPs, termed SoP_1 and SoP_2.

Also noticeable is an S-shape plateau surrounding the global minima and maxima. This would correspond to the circumference of the Poincaré sphere matching an equal mix of TE and TM incident SoP. This plateau can be seen to correspond to the new equator of the redefined poles located at the global minima and maxima. With Mercator projections, the equator defined by the global maxima and local minima poles defines an S-shaped structure which upon a sphere would be equidistant from the two poles if the curved surface was traveled along different latitude lines.

Extremes of centre frequency seem suitable to isolate the TE and TM modes for polarization-uncompensated DUTs, but some issues with well compensated DUTs had been noticed. Enhancements were required to further increase the confidence in extracted TE and TM modes.

4.3.3 Extreme insertion loss decision criterion

For polarization-compensated DUTs it seemed that using extremes of insertion loss or responsivity should yield a better indicator of excitation with TE or TM incident SoPs. The overall variation of PDf is not as obvious.

Figure 3.5 on page 28 shows the tracking of extremes of insertion loss in a polarization scrambler setup or PDL meter-like instrument. A similar plot for centre frequency is shown in Figure 4.9. Contrary to a polarization scrambler or PDL-meter, the simulated polarization controller monitors the insertion loss *at the centre frequency* of the filter main lobe instead of at a single constant wavelength. The (α, β) angle pair which yields extremes of insertion loss can be used to simulate the SoP_1 and SoP_2 spectra and save them to a new data file for further analysis. Figure 4.13 shows a Mercator projection for this criterion. A global maxima does seem to match the global maxima of the centre frequency plot, while the second local maxima matches the global minima in centre frequency performance. Also noticeable is the same S-shaped plateau of global minima which seems to correspond to an equal mix of the TE and TM incident SoPs.

This plot does not show a clear relationship between a global maxima and minima. A lot more fluctuations can be seen in the contour curves, which does not indicate a smooth transition as the incident SoP is changed. This entails the risk of finding largely different results as a function of the sampling density and the sequence of sampling of the Poincaré sphere. The first (α, β) angle pair to reach an extreme value of insertion loss would be kept as the final solution if not surpassed, even though many other points may have the same exact insertion loss.

This sample had about 3GHz of PDf. The extremes of centre frequency were more appropriate to determine the closest match to TE and TM, termed SoP_1 and SoP_2. The extremes of insertion loss would not have been an appropriate criterion. Many different SoPs could have been chosen as the minimal insertion loss point due to the mix of TE and TM yielding the lowest value of insertion loss. Unfortunately, this mix of TE and TM modes may also combine constructively, depending on the level of PDf and PDL of the DUT, and may show the maximal insertion loss for different DUTs.

Figure 4.13: Mercator projection of insertion loss for uncompensated die

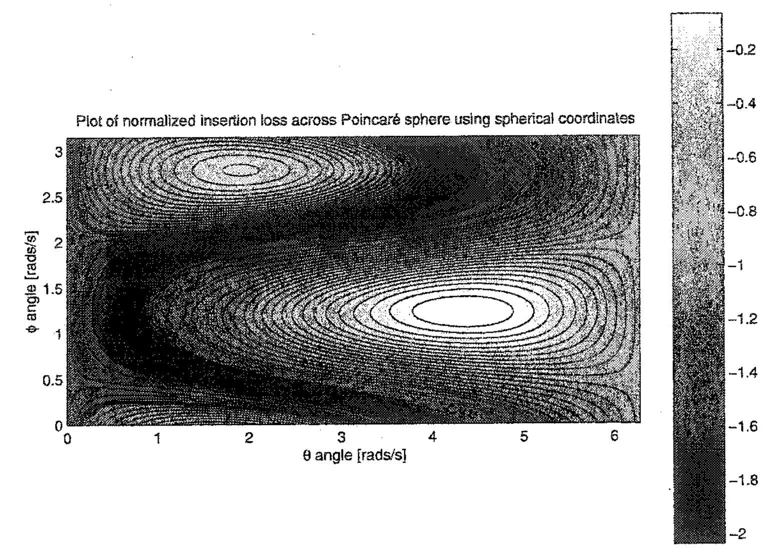

As with some types of Mercator projections the equator, defined by the global maxima and local minima poles, defines a similar S-shaped structure, which upon a sphere would be equidistant from the two poles along latitude lines.

For this DUT, the extremes of insertion loss would not have been the most appropriate criterion to find the TE and TM modes.

4.3.4 Extreme centre frequency and insertion loss combined

The extremes of insertion loss were inappropriate in some cases. The same could be assumed of the extremes of centre frequency, for different DUTs. To optimize the selection of the SoP_1 and SoP_2 spectrum both criteria were combined alongside a new orthogonality parameter which is meant to evaluate the orthogonality of the (α, β) angle pairs found for each criterion.

The (α, β) angle pairs yielding extremes of centre frequency and extremes of insertion loss are both converted to Stokes vectors and the orthogonality factor for each criterion is evaluated. Nominal TE and TM incident Stokes vectors have the electrical field of their TEM waves oriented at 90 degrees from each other. On a Poincaré sphere this corresponds to having Stokes vectors which point in opposite directions, or in a mathematical sense, the dot product of the Stokes vectors should be equal to -1, as seen in Equation 4.5.

$$\overrightarrow{S_{TE}} \bullet \overrightarrow{S_{TM}} = -1 \tag{4.5}$$

Which can be expanded as follows:

$$\overrightarrow{S_{TE}} \bullet \overrightarrow{S_{TM}} = S_{1_{TE}} S_{1_{TM}} + S_{2_{TE}} S_{2_{TM}} + S_{3_{TE}} S_{3_{TM}} = -1$$

Assuming $\overrightarrow{S_{TE}} = -\overrightarrow{S_{TM}}$, which would indicate perfect orthogonality on the Poincaré sphere, the above equation becomes (since the Poincaré sphere is a unit-sphere) valid. For points on the surface of the Poincaré sphere:

$$\begin{aligned}\overrightarrow{S_{TE}} \bullet \overrightarrow{S_{TM}} &= -S_{1_{TE}} S_{1_{TE}} - S_{2_{TE}} S_{2_{TE}} - S_{3_{TE}} S_{3_{TE}} \\ &= -\left(S_{1_{TE}}^2 + S_{2_{TE}}^2 + S_{3_{TE}}^2\right) \\ &= -1\end{aligned} \quad (4.6)$$

This allows a numerical comparison of the two criteria used. After the simulation and analysis of all spectra as defined by the **step** variable, the computation of the orthogonality factor using PDf, $O_f^{L;xdB}$, and PDL, $O_L^{L;xdB}$, allows the selection of the most suited approach; the criterion with its orthogonality factor closest to -1 sees its corresponding (α, β) angle pair used to simulate the SoP_1 and SoP_2 spectrum.

This allowed the continued use of these two criterion, and the occurrence of odd results was largely reduced, yet, a single annoyance still prevailed.

Even by choosing from the two solutions provided by using these two criteria, most channels analyzed would not result in a dot product of -1, indicating that both criterion were not ideal. Since the resulting incident Stokes vector were not exactly orthogonal to each other, even if their orthogonality factors were often very close to -1, no guarantee could be offered that these were in fact really orthogonal incident SoPs.

Furthermore, some issues with the filter main lobe shape and noise on our electrical measurement system, as discussed in Section 3.3, affected the accuracy of the insertion loss measurement as there was an artifact ripple seen at the top of the main filter lobe. This affected the minimum insertion loss, IL_{MIN}, which influenced the accuracy of the extracted centre frequency and the value returned for the insertion loss at the centre frequency.

Attempts were made to extract these parameters by using parameter definitions based on the centre frequency found using the values found 10dB below the peak value, instead of the typical 3dB. Still, the fact that the analysis was highly dependent on the criterion and the parameter definition used motivated further investigations into new analysis criteria. As discussed in Section 4.4, a solution based solely on raw measurement data, instead of any extracted parameters, seemed more appropriate.

4.3.5 Advantages and disadvantages of sampling criteria

The sampling approach and different selection criteria described throughout Section 4.3 offered an unmatched view of the polarization-dependent performance of the DUT for which Mueller matrix terms had been extracted. The advantages and disadvantages of this approach are detailed in this section.

By enabling the extraction of all possible spectrum this technique goes further than the original PDL Mueller-matrix based technique or any scrambler-type measurement setup. This technique goes further by enabling spectra for any desired incident SoP to be visualized instead of only seeing the potential or measured extremes as in the other measurement techniques mentioned.

While matrix-based measurements do increase the accuracy and repeatability of the DUT measurements, the associated analysis remains time consuming. Even though many variables may be optimized to reduce the required computation time, the fact remains that some of the parameters used in different analysis criteria are affected by the variation in the settings used to obtain said parameters. This adds confusion to the parameter selection and settings optimization process. The ideal criteria would be less subjective, relying only on measured results rather than analyzed spectrum.

The time taken to simulate the different spectrum is largely influenced by the following parameters:

- ▷ **step** variable definition, or density of sampling of Poincaré sphere;
- ▷ range of spectra around main lobe used in computation;
- ▷ wavelength sampling step;
- ▷ number of parameters analyzed and associated computation time;
- ▷ computing resources available for analysis.

To help speed up testing the analysis of the Mueller matrix terms was performed by an analysis client[2] , which ran as a background service on the different PCs of the T&M group at MetroPhotonics Inc. This analysis was originally performed at the testing stations and delayed subsequent measurements of the remaining DUT channels. The analysis client allowed larger numbers of incident Stokes vectors to be analyzed with little delay in testing or impact on overall testing capacity. Only the main filter lobe could be effectively included in any of the sampling approaches. The different criteria could only be applied to a small span of the overall spectrum. Investigation of the polarization-dependence on some parameters, such as non-adjacent crosstalk, remained inefficient. On the main workstation used to run the analysis client a ± 150GHz range around the centre frequency had to be used to reduce the analysis time to less than two minutes per analyzed DUT channel, while using about $20,000$ points on the Poincaré sphere.

One important limitation of all Mueller matrix based criteria is that, while a pair of orthogonal spectrum can be extracted and different criterion may yield larger confidence that these are indeed good representations of the TE and TM modes, there is no way to decide which of the two modes is the TE mode, and vice-versa, if only one channel's results is known. Additional analysis is required to match the SoP_1 and SoP_2 spectrum to the TE and TM modes. Some rules of thumb may be used, but some residual strain in the epitaxial layers and the combined action of the polarization compensator, may render these rules of thumb useless. In most cases, test structures could be used to extract wafer-growth batch specific results or completed device results could be investigated for educated guesses.

This is the main reason why only the absolute PDf or PDL can be computed. It is normally defined as the difference between the TE and TM modes in non-absolute terms. The polarization compensator design should show a linear regression when PDf is plotted as a function of channel number. Absolute PDf results required new ways of analyzing results and new rules of thumb had to be used to match the results to the expected slope of the absolute value of PDf, if this curve would cross the 0GHz mark.

[2] More details on the MetroPhotonics Inc. analysis client can be found in Appendix D.1.

The resulting (α, β) angle pairs found with these criteria are highly dependent on the parameter definitions and subjective choices made to optimize the analysis and overall testing-time. Noise showing up as a ripple in the main lobe clear passband was a clear indication that using the 3dB level to extract insertion loss and centre frequency was not suitable and other parameter-specific settings could also be affected. The confidence in the selection of the SoP_1 or SoP_2 spectrum and their correspondence to the TE and TM incident SoPs was uncertain with these criteria.

The largest disadvantage of this approach was the fact that the SoP_1 or SoP_2 solutions had no guarantee of orthogonality, their orthogonality factor would get close to the -1 target, but most often would not reach it. This could be compared to stating that the SoP_1 or SoP_2 incident Stokes vectors were not purely TE or TM, as some of the TE mode had leaked into the assumed purely TM mode, and vice-versa. The promise of quasi-infinite extinction ratio between the two modes, which is one of the main reasons to avoid the PM-fiber approach (apart from the fact that no PM-fiber is eventually attached to our device) is not fulfilled as hoped.

Assuming the input fiber and device is kept stable during the measurement,only one valid solution should exist; a single pair of orthogonal incident SoPs corresponding to the TE and TM modes must exist and can be isolated.

4.4 Numerical solutions

Due to some of the issues discovered when evaluating the extreme centre frequency and insertion loss criteria based on the sampling of the Poincaré sphere, new approaches aimed at isolating the SoP_1 or SoP_2 incident Stokes vectors were required.

The confusion created by the lack of guarantee that the resulting (α, β) angle pairs would yield orthogonal incident Stokes vectors highly influenced the other approaches discussed throughout this section. Even within a single device, some channels had been found closer to being orthogonal when using extremes of centre frequency while others were found with extremes of insertion loss. The PDf results were not closely matched to the expected linear regressions.

4.4.1 Normalized difference criterion

To avoid the selection of the most suitable criterion based on an orthogonality factor, without a guarantee of perfect orthogonality, an approach which would provide such perfection was investigated. By only sampling half of the Poincaré sphere and always comparing opposite orthogonal SoPs, a new analysis and selection criterion could be applied to the simulated spectra.

By definition, any orthogonal Stokes vector, SoP_1, is opposite to a second Stokes vector, SoP_2, as can be seen in Figure 4.14.

By always looking at guaranteed orthogonal incident Stokes vector pairs, a new criterion focused on comparing the resulting spectrum of the SoP_1 and SoP_2 incident Stokes vectors could be evaluated. This approach only requires sampling of half of the Poincaré sphere, since for each point in the southern hemisphere the corresponding point on the northern hemisphere's spectrum is also simulated.

To avoid any performance parameters, we can investigate a technique meant to assign

Figure 4.14: Poincaré sphere representation of orthogonal sampling approach

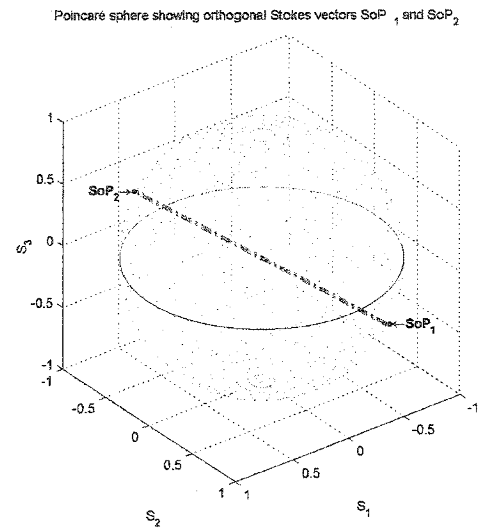

$$\begin{aligned}\overrightarrow{SoP_1} &= -\overrightarrow{SoP_2} \\ \begin{bmatrix} S_1 & S_2 & S_3 \end{bmatrix}^T &= -\begin{bmatrix} S_1 & S_2 & S_3 \end{bmatrix}^T\end{aligned}$$

a numerical value to quantify this difference. This can be compared to finding the base set of orthogonal vectors from which all other SoPs can be expressed as linear combinations. Since the different building blocks each have their own TE and TM modes, the same linear combination rules used for them are assumed to be applicable for overall DUT response, if a valid base set can be isolated.

A simple normalized difference equation can be used to compare different orthogonal SoPs pairs, with no need to take into account parameter definitions.

By using the following equations we can express the difference between the SoP_1 and SoP_2 spectrum, in a single numerical value. Let $f_1(\lambda)$ be the resulting spectrum for the incident Stokes vector SoP_1, and $f_2(\lambda)$ for SoP_2, defined as follows:

$$\begin{aligned} f_1(\lambda) &= m_{00}(\lambda) S_0 + (m_{01}(\lambda) S_1 + m_{02}(\lambda) S_2 + m_{03}(\lambda) S_3) \\ f_2(\lambda) &= m_{00}(\lambda) S_0 - (m_{01}(\lambda) S_1 + m_{02}(\lambda) S_2 + m_{03}(\lambda) S_3) \end{aligned} \tag{4.7}$$

Using these newly defined variables and the α and β sampling approach used to find the extremes of centre frequency and/or insertion loss. The extraction of the following numerical value can be performed by limiting the α-angle from 0 to 90 degrees, thus ensuring the S_3 term would be negative since defined as $S_3(\alpha) = -\sin(2\alpha)$. The SoP_1 Stokes vector is consequently always assigned to the southern hemisphere of the Poincaré sphere.

For each of the (α, β) angle pairs a numerical value, ξ, corresponding to the normalized difference between the f_1 and f_2 functions, is defined as follows:

$$\xi(\alpha,\beta) = 1 - \frac{\sum_\lambda \left(f_{1_{(\alpha,\beta)}}(\lambda) - f_{2_{(\alpha,\beta)}}(\lambda)\right)^2}{\sqrt{\sum_\lambda \left(f^2_{1_{(\alpha,\beta)}}(\lambda)\, f^2_{2_{(\alpha,\beta)}}(\lambda)\right)}} \tag{4.8}$$

For Equation 4.8, the following observations can be made:

- ▷ The larger the difference between the f_1 and f_2 spectrum across the desired wavelength range, the smaller the value of ξ;
- ▷ If the $f_1(\lambda)$ and $f_2(\lambda)$ spectrum are identical then the value of ξ will be equal to 1. This may happen for a perfect mix of TE and TM modes, for example.

By tracking which (α, β) angle pair yields the smallest value of ξ, the corresponding incident SoP_1 and SoP_2 Stokes vector pair can be used to simulate the full-wavelength range. These spectra are then saved the spectrum to a new data text file, as for other criteria described earlier. Polarization-dependent parameters can also be computed, such as PDf and PDL for this solution.

The same type of Mercator projection can be used to investigate the effectiveness of this criterion. Figure 4.15 shows the resulting projection of the normalized difference parameter for the same DUT used in Figures 4.12 and 4.13. Since only half the sphere is simulated (α-angle from 0 to 90 degrees), the whole sphere (α-angle from 0 to 180 degrees) is still plotted to ease comparison of different criteria.

Figure 4.15: Mercator projection of normalized difference for uncompensated die

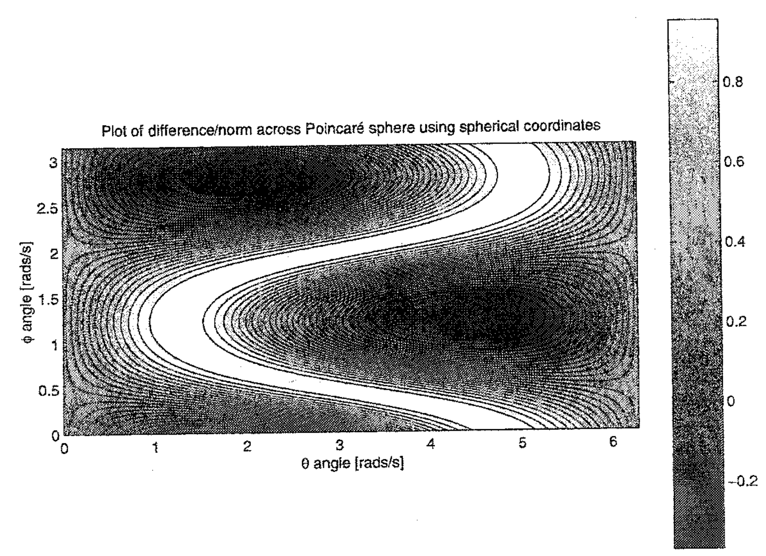

As in Figures 4.12 and 4.13, the same S-shape plateau can be seen. This plateau reaches a value of $\xi = 1$, which corresponds to an equal mix of TE and TM. The newly defined poles corresponding to the symmetric global maximas defines a new equator which corresponds to the S-shaped plateau, seen once more. This increases the confidence in the validity of linear combinations using the two extreme orthogonal SoPs as a base set to appropriately recreate all incident Stokes vectors.

The global minima does correspond to the extremes of the centre frequency Mercator projection, as well as the global maxima of insertion loss. The minima of insertion loss is seen to match the mix of TE and TM S-shaped plateau.

Figure 4.16 shows the Mercator projections of all three analysis criteria. Clearly the normalized difference Mercator projection shows the most abrupt and regular convergence towards the global minima of the three criterion. The inclusion of divergence vectors onto the plots would clearly show this.

Figure 4.16: Mercator projection of all three analysis criteria

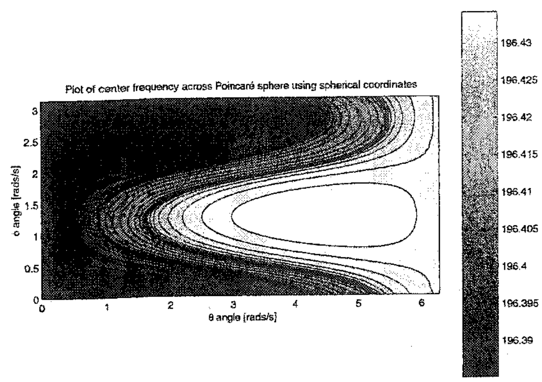

(a) Mercator projection of centre frequency

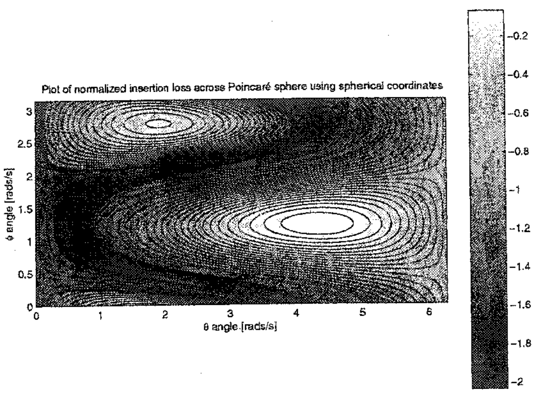

(b) Mercator projection of insertion loss

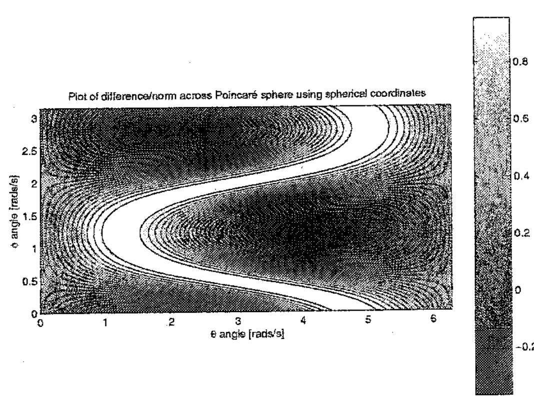

(c) Mercator projection of normalized difference

4.4.2 Advantages of normalized difference criterion

This new criterion and analysis approach offers many advantages, namely parameter definition are avoided. Only the obtained Mueller matrix terms and resulting simulated spectrum are used in the analysis. By definition, the SoP_1 and SoP_2 incident Stokes vectors are orthogonal and, in consequence, a single solution is returned. The added step of selecting the most orthogonal solution as defined by the orthogonality factors, $O_f^{L,xdB}$ and $O_L^{L,xdB}$, is unnecessary.

Since only half the Poincaré sphere needs to be sampled using the α and β angles, the computational effort associating with the sampling itself is halved.

As for other Mueller matrix terms analysis techniques, the SoP_1 and SoP_2 solution cannot be assigned to TE and TM without some prior knowledge of the epitaxial layers, residual strain, and other growth related parameters. Some rules of thumb can be used if this distinction is required.

By definition, the SoP_1 incident Stokes vector always lands on the southern hemisphere. Additional analysis steps were added within the analysis client to swap the SoP_1 and SoP_2 incident Stokes vectors if the dot product of adjacent channels SoP_1 vectors were found to be negative. In other words, if their Stokes vectors were found to point in opposite directions. This would happen when the solution vector is very close to the equator of the Poincaré sphere and adjacent channels could have S_3 terms very close to 0. As a DUT is measured in a relatively short period of time, the orthogonal incident Stokes vectors of the SoP_1 and SoP_2 incident SoPs for all channels should all be located within small areas upon the Poincaré sphere, respectively.

After the measurement of all channels is completed, it is possible to decide which of SoP_1 or SoP_2 corresponds to the TM mode. By design, the polarization compensator is meant to affect the incident TM mode centre frequencies more than the TE mode centre frequencies. Hence, by looking at the centre frequencies of all channels after data is captured, the SoP_i state which shows the largest fluctuations across the operating wavelength range, or equivalently the largest slope of PDf when plotted as a function of channel number, is assigned to the TM mode and the other to the TE mode. While this could be done within the analysis client, it would involve modifying already saved data files. Therefore, this extra analysis is only used when non-absolute terms PDf results are required for RCA-type analysis efforts. This was only possible when all incident SoP_i solution were guaranteed to point in the same direction for each channel of the DUT.

As this criterion is still based on a sampling approach, only a limited spectral range was used to compute the ξ terms. Spectral structures outside of the main lobe have been shown to be good indicators of polarization-dependence. But, as many thousands points upon the Poincaré sphere were still being sampled and even though the additional computational effort of extracting parameters is removed, the spectral range considered still needed to be reduced to maintain the arbitrarily chosen benchmark of less than two minutes per channel analyzed. A larger number of points on the Poincaré sphere could be sampled in this two minute window, but if the same number of points was used, the analysis averaged about 30 seconds on the same PC used for the extreme centre frequency and insertion loss criteria.

The last analysis technique investigated aimed to remove the need to sample individual incident Stokes vectors by evaluating the response across the whole wavelength range for all possible SoPs in a single system of equations.

4.4.3 Extreme most orthogonal numerical analysis

Although the normalized difference criterion had proven very efficient and resulting PDf versus channel number plots were very close to the predicted design results, the need to sample thousands of incident Stokes vectors still involved large computational efforts.

The technique described in (17) uses a quadratic equation to find the extremes of insertion loss, $T_{0_{MAX}}(\lambda)$ and $T_{0_{MIN}}(\lambda)$, as described by Equations 3.12 and 3.13, on an individual wavelength-basis, which are also found to be orthogonal on the Poincaré sphere. These extremes are then used to extract the PDL spectrum.

Expanding upon this approach and the normalized difference criterion described in Section 4.4.1, the most orthogonal numerical analysis approach aims to take into account the whole spectrum to obtain a wavelength-independent orthogonal solution. Rather than finding extremes for individual wavelengths, it aims to extract the extreme orthogonal spectra for SoP_1 and SoP_2, which should represent the TE and TM spectra, or vice-versa.

This new analysis approach takes into account all Mueller matrix terms across the whole acquired wavelength range. It includes the investigation of structures outside of the main lobe, which have been shown to also exhibit polarization dependent spectrum variation, but had previously been cropped out to reduce the computational effort.

As for the normalized difference criterion, this approach also does not create confusion due to parameter definitions. Orthogonality of the solution pair of Stokes vectors is also guaranteed by definition.

The same solution as for the numerical sampling normalized difference criterion is obtained, since this new approach is analogous to using an infinitely dense sampling grid to sample the Poincaré sphere. This new approach has the added advantage of only requiring a few mathematical operations to yield the final solution.

As shown before, the following equations represent the spectral response variation due to the influence of a given incident Stokes vector pair opposite to each other. The $m_{00}(\lambda)\, S_0$ terms were removed from Equation 4.7, yielding the following:

$$\begin{aligned} f_1^{'}(\lambda) &= \left(m_{01}(\lambda)\, S_1 + m_{02}(\lambda)\, S_2 + m_{03}(\lambda)\, S_3\right) \\ f_2^{'}(\lambda) &= -\left(m_{01}(\lambda)\, S_1 + m_{02}(\lambda)\, S_2 + m_{03}(\lambda)\, S_3\right) \end{aligned} \tag{4.9}$$

The goal remains to find the vector, $\begin{bmatrix} S_1 & S_2 & S_3 \end{bmatrix}$, which maximizes the difference between the $f_1^{'}(\lambda)$ and $f_2^{'}(\lambda)$ equations. A simple way to define this optimization problem is to define a new equation as follows:

$$\psi = \left(\sum_{\lambda}\left(f_1^{'}(\lambda) - f_2^{'}(\lambda)\right)^2\right) \rightarrow max \tag{4.10}$$

Which, since $f_1^{'}(\lambda) \equiv -f_2^{'}(\lambda)$, can be rewritten as

$$\psi = \sum_{\lambda}\left(2f_1^{'}(\lambda)\right)^2 = \sum_{\lambda} 4\left(m_{01}(\lambda)\, S_1 + m_{02}(\lambda)\, S_2 + m_{03}(\lambda)\, S_3\right)^2$$

or as:

$$\frac{\psi}{4}=\sum_{\lambda}\left(m_{01}^{2}(\lambda)S_{1}^{2}+m_{01}(\lambda)m_{02}(\lambda)S_{1}S_{2}+m_{01}(\lambda)m_{03}(\lambda)S_{1}S_{3}\right.$$
$$+m_{02}(\lambda)m_{01}(\lambda)S_{2}S_{1}+m_{02}^{2}(\lambda)S_{2}^{2}+m_{02}(\lambda)m_{03}(\lambda)S_{2}S_{3}$$
$$\left.+m_{03}(\lambda)m_{01}(\lambda)S_{3}S_{1}+m_{03}(\lambda)m_{02}(\lambda)S_{3}S_{2}+m_{03}^{2}(\lambda)S_{3}^{2}\right)\quad(4.11)$$

Introducing the following notation:

$$M_{ij}\equiv\sum_{\lambda}\left(m_{0i}(\lambda)m_{0j}(\lambda)\right)=M_{ji}$$

Equation 4.11 can be rewritten as:

$$\psi=\left(M_{11}S_{1}^{2}+M_{12}S_{1}S_{2}+M_{13}S_{1}S_{3}+M_{21}S_{2}S_{1}+M_{22}S_{2}^{2}\right.$$
$$\left.+M_{23}S_{2}S_{3}+M_{31}S_{3}S_{1}+M_{32}S_{3}S_{2}+M_{33}S_{3}^{2}\right)\quad(4.12)$$

Which can be rewritten in matrix form as follows:

$$\psi=\begin{bmatrix}S_1 & S_2 & S_3\end{bmatrix}\begin{bmatrix}M_{11} & M_{12} & M_{13}\\ M_{21} & M_{22} & M_{23}\\ M_{31} & M_{32} & M_{33}\end{bmatrix}\begin{bmatrix}S_1\\ S_2\\ S_3\end{bmatrix}=\vec{S}^{T}\mathbf{M}\vec{S}\quad(4.13)$$

where the $\mathbf{M}$ matrix is a symmetric real matrix, since $M_{ij}=M_{ji}$.

The solution of Equation 4.10 is given by the normalized eigenvector, X_i, of matrix $\mathbf{M}$ having the largest eigenvalue, μ_i, which can be found using the Jacobi method.

To prove this, recall that eigenvectors and eigenvalues of a $3x3$ matrix are nontrivial solutions to the equation $\mathbf{M}\vec{X_i}=\mu_i\vec{X_i}$, where $i=1$, 2 or 3.

Any Stokes vector can be expanded as $\vec{S}=aX_1+bX_2+cX_3$, where $(a^2+b^2+c^2)=1$. This allows us to rewrite Equation 4.10 as:

$$\begin{aligned}\psi &= \vec{S}^{T}\mathbf{M}\vec{S}=(aX_1+bX_2+cX_3)^{T}\mathbf{M}(aX_1+bX_2+cX_3)\rightarrow max\\ &= a^2\mu_1+b^2\mu_2+c^2\mu_3\rightarrow max\end{aligned}$$

We maximize ψ by only using the eigenvector with the largest eigenvalue, $max(\mu_1,\mu_2,\mu_3)$, by setting the other two components to 0. The resulting vector may end anywhere in the three-dimensional space. Scaling it to unit length will not modify the ratio of linear vertical, horizontal or circular polarizations and ensure the final solution falls upon the Poincaré sphere's surface resulting in a fully polarized SoP.

Thus the eigenvector, $\vec{S_i}$, with the largest eigenvalue, μ_i, maximizes the difference in the orthogonal spectra. The eigenvector, $\vec{S_i}$, can be assigned to the SoP_1 incident Stokes vector, while its opposite, $-\vec{S_i}$, can be assigned to the SoP_2 incident Stokes vector.

This optimization problem is reduced to the diagonalization of a 3 by 3 symmetrical quadratic form. This approach yields a single solution with very little computational efforts. Since the professional version of the LabVIEW programming environment has a built-in eigenvalue solver, the main computational effort consists of computing the six unique M_{ij} terms over all available wavelength and building the $\mathbf{M}$ matrix. Solving to determine the eigenvectors and corresponding eigenvalues of this matrix are handled by the built-in eigenvalue solver.

The largest eigenvalue of the three indicates which corresponding eigenvector should be used to simulate the orthogonal SoP_1 and SoP_2 spectra and save them to text files, after computing all appropriate polarization dependent parameters, such as PDf and PDL.

From simulating thousands of incident Stokes vectors on the Poincaré sphere, we now can obtain the same result after only a few simple mathematical operations by solving a simple optimization problem as described above.

4.5 State of polarization-simulation engine conclusions

No Mercator-type plots can be created for the most orthogonal numerical analysis approach, as seen in Figures 4.12, 4.13 and 4.15. It was found to correlate very well with the normalized difference approach when large enough samples were taken upon the surface of the Poincaré sphere. For these reasons, and the highly correlated results to expected design results of PDf as a function of channel number and PDL, this new approach has been the standard analysis approach for MetroPhotonics Inc. devices at all stages of the production cycle, since its inception.

While the results are almost instantaneous, the analysis is still performed using the analysis client. This analysis has proven efficient enough to be run in parallel with data acquisition software at the measurement workstation. Yet, the analysis client is still the analysis workhorse to ensure the impact on testing-time is minimized and all available resources of the PC test stations are dedicated to handling the data acquisition.

The same issues as with other criterion, namely the fact that the SoP_1 and SoP_2 spectra may not be associated to the actual TE and TM modes, still subsist except after all DUT channels are analyzed. After all data is acquired and analyzed, the SoP_i most affected by the polarization compensator can be assigned to the TM incident SoP. The fact the solution can be extracted so efficiently has opened new avenues for further exploitation of Mueller matrix terms of different types of data.

This is by far the most elegant solution to solve the fundamental problem of isolating the TE and TM modes. Through efficient data acquisition and production-level analysis and testing capacity, whilst ensuring the continued availability of highly accurate data for RCA analysis efforts and fabrication and assembly process metrics data for continued qualification.

Chapter 5

Verification experiments

The TE and TM modes results obtained by using Mueller matrix terms have been scrutinized exhaustively by the T&M and Design groups of MetroPhotonics Inc. Customers and research groups also performed exhaustive qualification and evaluation processes looking at the overall accuracy of our complete specifications sheets as well, in some cases, of internal RCA parameters such as PDf, PDL and PDR. High levels of correlation were reported and documented in evaluation reports by all.

Comparison with other available measurement techniques have yielded enough satisfactory results, enough so that this measurement technique has become the *de facto* standard measurement technique for all T&M production-oriented measurements. Future projects are also being considered for more R&D-oriented analysis requirements, as discussed in Chapter 6.

Through the batch-processing capabilities of the analysis client several thousand individual channels of different MetroPhotonics Inc.'s SurePath^{TM} portfolio products have been analyzed. This chapter introduces some of the verification experiments performed to verify the validity of the algorithms detailed throughout Chapter 4. While the presentation of large data sets would also prove the efficiency of these algorithms, these commonly used tests help prove the concepts without having to investigate each parameters typically analyzed in MetroPhotonics Inc.'s Statistical Process Control (**SPC**) systems.

The use of different equipment, input fibers, temperature control-schemes as well as electrical photocurrent measurement tools create some discrepancies which can be easily explained.

Direct PM-fiber measurement of responsivity aimed at comparing the main filter lobe passband shapes are presented. Followed by PDf results as a function of the channel number were found to match the predicted delta variation of about 5GHz across 43 channels. Comparison of polarization scrambler and Mueller matrix-based measurements from the CSA of extremes of absolute responsivity and corresponding PDR spectra conclude this chapter.

5.1 Comparison with polarization maintaining fiber measurements

Direct comparison of PM-fiber measurements with known incident SoPs is one of the most obvious technique used to compare the TE and TM modes spectra to the simulated spectra from Mueller matrix terms.

While the coupling efficiency difference of the TE and TM modes is more pronounced for PM-fiber measurements, an accurate evaluation of the overall responsivity can be obtained by measuring the input power using a bare-fiber adapter and an optical integration sphere. A simple current meter can then be used to measure the generated photocurrent at each wavelength step for both incident SoPs.

Figure 5.1 shows absolute responsivity measurement results of one of the centre channels of a SurePath Monitor™ die attached to the ceramic carrier, obtained from extracted Mueller matrix terms and PM-fiber measurements. An offset of 150GHz was added to ease the comparison of both techniques.

Figure 5.1: SoP_1 and SoP_2 and TE and TM spectrum comparison

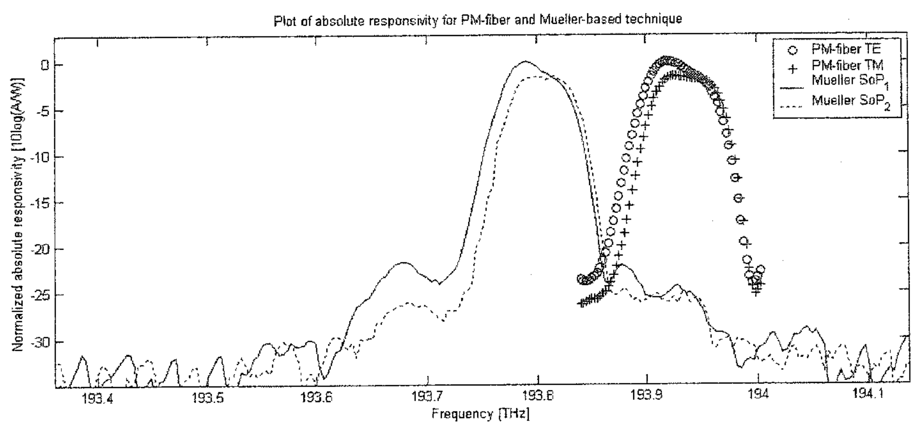

(a) Larger spectrum span view

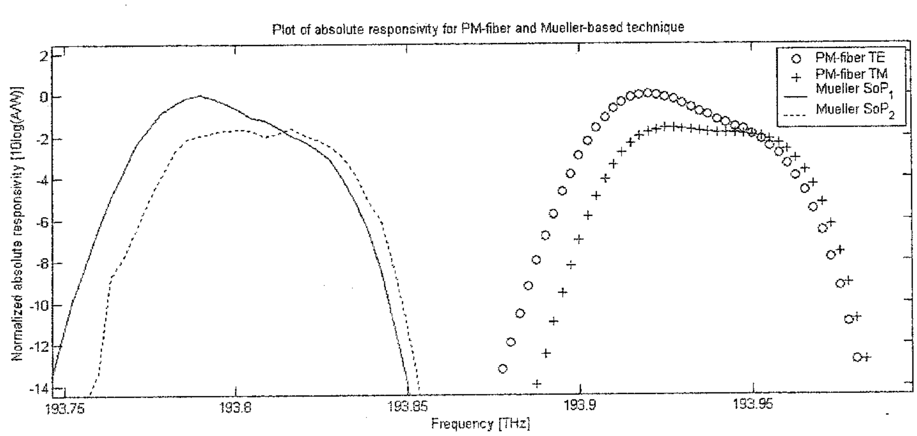

(b) Detailed view of main filter lobe results

These Mueller matrix based measurements show some of the ripple effects seen due to residual 60Hz noise generated by wiring ground loops on the original SWS setup. Still both plots show very comparable results. The SoP_1 and SoP_2 are seen to match the TE and TM spectra measured with a PM-fiber. The PM-fiber measurements were done over a shorter wavelength range due to the longer testing time and to avoid fiber decoupling.

Correlation of passband widths, absolute responsivity and passband shapes further gave credence to the different criterion used to extract TE and TM spectra from the Mueller matrix terms. Confidence in the different algorithms increased greatly as more of these types of tests were performed. This measurement technique was thus found sufficient to isolate the TE and TM modes efficiently enough for production-level capacity requirements while still providing enough accuracy for detailed R&D-oriented RCA efforts.

The impact on the T&M group's testing capacity and head count requirements was obvious, Much less operator-intensive steps were required and testing capacity and usefulness of results were increased significantly.

5.2 Slope of polarization dependent frequency results

One of the most accurate technique to evaluate the accuracy of these novel measurement techniques is to review the PDf of the device as a function of channel number. The geometric shape of the polarization compensator yields very repeatable slopes of the resulting PDf results.

While the nominal values depend largely on any residual strain or external stress effects applied mostly on the DUT's slab waveguide area, the slope depends mainly on the shape of the compensator as seen in Figure 5.2. Following the echelle-grating diffraction different wavelengths travel through different compensator areas, hence their inherent PDf is over- or under-compensated around the central nominal designed frequency.

Figure 5.2: Polarization compensator influence as a function of wavelength

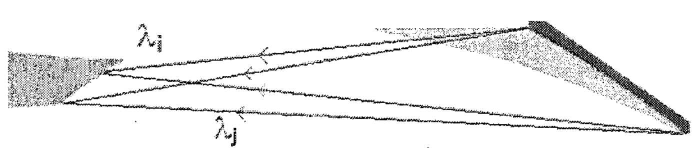

The nominal polarization compensator design yields a variation of about 5GHz from channel 1 to channel 43, following a positive slope when PDf is defined in non-absolute terms. As shown in Figures 5.3 the variation in absolute PDf results closely matches the expected variation of about 5GHz, shown as a linear regression curve. The slope sign change is only related to having SoP_1 assigned to the TE or TM mode depending on which of these orthogonal modes was located to the southern hemisphere of the Poincaré sphere at the test station. Variations in the retardance of the fiber across long periods of time (hours, days, weeks) and the required fiber handling for cleaning and connections displaces the TE and TM incident SoPs upon the Poincaré sphere.

By design for PDf defined using known TE and TM spectrum corresponding centre frequencies the slope is always positive. Special analysis can be performed to assign the appropriate SoP_i to the TM mode since its centre frequency is most affected by the presence of the polarization compensator. This additional step was implemented in other RCA software where the assignment of the TE and TM labels is more crucial.

Figure 5.3: Polarization dependent frequency versus channel number plots

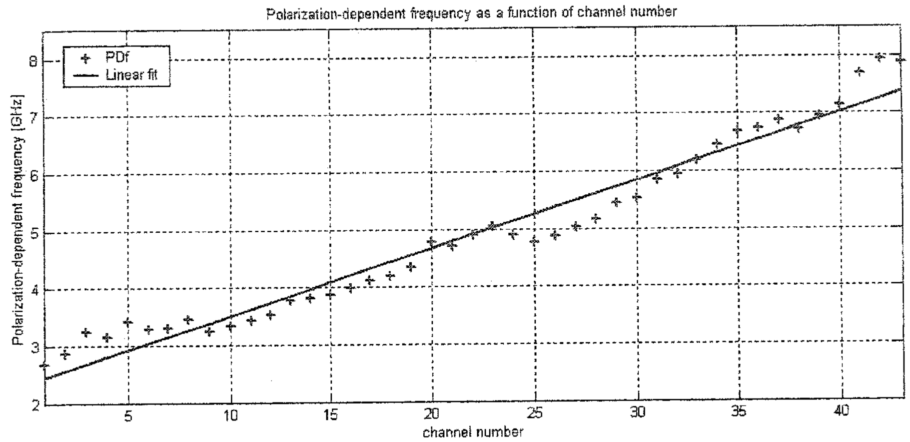

(a) Expected positive slope of PDf results

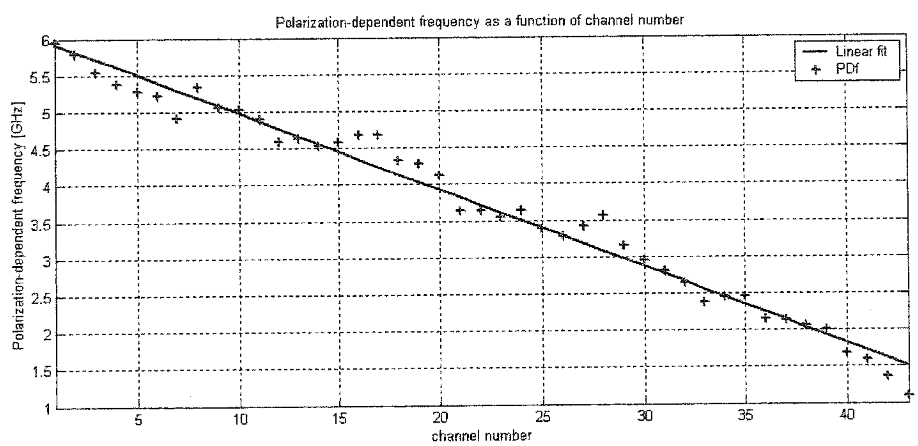

(b) Reversed negative slope of PDf results

Similar plots of PDf as a function of channel number obtained by using PM-fiber measurements or polarization-sampling techniques show much larger variations around their same linear regression curve. Reduced repeatability is also noticed, mainly due to the multiple alignments required and the resulting measurements done at largely different moments in time.

The accuracy of the PDf measurement obtained was deemed sufficient to consider using InP dies as strain and stress sensors for different assembly processes. These include die attachment to ceramic carrier and integration of dies on carrier subassemblies into packages and the subsequent laser welding of the fiber patchcord subassembly. Investigation of any variation in the absolute PDf value or slope variation can be used to pinpoint the processing step in the production line where the stress upon the die was increased or any die bowing may have been induced by uneven epoxy spreading and curing. Changes to the shape factor were also accurately correlated to variable strain in the slab area. The extraction of the TE and TM spectra were essential to the efficient RCA investigations meant to optimize all these different processes.

5.3 Direct comparison with polarizer scrambler results

Although the four-state Mueller matrix PDL measurement technique used has been often verified, this section presents a comparison of polarization scrambler measurements of responsivity. These polarization scrambler-based measurements aimed to extract the maximum and minimum responsivity spectrum, $R_{MAX}(\lambda)$ and $R_{MIN}(\lambda)$, and corresponding PDR of the individual channels of the SurePath Monitor^{TM} product after fiber attachment when a four-state system was unavailable.

Figure 5.4 shows the overlap of polarization scrambler and Mueller matrix results for channels 1, 22 and 43 of a Monitor DUT. The input power reaching the DUT is calibrated using an optical integration sphere, then a current meter is used to measure the generated photocurrent for each wavelength step for several incident SoPs. The ratio of generated photocurrent over the input power reaching the DUT yields the responsivity. An offset of 150GHz was added to ease the comparison of both techniques.

When compared to calculated extremes of responsivity using the technique detailed in Section 3.2.3 these results show very good correlation. Only the main lobe could be captured by the polarization scrambler technique due to time constraints. Once more, the capacity increase of the matrix based techniques is clear, as several minutes are required to obtain accurate main lobe results with a polarizer scrambler technique compared to several seconds when using a Mueller matrix based analysis system.

5.4 Verification experimentation conclusions

Only a sample of all verification experimentations performed could be detailed within this document. More detailed analyses of crosstalk measurement accuracy and impact of noise on the overall measurement accuracy did not fit the scope of this document.

The main approach used to qualify these simulation techniques involves the analysis of data as shown throughout Chapter 4. DUTs measurement results with PM-fiber or other means were compared to simulated results for different analysis criterion using Mercator projections and rigorous statistical analysis of the results obtained.

Early on the operators were asked to perform repeated measurements of reference samples in the daily process of recommissioning the different test stations. This allowed monitoring of the evolution and stability of the test stations. Simple SPC analysis tools were developed to monitor the average and standard deviation of all parameters of interest as well as plotting tools to allow visual feedback to pinpoint any trends. Engineering logs were kept for each stations to insure historical changes were logged and could be used to explain odd results.

The fast-paced environment at MetroPhotonics Inc. complicated any trend charting since new analysis algorithms, parameters and hardware enhancements were always being considered and added to the characterization process, yielding any long-term review difficult. Tightening of the standard deviations could still be tied to hardware modifications indicating more precise and accurate measurements. Direct comparison of the SWS and CSA measurement tools for absolute responsivity measurement did show reduced standard deviations for all parameters on the CSA, which can be explained by the more accurate *in situ* calibration methodologies. On-

Figure 5.4: $R_{MAX}(\lambda)$ and $R_{MIN}(\lambda)$ and polarization scrambler measurements comparison

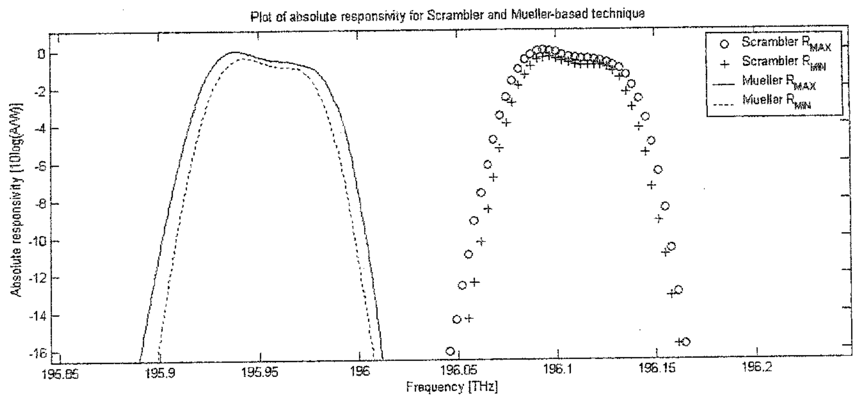

(a) Channel 1 Mueller and polarization scrambler spectra

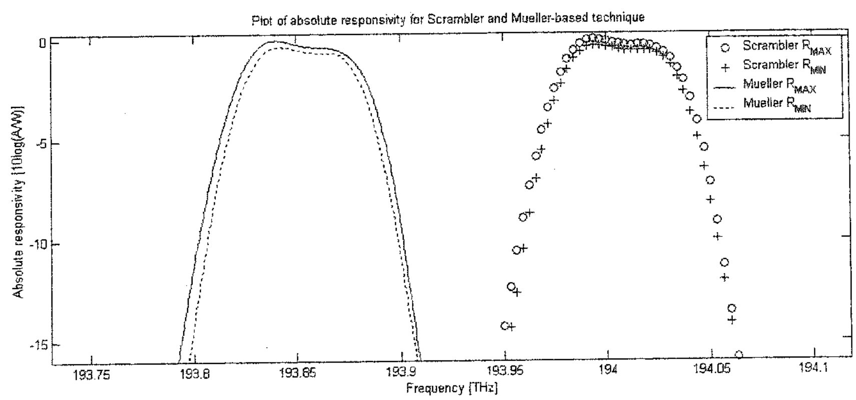

(b) Channel 22 Mueller and polarization scrambler spectra

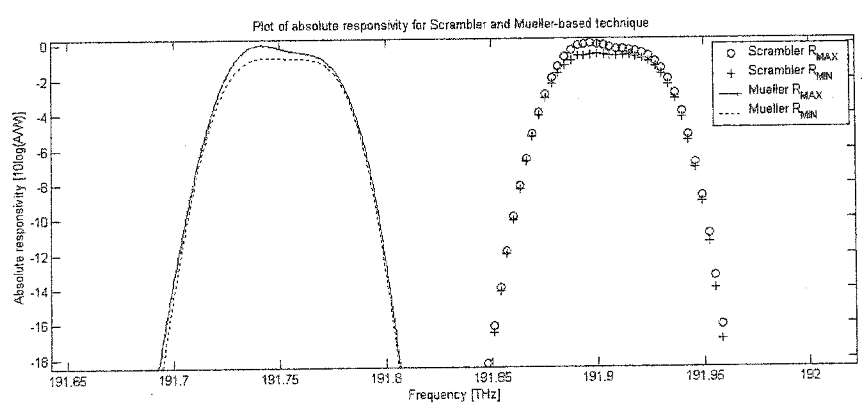

(c) Channel 43 Mueller and polarization scrambler spectra

going calibration and reference traceability to National Institute of Standards and Technology (NIST) or National Research Council Canada (NRC) standards further guaranteed accurate and precise results.

This Mueller matrix based opto-electrical characterization system was considered sufficient to be used as the main tracking tool for Telcordia qualification of the different SurePath™ portfolio sub-assemblies and final packages which are expected to be completed by the end of the summer of 2004.

Compared to earlier measurement techniques the Mueller matrix-based measurement technique has been seen to provide much more accurate results than other measurement techniques.

Chapter 6

Conclusions and future work

Optical networks have been going through profound revolutions over the last few years. The vast deployment of optical amplifiers has profoundly changed the cost structure associated with the deployment of multi-channel DWDM optical links.

The next few years hold the promise of further penetration of optical fibers closer to end-users, in schemes such as Fiber-to-the-Home (**FTTH**) or Fiber-to-the-Premises (**FTTP**), which may increase the number of required optical links tenfold. MetroPhotonics Inc. aims to answer this need by reducing costs of production by using semiconductor processing, integrating novel functionalities into PIC devices, and developing novel efficient testing and data analysis techniques to further increase production capacity.

The integration of electrical functions alongside optical functions enables optical network designers to consider new approaches to provide services to their customers. The novel approach used by MetroPhotonics Inc. to integrated echelle-grating (de)multiplexers with active functionalities, involves many trade-offs to evaluate and optimize the design of the individual building blocks as well as the overall DUT response, as discussed extensively throughout Chapter 2.

Throughout this document different measurement techniques suitable for polarization-dependent optical components were presented, with their respective strengths and weaknesses. Chapter 3 introduced the commonly used OSA or power meter measurement technique as well as the polarization sampling approach. The PM-fiber measurement technique was long considered T&M's only alternative, until more advanced techniques were implemented from the deeper understanding of the inner workings of the Mueller matrix terms-based PDL measurement tool which had been used for passive optical testing.

Focused on Mueller matrix-based analysis approaches, this document showed how these approaches have enabled the T&M group to fully characterize the polarization-dependence of the SurePath^{TM} portfolio products to hopefully satisfy both design-oriented internal and specifications-oriented external customers.

The SoP-simulation engine, presented throughout Chapter 4, used alongside special analysis tools allowed the extraction of the TE and TM spectra from the measurement of only four incident SoPs. Different criteria results were shown in different projections to allow investigation of the extraction of the SoP_1 and SoP_2, which can be associated to the TE and TM modes by investigating their variation in centre frequencies.

This new capability enabled the decommissioning of all production PM-fiber rotation-based test stations, yielding highly increased testing capacity without the need for any headcount increase in the T&M group, which is desirable for any cash-strapped startup in this industry.

This level of scrutiny has been used to qualify both passive insertion loss results and absolute responsivity measurements, which are used to calibrate the SurePath Monitor™ product. This very accurate calibration process has helped this product reach new levels of guaranteed performance.

Chapter 5 presented a small sample of the verification experiments performed to evaluate how accurately the TE and TM spectra were extracted, as well as the overall precision of the PDf results as a function of channel number results which were found to match the designed PDf slope, as predicted from the designed compensator geometry.

6.1 Future work and scientific contributions

This Section details some of the future work, scientific contributions and other side-projects that emanated from the main project focused on extracting the TE and TM modes from the different SurePath™ portfolio products.

While Mueller matrix-based measurement and analysis techniques enabled us to extract more details in reduced measurement times for current MetroPhotonics Inc. products, the same concepts can be considered for other projects, such as the following:

Integration of Mueller matrix-based measurements for waveguide losses

Other phenomenon which exhibit clear polarization dependence can be evaluated using Mueller matrix based measurement techniques.

One such phenomenon is the Fabry-Perot cavity effect used to evaluate the propagation loss through transparent passive waveguides as a function of polarization. Two clear TE and TM modes can be seen when straight waveguides of different lengths with parallel facets are excited.

The etalon-like, fringe pattern, is dependent on the polarization-dependent absorption coefficient and can be extracted from the modulation ratio of the fringes measured. This same phenomenon is used to create Fabry-Perot cavity lasers.

Typically performed by using a lock-in amplifier to monitor the signal even with very low signal-to-noise ratio, a Mueller matrix-based simulation engine could be used to monitor the variation in fringe patterns to recover the base set of orthogonal modulation ratios showing the largest variation.

This measurement technique would be well suited for other advanced material analysis techniques as well as more complex active building block qualification measurements for different parameters, such as the polarization dependence of optical return loss, for example.

Six-state Mueller matrix measurement approach

The need for increased PDL accuracy involving the need for six-state Mueller matrix measurement and the qualification of this increase in accuracy involves rather complex hardware setups, and the purchase of PDL-calibrated devices are being investigated to allow continued monitoring of the different test stations, for PDL accuracy and testing techniques.

The increase by 50% of testing time may be counteracted by reducing the operating wavelength range for certain tests, for example, if the increase in accuracy is deemed essential.

Calibration of SurePath monitor™ logarithmic amplifiers

The SurePath monitor™ is integrated with a custom-built electronic circuit to allow sampling of the individual photocurrents generated by the built-in photodiodes and conversion to measured input powers and crosstalk corrections, by using the calibrated responsivity spectrum across the operating wavelength range of each channel.

The voltage output of the log amps and corresponding Analog to Digital (**A/D**) values sampled by the built-in Digital Signal Processor (**DSP**) can be seen as just another linear polarization dependent parameter that can be correlated to the incident SoP, and henceforth, from which Mueller matrix terms could be created and used for different analysis requirements.

Calibration of other SurePath™ portfolio products

Future SurePath™ portfolio devices may require calibration across multiple voltage biases, and different input powers, such as the SurePath Equalizer™.

The need for efficient algorithms remains omnipresent as calibration as function of voltage and input power steps adds new levels of complexity to the calibration and data acquisition processes. More complex analysis software alongside multi-channel CSA simultaneous data acquisition will be essential.

Integration of extreme most orthogonal algorithm into firmware

On-going project to evaluate if the extreme most orthogonal algorithm to extract the SoPs which yield the most different orthogonal spectrum, could be integrated as an option in different measurement tools, such as the CSA, for example.

Already, some suppliers are offering approximation of the PDλ or polarization dependent bandwidth variation obtained by varying the incident SoP to as many states as possible, often termed the "all-states" approach.

The next evolution would be to offer, alongside Mueller matrix terms, the option to simulate the spectrum of the TE and TM modes, or even consider setting the polarization controller to the appropriate waveplate angles to repeat the measurement for these two states.

Extraction of TE and TM spectra through analysis of Mueller matrix terms

While simulation of different spectra by varying the incident SoP is common knowledge. The same can be said about the recovery of the extremes of insertion loss or responsivity through the simulation of several incident SoPs.

A single article by Swann *et al.*, (44), was found in the scientific literature showing the mapping of a specific performance parameter onto the surface of a Poincaré sphere for several specific incident SoPs. This technique allowed the extraction of the PDf or PDλ using only four incident SoPs, yet did not provide the spectrum of the two orthogonal modes yielding this result. The simulation of different incident Stokes vectors and investigation of the impact on the output spectrum forms the basis of the Mueller calculus. Yet, it is believed that the isolation of the incident SoP and subsequent simulation of the full orthogonal spectra corresponding to the TE and TM incident SoPs, by solving a simple optimization problem has yet to be reported in the scientific literature, apart from this article currently under review, (15).

This elegant solution based on eigenvectors and eigenvalues involves very little computational efforts. The increase in testing capacity and capabilities within the T&M group of MetroPhotonics Inc. is undeniable and the impact for component manufacturers using different technologies should be comparable.

6.2 Conclusions

In summary, this project, which initially only aimed to increase the accuracy of extracted TE and TM centre frequency measurements to help optimize the design of the polarization compensator, has generated many different side-projects.

A deeper understanding of the Mueller matrix terms and associated Mueller calculus has allowed the T&M group to investigate both optical and opto-electrical results for different parameters. By isolating the two orthogonal modes for design related investigations, as well as increased accurate calibrations for final products for customers, the T&M group has answered the need of both its internal and external customers.

The number of requests for special analysis and investigation of different assembly sub-processes, such as die attachment stress from variation in PDf and shape factor, has helped us get involved in many of the different aspects of the design of complex opto-electrical PIC devices, from die design to final packaged assembly.

A whole new realm of opportunities has been discovered, time will tell what other scientific innovations may come from it.

Bibliography and References

[1] "Polarization-Dependent Loss measurements using modular test system configurations, Product Note 11896-2," Agilent Technologies, Santa Rosa, CA, 2000.

[2] "Agilent 8509C lightwave polarization analyzer, User's/Reference Guide," Agilent Technologies, Santa Rosa, California, United States of America, p. 342, Mar. 2001.

[3] "Polarization Measurements of Signals and Components, Product Note 8509-1," Agilent Technologies, Santa Rosa, CA, 2002.

[4] "Agilent N4150a, N415a, Photonics Foundation Library, User's and Programmer's Guide," Agilent Technologies GmbH, Herrenberger Strasse 130, 71034 Böblingen, Germany, p. 336, September 2001. [Online]. Available: http://cp.literature.agilent.com/litweb/pdf/N4150-90A63.pdf

[5] G. P. Agrawal, Fiber-Optic Communication Systems, 3rd ed. New York, NY, United States of America: John Wiley & Sons, Inc., 2002.

[6] M. Born and E. Wolf, Principles of Optics, 7th ed. Cambridge, United Kingdom: Cambridge University Press, 1999.

[7] R. M. Craig, "Visualizing the limitations of four-state measurement of PDL and results of a six-state alternative," in Technical Digest: Symposium on Optical Fiber Measurement, NIST Special Publication 988. Boulder, Colorado, United States of America: National Institute of Standards and Technology, Sept. 24–26, 2002, pp. 121–124.

[8] R. Craig, "Accurate Spectral Characterization of Polarization Dependent Loss," IEEE Journal of Lightwave Technology, vol. 21, no. 2, pp. 432–437, 2003.

[9] R. Craig, S. Gilbert, and P. Hale, "High-Resolution, Nonmechanical Approach to Polarization-Dependent Transmission Measurements," IEEE Journal of Lightwave Technology, vol. 16, no. 7, pp. 1285–1294, July 1998.

[10] (2004) The dBmOptics Inc. website. [Online]. Available: http://www.dBmOptics.com

[11] "Optical Component Spectrum Analyzer, System Operations Manual," dBmOptics Inc. Corporation, Lafayette, Colorado, United States of America, p. 210, Dec. 2003.

[12] A. Densmore, K. Pimenov, and V. I. Tolstikhin, "Integrated electroabsorption attenuator-photodetector for optical power control in WDM transmission systems," IEEE Journal of Selected Topics in Quantum Electronics, vol. 8, no. 6, pp. 1435–1444, Nov. 2002.

[13] ——, "InP-based single-mode vertically integrated waveguide photodetectors: Characterization and performance analysis," in Proceedings of Integrated Photonics Research Conference (IPR'03), June 16–18, 2003, paper IWB4, p. 4.

[14] D. Derickson, Fiber Optical Test and Measurement. Upper Saddle River, NJ, United States of America: Prentice-Hall Inc., 1998.

[15] E. Desfonds, K. Pimenov, and T. J. Hall, "Extraction of orthogonal incident state of polarization spectra using Mueller matrix approach," in Technical Digest: Symposium on Optical Fiber Measurement. Boulder, Colorado, United States of America: National Institute of Standards and Technology, Sept. 28–30, 2004, paper submitted for review.

[16] E. Desfonds, K. Pimenov, K. Nguyen, and T. Somerville, "Full C-band responsivity characterization of monolithically integrated optical channel monitors for DWDM transmission systems," in Proceedings of Photonics North 2004 (PN '04), no. 5577-14, Sept. 27–29, 2004, paper to be published.

[17] D. Favin, B. M. Nyman, and G. M. Wolter, "System and method for measuring polarization dependent loss," United States of America Patent 5,371,597, December 6, 1994.

[18] A. Gerrard and J. Burch, Introduction to Matrix Methods in Optics. New York, NY, United States of America: Dover Publications, Inc., 1975.

[19] A. Girard, et al., Guide to WDM Technology Testing, 2nd ed. Quebec City, Quebec, Canada: EXFO Electro-Optical Engineering Ing., 2000.

[20] S. Grabtchak, D. Masson, V. Tolstikhin, and B. Humphreys, "Very low loss shallow ridge waveguides for InP-based monolithically integrated WDM components," in Conference Proceedings, Photonics North Montreal 2003, Montreal, Quebec, Canada, May 25–29, 2003, p. 4.

[21] J.-J. He, et al., "Integrated polarization compensator for WDM waveguide demultiplexer," IEEE Photonics Technology Letters, vol. 1., pp. 224–226, 1999.

[22] ——, "Monolithic integrated wavelength demultiplexer based on a waveguide rowland circle grating in InGaAsP/InP," IEEE Journal of Lightwave Technology, vol. 16, pp. 631–638, 1998.

[23] J.-J. He, "Phase-dithered waveguide grating with flat passband and sharp transitions," IEEE Journal of Selected Topics in Quantum Electronics, vol. 8, no. 6, pp. 1186–1193, Nov. 2002.

[24] S. Huard, Polarisation de la lumière. Paris, France: Masson, 1993.

[25] B. Humphreys and E. S. Koteles, "Fabrication challenges for enabling metropolitan WDM network technologies," Compound Semiconductor, pp. 87–94, July 2001. [Online]. Available: http://compoundsemiconductor.net/articles/magazine/7/7/45/1

[26] B. Humphreys and A. O'Donnell, "A building block approach to manufacturing monolithic photonic integrated circuits," Compound Semiconductor, Aug. 2003. [Online]. Available: http://www.compoundsemiconductor.net/articles/magazine/9/8/5/1

[27] "SWS15104 four-state polarization controller, user's manual," JDS Uniphase Corporation, Nepean, Ontario, Canada, p. 24, May 2000.

[28] "SWS2000 Swept Wavelength System, User's Manual," JDS Uniphase Corporation, Nepean, Ontario, Canada, p. 215, May 2001.

[29] G. Keiser, Optical Fiber Communications, 3rd ed. Boston, MA, United States of America: McGraw-Hill Higher Education, 2000.

[30] E. S. Koteles, "Integrated planar waveguide demultiplexers for high-density WDM applications," in Proceedings of SPIE, ser. Critical Reviews, R. T. Chen and L. S. Lome, Eds., vol. CR71. The Internation Society for Optical Engineering, Jan. 25–26, 1999, paper CR71-01, pp. 3–32.

[31] (2004) The MetroPhotonics Inc. website. [Online]. Available: http://www.metrophotonics.com

[32] "SurePath Monitor™ data sheet," MetroPhotonics Inc., Ottawa, Ontario, Canada, p. 4, 2003. [Online]. Available: http://www.metrophotonics.com/html/prod_mon.html

[33] "SurePath Monitor™ evaluation fixture product bulletin," MetroPhotonics Inc., Ottawa, Ontario, Canada, p. 2, 2004. [Online]. Available: http://www.metrophotonics.com

[34] "SurePath Monitor™ high speed controller product bulletin," MetroPhotonics Inc., Ottawa, Ontario, Canada, p. 2, 2004. [Online]. Available: http://www.metrophotonics.com

[35] R. März, Integrated optics: design and modeling, 1st ed. Norwood, Maryland, United States of America: Artech House, Inc., 1995.

[36] (2004) National Instruments. [Online]. Available: http://www.NI.com/LabVIEW

[37] B. M. Nyman, D. L. Favin, and G. M. Wolter, "Automated system for measuring polarization-dependent loss," in Technical Digest Optical Fiber Conference (OFC 1994). San Jose, California, United States of America: Optical Society of America, 1994, paper ThK6, pp. 230–231.

[38] K. Okamoto, Fundamentals of Optical Waveguides, 1st ed. San Diego, CA, United States of America: Academic Press, 2000.

[39] J. I. Pankove, Optical processes in semiconductors. New York, NY, United States of America: Dover Publications Inc., 1971.

[40] A. L. Schawlow and C. H. Townes, "Infrared and optical masers," Physical Review, pp. 1940–1949, Dec. 15 1958. [Online]. Available: http://www.coseti.org/schawlow.htm

[41] (2004) The World of Science Website. [Online]. Available: http://scienceworld.wolfram.com/

[42] (2004) SETI@home. [Online]. Available: http://setiathome.berkeley.edu

[43] T. Somerville, "Parameter definitions, 100GHz C-band, SurePath Monitor™," Internal document, MetroPhotonics Inc., Ottawa, Ontario, Canada, p. 27, January 2003.

[44] W. Swann, S. Dyer, and R. Craig, "Four-state measurement method for polarization dependent wavelength shift," in Technical Digest: Symposium on Optical Fiber Measurement, NIST Special Publication 988. Boulder, Colorado, United States of America: National Institute of Standards and Technology, Sept. 24–26, 2002, pp. 125–128.

[45] "FOTP-157 - measurement of polarization dependent PDL of single-mode fiber optic components," Telecommunications Industry Association, July 2000. [Online]. Available: http://www.tiaonline.org/standards

[46] "FOTP-198 - measurement of polarization dependence of insertion loss of single-mode fiberoptic components by a Mueller matrix method (R2002)," Telecommunications Industry Association, December 2002. [Online]. Available: http://www.tiaonline.org/standards

[47] V. I. Tolstikhin, "Single-mode vertical integration of active devices within passive waveguides of InP-based planar WDM components," in Proceedings of Integrated Photonics Research Conference (IPR'02), July 17–19, 2002, paper IFC4, p. 3.

[48] V. I. Tolstikhin, et al., "44-channel optical power monitor based on an echelle grating demultiplexer and a waveguide photodetector array monolithically integrated on an InP substrate," in Proceedings of Optical Fiber Communication Conference (OFC'03), Mar. 2000, paper PD-37, p. 3.

[49] V. Tolstikhin, et al., "InP-based monolithic integration of echelle grating (de)multiplexer, passive waveguide circuitry and active waveguide devices for applications in DWDM transmission systems," in Proceedings of 29th European Conference on Optical Communications, vol. 3, Sept. 21–25, 2003, pp. 666–667.

[50] V. Tolstikhin, A. Densmore, K. Pimenov, and S. Laframboise, "Monolithically integrated optical channel monitor for DWDM transmission systems," IEEE Photonics Technology Letters, vol. 15, pp. 843–845, June 2003.

[51] V. Tolstikhin, et al., "Monolithically integrated optical channel monitor for DWDM transmission systems," IEEE Journal of Lightwave Technology, vol. 22, pp. 146–153, Jan. 2004.

[52] J. Yeager and M. A. Hrusch-Tupta, Eds., Low Level Measurements Handbook, 5th ed. Cleveland, Ohio, United States of America: Keithley Instruments Inc., 1998. [Online]. Available: https://www.keithley.com/servlet/Data?id=9538

Appendix A

List of acronyms

A/D Analog to digital

AR Anti-reflection

ASE Amplified spontaneous emission

AWG Arrayed waveguide (demultiplexer)

BBS Broadband source

CSA Component Spectrum Analyzer

CWDM Coarse wavelength division multiplexing

dB decibel

DeMux Demultiplexer

DUT Device-under-test

DWDM Dense wavelength division multiplexing

EDFA Erbium-doped fiber amplifier

fc centre frequency

FTTH Fiber-to-the-home

FTTP Fiber-to-the-premises

fs femtosecond

GΩ gigaohms

GUI Graphical user-interface

IC Integrated circuit

IL Insertion loss

InP Indium phosphide

ITU International Telecommunication Union

L+45 Linear +45 degrees polarization

L-45 Linear -45 degrees polarization

LCP Left-hand circular polarization

LHP Linear horizontal polarization

LP Linear polarized

LVP Linear vertical polarization

MMF Multi-mode fiber

MUX Multiplexer

nA nanoampere

NIST National Institute of Standards and Technology

nm **nanometer**

NRC National Research Council (Canada)

O-E-O Optical to Electical to Optical

OEM Original equipment manufacturer

OSA Optical spectrum analyzer

pa picoamperes

PC Personal Computer

PCB Printed circuit board

PDf Polarization dependent frequency

PDλ Polarization dependent lambda (wavelength)

PDL Polarization dependent loss

PDR Polarization-dependent responsivity

PIC Photonic integrated circuit

PLC Planar lightwave circuit

pm picometer

PM Polarization maintaining

ps picosecond

3R Repeat-Regenerate-Retime

RCA Root-cause analysis

RCP Right-hand circular polarization

R&D Research and development

SEM Scanning electron microscope

SMF Single-mode fiber

SOM Source optics module

SONET Synchronous optical network

SoP State of polarization

SPC Statistical process control

SWS Swept-wavelength system

T&M Test and measurement

TDM Time division multiplexing

TE Transverse electrical

TEM Transverse electromagnetic

TIA Transimpedance amplifier

TLS Tunable laser source/system

TM Transverse magnetic

VI Virtual instrument

WDM Wavelength division multiplexing

Appendix B

Definitions of optical and opto-electrical parameters

This section presents the definitions for the most common parameters used in the evaluation of the optical insertion loss and absolute responsivity spectrum obtained through the use of the SoP-simulation engine. All of the algorithms were implemented using LabVIEW and integrated into the analysis client and data acquisition software.

The preferred definitions used within MetroPhotonics Inc. were summarized internally in (43). This original document was inspired by many reference documents, such as (4), (11), (19, Chapter 3), and (28, pages 108-115).

The ^{L} or ^{R} superscripts are used to differentiate parameters with the same name but used for insertion loss spectra or responsivity spectra.

The ^{,XdB} superscript indicates that the associated parameter was determined using a passband of XdB or is dependent on the centre frequency defined by using the XdB passband.

The $_{SoP_i}$ subscript indicates that the associated parameter is specific to either the SoP_1 or SoP_2 extreme orthogonal SoP.

B.1 Optical parameters

▷ **Clear passband** (PB_{clear})

This is the frequency range over which a channel's optical parameters are defined. The range is dependent on the channel separation. It is centered on the centre frequency of a channel specific to each extreme SoP for untuned tests, and is centered on the channels ITU frequency for temperature tuned tests.

▷ **Minimum insertion loss** ($IL_{SoP_i}^{MIN}$)

The minimum insertion loss across the operating wavelength range.

▷ **Minimum insertion loss frequency** ($f\left(IL_{SoP_i}^{MIN}\right)$)

The frequency of the minimum insertion loss across the operating wavelength range.

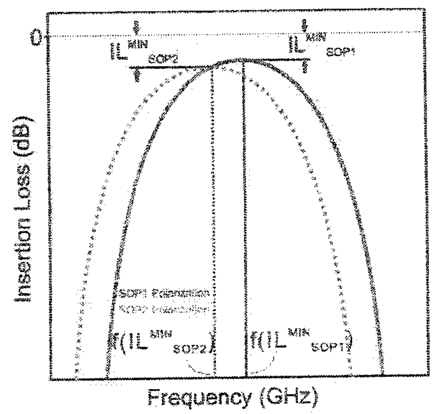

▷ **XdB passband** $\left(\delta f_{SoP_i}^{L,XdB}\right)$

The effective bandwidth measured XdB down from the minimum insertion loss, specific to each extreme SoP. Typical values of X used are 0.5, 1, 3, 6, 10 and 20dB.

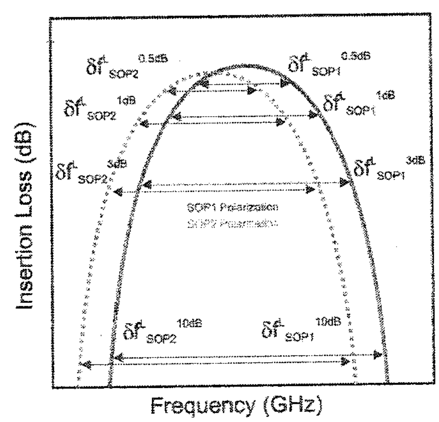

▷ **Centre frequency** $\left(f_{c_{SoP_i}}^{L,XdB}\right)$

The centre of the XdB passband points, specific to each extreme SoP. Typical value of X is 3dB.

$$f_{c_{SoP_i}}^{L,XdB} = \frac{\left(f_{Xa_{SoP_i}} + f_{Xb_{SoP_i}}\right)}{2}$$

▷ **Insertion loss at centre frequency** $\left(IL\left(f_{c_{SoP_i}}^{L,XdB}\right)\right)$

The insertion loss at the centre of the XdB passband points, specific to each extreme SoP. Typical value of X is 3dB.

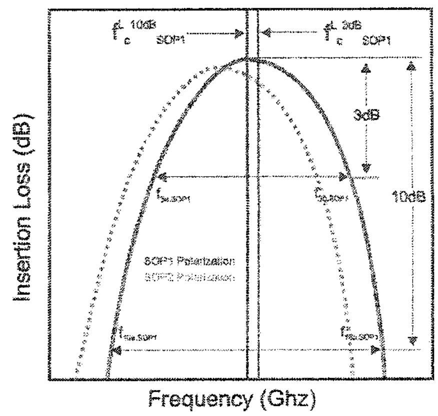

▷ **Maximum insertion loss** $\left(IL_{SoP_i}^{MAX,XdB}\right)$

The maximum insertion loss in the clear passband, centered around the centre frequency.

▷ **Maximum insertion loss frequency** $\left(f\left(IL_{SoP_i}^{MAX,XdB}\right)\right)$

The frequency of the maximum insertion loss in the clear passband, centered around the centre frequency.

▷ **In-band ripple** $\left(Ripple_{SoP_i}^{L,XdB}\right)$

The difference between $IL_{SoP_i}^{MAX,xdB}$ and $IL_{SoP_i}^{MIN}$, measured within the clear passband of a given channel.

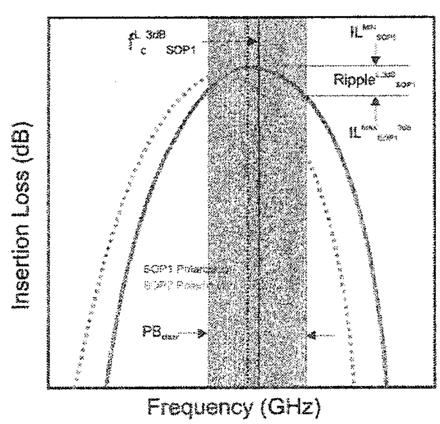

▷ **Adjacent channel crosstalk** $\left(AX_{SoP_i}^{L,XdB}\right)$

The difference between the maximum optical insertion loss of a channel, $IL_{SoP_i}^{MAX,xdB}$, and the minimum level of optical leakage power suppression (maximum transmission) in the clear passband of adjacent channels. This parameter is the worst of the crosstalks calculated using the m, $m+1$ passbands, and the m, $m-1$ passbands.

Adjacent clear passbands are assumed to be spaced at exactly the nominal channel separation (e.g. 100GHz).

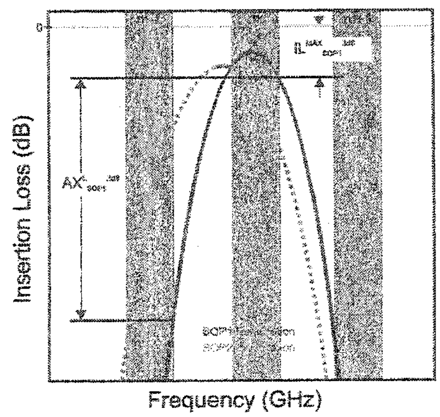

▷ **Polarization dependent frequency** $\left(PDf_{SoP_i}^{L,XdB}\right)$

This is a measure of the change in centre frequency as a function of polarization, measured as the difference in centre frequencies of the two extreme polarization states.

It is specified for devices as an absolute term, but could also be defined as the difference between TE and TM, in non-absolute terms, if extreme states of polarization can be assigned to TE and TM, instead of SoP_1 and SoP_2.

$$PDf^{L,XdB} = \left| f_{c_{SoP_1}}^{L,XdB} - f_{c_{SoP_2}}^{L,XdB} \right|$$

$$PDf^{L,XdB} = f_{c_{TE}}^{L,XdB} - f_{c_{TM}}^{L,XdB}$$

▷ **Polarization dependent loss** $\left(PDL^{XdB}\right)$

This is a measure of the insertion loss change as a function of polarization. This is measured as the difference in insertion loss of the two extreme polarization states at their centre frequencies.

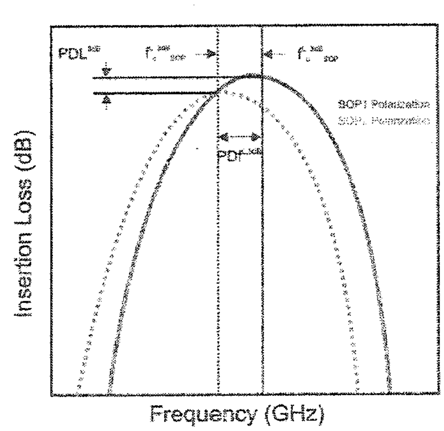

▷ **Orthogonality using PDf** $\left(O_f^{L,XdB}\right)$

This is defined as the dot product of the Stokes vectors of the extreme SoP used to determine the PDf value for each channel. The optimal value for this parameter is -1, and any deviation from -1 indicates a less-than-optimal orthogonality for the two extreme polarization states, SoP_1 and SoP_2, defined by this criterion.

▷ **Orthogonality using PDL** $\left(O_L^{L,xdB}\right)$

This is defined as the dot product of the Stokes vectors of the extreme SoP used to determine the PDL value for each channel. The optimal value for this parameter is -1, and any deviation from -1 indicates a less-than-optimal orthogonality for the two extreme polarization states, SoP_1 and SoP_2, defined by this criterion.

▷ **Shape factor** (SF)

Ratio of 20dB Passband and 3dB Passband, used to evaluate any distortion (widening or reduction) of spectra in main filter lobe due to die attachment or any other external stress influence.

$$SF = \frac{\delta f_{SoP_i}^{L,20dB}}{\delta f_{SoP_i}^{L,3dB}}$$

B.2 Opto-electrical parameters

The following parameters are obtained by characterizing the internal p-i-n diodes of products of the SurePath™ portfolio under excitation by light. Some subtle differences do exist when compared to optical only parameters, namely the largest value is termed maximal responsivity, whilst this may be compared to the minimal insertion loss.

All parameters are measured under operating bias voltage conditions.

▷ **Clear passband** (PB_{clear})

This is the frequency range over which a channel's opto-electrical parameters are defined. The range is dependent on the channel separation. It is centered on the centre frequency of a channel specific to each extreme SoP for untuned tests, and is centered on the channels ITU frequency for temperature tuned tests.

▷ **Maximum responsivity** $\left(R_{SoP_i}^{R,MAX}\right)$

The maximum responsivity across the operating wavelength range.

▷ **Maximum responsivity frequency** $\left(f\left(R_{SoP_i}^{R,MAX}\right)\right)$

The frequency of the maximum responsivity across the operating wavelength range.

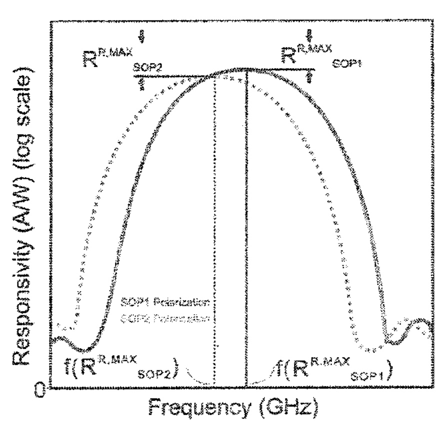

▷ **XdB passband** $\left(\delta f^{R,XdB}_{SoP_i}\right)$

The effective bandwidth measured XdB down from the maximum responsivity, specific to each extreme SoP. Typical values of X used are 0.5, 1, 3, 6, 10 and 20dB.

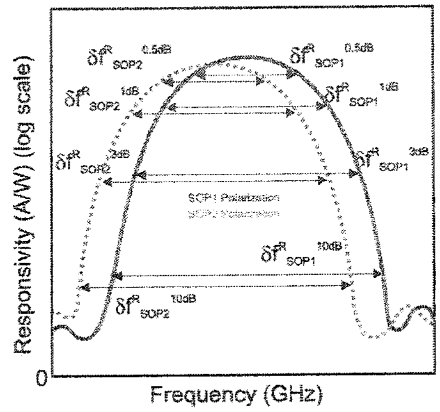

▷ **Centre frequency** $\left(f^{R,XdB}_{cSoP_i}\right)$

The centre of the XdB passband points, calculated as follows:

$$f^{R,XdB}_{cSoP_i} = \frac{\left(f_{Xa_{SoP_i}} + f_{Xb_{SoP_i}}\right)}{2}$$

Typical value of X is 3dB.

▷ **Responsivity at centre frequency** $\left(R\left(f^{R,XdB}_{cSoP_i}\right)\right)$

The responsivity at the centre of the XdB passband points, typical value of X is 3dB.

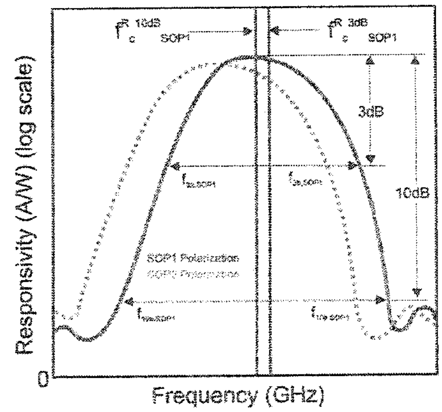

▷ **Minimum responsivity** $\left(R^{R,MIN,XdB}_{SoP_i}\right)$

The minimum responsivity in the clear passband, centered around the centre frequency.

▷ **Minimum responsivity frequency** $\left(f\left(R^{R,MIN,XdB}_{SoP_i}\right)\right)$

The frequency of the minimum responsivity in the clear passband, centered around the centre frequency.

▷ **In-band ripple** $\left(Ripple^{R,XdB}_{SoP_i}\right)$

The difference between $R^{R,MAX}_{SoP_i}$ and $R^{R,MIN,xdB}_{SoP_i}$, measured within the clear passband of a given channel.

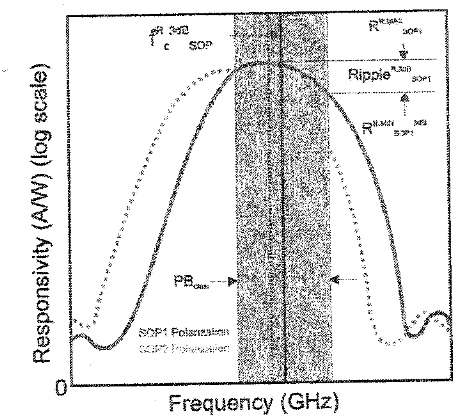

▷ **Adjacent channel crosstalk** $\left(AX^{R,XdB}_{SoP_i}\right)$

The difference between the minimum responsivity of a channel, $R^{R,MIN,XdB}_{SoP_i}$, and the minimum level of optical leakage power suppression (maximum responsivity) in the clear passband of adjacent channels. This parameter is the worst of the crosstalks calculated using the m, $m+1$ passbands, and the m, $m-1$ passbands.

Adjacent clear passbands are assumed to be spaced at exactly the nominal channel separation (e.g. 100GHz).

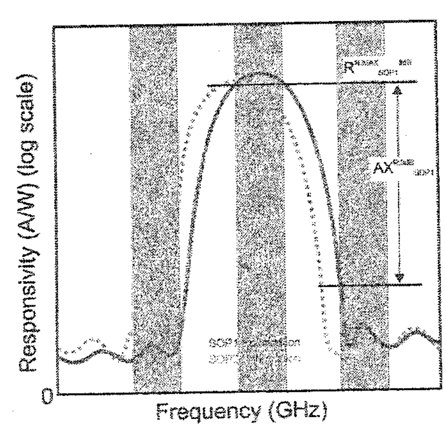

▷ **Non-adjacent channel crosstalk** $\left(NAX^{R,XdB}_{SoP_i}\right)$

The difference between the minimum responsivity of a channel, $R^{R,MIN,XdB}_{SoP_i}$, and the minimum level of optical leakage power suppression (maximum responsivity) in the clear passband of all non-adjacent channels.

Non-adjacent clear passbands are assumed to be spaced at exactly the nominal channel separation (e.g. 100GHz).

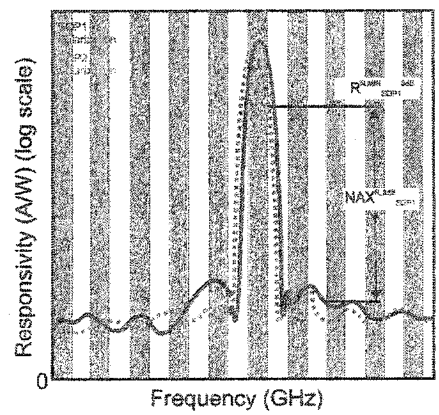

▷ **Polarization dependent frequency** $(PDf^{R,XdB})$

Measure of the change in centre frequency as a function of polarization, measured as the difference in centre frequencies of the two extreme polarization states based on responsivity.

It is specified for devices as an absolute term, but could also be defined as the difference between TE and TM, in non-absolute terms, if extreme states of polarization can be assigned to TE and TM instead of SoP_1 and SoP_2.

$$PDf^{R,XdB} = \left| f_{C_{SoP_1}}^{R,XdB} - f_{C_{SoP_2}}^{R,XdB} \right|$$

$$PDf^{R,XdB} = f_{C_{TE}}^{R,XdB} - f_{C_{TM}}^{R,XdB}$$

▷ **Polarization dependent responsivity** (PDR^{XdB})

This is a measure of the change in responsivity at centre frequency as a function of polarization, corresponds to the difference in centre frequency responsivity of the two extreme polarization states, SoP_1 and SoP_2.

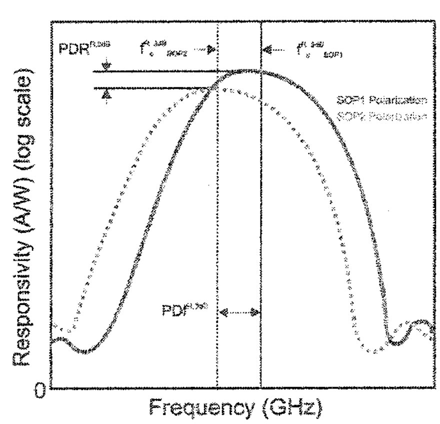

▷ **Orthogonality using PDR** $(O^{R,XdB})$

This is defined as the dot product of the Stokes vectors which yield the extreme PDR value for each channel. The optimal value for this parameter is -1, and any deviation from -1 indicates a less-than-optimal orthogonality for the two extreme polarization states, SoP_1 and SoP_2, defined by this criterion.

Appendix C

Mathematical Expansions

This section presents detailed expansions of some of the equations found in the body of this document.

C.1 $\frac{\lambda_0}{4}$-plate and $\frac{\lambda_0}{2}$-plate Mueller matrix expansion

It was shown in Section 4.2 how the combination of the Mueller matrices of a quarter-waveplate and half-waveplate with their fast axis set at α and β angles along their fast axis enables the sampling of the Poincaré sphere, as seen in the following figure.

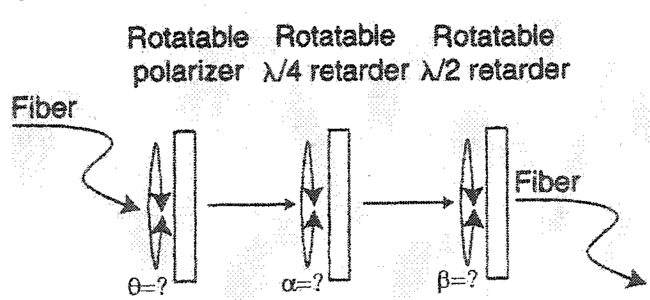

The mathematical expansion is shown below. More details can be found in (18, Section IV.3). As with normal matrix multiplications, Mueller matrices are not commutative but are associative, so multiple Mueller matrices may be combined into a single system matrix.

$$\begin{bmatrix} S_0 \\ S_1 \\ S_2 \\ S_3 \end{bmatrix} = M_{\frac{\lambda_0}{2}}(\beta)\, M_{\frac{\lambda_0}{4}}(\alpha) \begin{bmatrix} 1 \\ 1 \\ 0 \\ 0 \end{bmatrix} \tag{C.1}$$

where:

▷ the expansion of the half-waveplate is:

$$M_{\frac{\lambda_0}{2}}(\beta) = \begin{bmatrix} 1 & 0 & 0 & 0 \\ 0 & \cos(4\beta) & \sin(4\beta) & 0 \\ 0 & \sin(4\beta) & -\cos(4\beta) & 0 \\ 0 & 0 & 0 & -1 \end{bmatrix}$$

▷ the expansion of the quarter-waveplate is:

$$M_{\frac{\lambda_0}{4}}(\alpha) = \begin{bmatrix} 1 & 0 & 0 & 0 \\ 0 & \cos^2(2\alpha) & \cos(2\alpha)\sin(2\alpha) & -\sin(2\alpha) \\ 0 & \cos(2\alpha)\sin(2\alpha) & \sin^2(2\alpha) & \cos(2\alpha) \\ 0 & \sin(2\alpha) & -\cos^2(2\alpha) & 0 \end{bmatrix}$$

▷ the Stokes vector of linearly horizontal polarized light, $\begin{bmatrix} 1 \\ 1 \\ 0 \\ 0 \end{bmatrix}$

Let $\xi = M_{\frac{\lambda_0}{4}}(\alpha) \begin{bmatrix} 1 \\ 1 \\ 0 \\ 0 \end{bmatrix}$, thus

$$\xi = \begin{bmatrix} 1 & 0 & 0 & 0 \\ 0 & \cos^2(2\alpha) & \cos(2\alpha)\sin(2\alpha) & -\sin(2\alpha) \\ 0 & \cos(2\alpha)\sin(2\alpha) & \sin^2(2\alpha) & \cos(2\alpha) \\ 0 & \sin(2\alpha) & -\cos^2(2\alpha) & 0 \end{bmatrix} \begin{bmatrix} 1 \\ 1 \\ 0 \\ 0 \end{bmatrix}$$

$$\xi = \begin{bmatrix} 1 \\ \cos^2(2\alpha) \\ \cos(2\alpha)\sin(2\alpha) \\ \sin(2\alpha) \end{bmatrix} \tag{C.2}$$

Merging Equations C.1 and C.2, yields:

$$\begin{bmatrix} S_0 \\ S_1 \\ S_2 \\ S_3 \end{bmatrix} = M_{\frac{\lambda_0}{2}}(\beta)\,\xi = \begin{bmatrix} 1 & 0 & 0 & 0 \\ 0 & \cos(4\beta) & \sin(4\beta) & 0 \\ 0 & \sin(4\beta) & -\cos(4\beta) & 0 \\ 0 & 0 & 0 & -1 \end{bmatrix} \begin{bmatrix} 1 \\ \cos^2(2\alpha) \\ \cos(2\alpha)\sin(2\alpha) \\ \sin(2\alpha) \end{bmatrix}$$

which in turn, simplifies to the following expansion

$$\begin{bmatrix} S_0 \\ S_1 \\ S_2 \\ S_3 \end{bmatrix} = \begin{bmatrix} 1 \\ \cos^2(2\alpha)\cos(4\beta) + \cos(2\alpha)\sin(2\alpha)\sin(4\beta) \\ \cos^2(2\alpha)\sin(4\beta) - \cos(2\alpha)\sin(2\alpha)\cos(4\beta) \\ -\sin(2\alpha) \end{bmatrix}$$

C.2 Theoretical error of extracted parameters

This section details how to compute the theoretical error of extracted parameters, focusing on the theoretical error of centre frequency and resulting error on PDf or PDλ.

PDλ is the difference between two centre wavelengths, λ_{CENTER_A} and λ_{CENTER_B}.

These are determined by finding the peak insertion loss, subtracting XdB to its value, and then looking for two wavelengths that have this new insertion loss value on each side of the main filter lobe, λ_{XdB_A} and λ_{XdB_B}. The average value of these two wavelengths is the centre wavelength. The following figures show these steps, with X=3dB.

The values of λ_{3dB_A} and λ_{3dB_B} are linearly interpolated between the two closest measured data points, as seen in the following figure termed from this point on λ_i and λ_{i+1}, i being the index in the wavelength array.

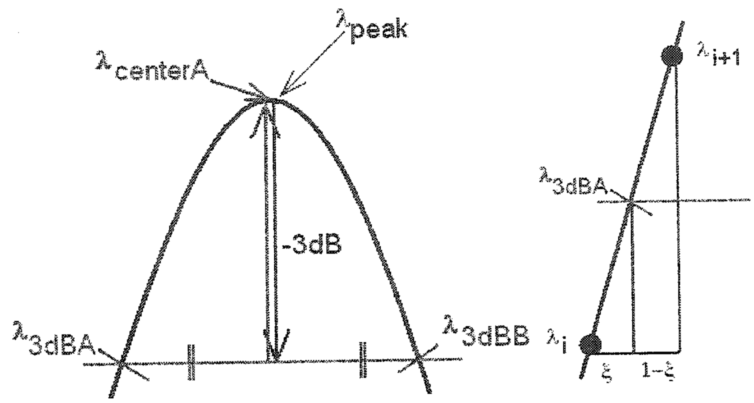

The equation used to linearly interpolate the value of λ_{3dB_A} or λ_{3dB_B} follows:

$$\lambda_{3dB_A} = \lambda_i + \xi\left(\lambda_{i+1} - \lambda_i\right) = (1-\xi)\,\lambda_i + \xi\lambda_{i+1}$$

The error on λ_{3dB_A} is $\Delta\lambda_{3dB_A} = \sqrt{(1-\xi)^2\,\Delta\lambda_i^2 + \xi^2\Delta\lambda_{i+1}^2}$, obtained by using the general squared error of the derivative of the function. Worst-case error will occur when ξ is equal to $\frac{1}{2}$, hence exactly between the λ_i and λ_{i+1} data points. This can be proven by equating the first derivative of this equation to zero and solving for ξ.

Hence the worst-case error on λ_{3dB_A} and λ_{3dB_B}, assuming every data point has the same average error of half the data point spacing is defined as follows:

$$\Delta\lambda_{3dB_A} = \sqrt{\left(1-\frac{1}{2}\right)^2\Delta\lambda^2 + \left(\frac{1}{2}\right)^2\Delta\lambda^2} = \sqrt{\frac{\Delta\lambda^2}{2}} = \Delta\lambda$$

When subtracting λ_{3dB_A} and λ_{3dB_B} to obtain λ_{CENTER_A}, the overall error will be the square root of the sum of the squares of the errors on the interpolation of λ_{3dB_A} and λ_{3dB_B}, which turns out to be equal to the error $\Delta\lambda$, which is equal to half the wavelength spacing.

Once more, when subtracting λ_{CENTER_A} and λ_{CENTER_B}, the overall error will be the square root of the sum of the squares of the errors on the calculation of λ_{CENTER_A} and λ_{CENTER_B}, which turns out to be equal to the square-root of 2 multiplied by the wavelength accuracy, or half the wavelength step, yielding $\sqrt{2}\Delta\lambda$.

For different values of wavelength spacing, we obtain different error values, as presented in the following table, which shows typical default wavelength steps used by different sweeping-mode TLS-based systems. The commonly used rule of thumb approximation, $0.8nm \simeq 100GHz$, used to convert wavelengths to frequency around 1550nm was used to convert the PDλ in $\pm$pm error to a PDf error in $\pm$GHz.

Wavelength step [pm]	Wavelength error [pm]	PDλ error [pm]	PDf error [$\approx$GHz]
3	$\pm$1.5	$\pm$2.121	$\pm$0.265
5	$\pm$2.5	$\pm$3.53	$\pm$0.441
10	$\pm$5	$\pm$7.071	$\pm$0.885

Appendix D

LabVIEW code implementations

This section presents some of the LabVIEW[1] code used throughout this project, which are called Virtual Instruments (**VIs**). LabVIEW being a graphically based programming language, it is somewhat awkward to detail the programming steps, except maybe in a **pseudo-code** approach.

A screenshot of the LabVIEW code layout, the **Block Diagram**, and graphical user-interface (**GUI**), or **Front Panel** is presented, and a more detailed pseudo-code algorithm, detailing the different steps is also shown.

The following programs are shown in this section:

- ▷ Analysis client program
- ▷ Centre frequency and insertion loss program
- ▷ Normalized difference program, and its main subroutine:
  - ⇒ Compute normalized difference for T_0 and T_0' for given (α, β)
- ▷ Numerical solution program (for given Mueller matrix array)

Many other VIs to control the data acquisition hardware and perform other data analysis for various tests were written. The programs shown herein were chosen to show the typical programming philosophy used throughout this project.

D.1 Analysis client program

The analysis client software became and still is T&M group's analysis workhorse ever since its original incarnation (version 1.0) in January of 2002, up to version 4.86 released on July 12^{th}, 2004.

Originally aimed to parse files for each channel from multi-channel data files as large as 10Megs. As the SoP-simulation engine became a workhorse of its own, the simulation quickly became too intensive for the PCs used to control the hardware acquiring the data. Other channels and DUTs could be tested instead of waiting for the analysis to be completed.

Design philosophy and interface

---

[1] For more information on LabVIEW, please visit (36).

Largely inspired by other distributed computing projects, such as SETI@Home[2] , the analysis client was designed to run in the background on the PC workstations of the T&M team members. Allowing the lower-class PCs used in the labs to be completely focused on data acquisition.

The Front Panel consists of a small window requiring minimal user-interaction. This approach is similar to the SETI@Home client which can be enabled only when the computer's screen saver is enabled or when the CPU usage is below a certain threshold.

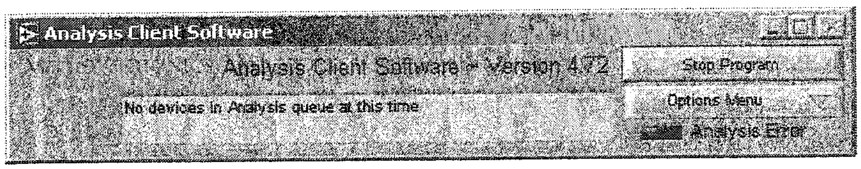

Larger Poincaré sphere sampling densities could be used without affecting the testing capacity of the different test stations manned by the T&M operators and engineers. While a DUT was officially done testing once the data was analyzed, this asynchronous analysis process is sufficient for large production levels and is being tied into SPC systems.

The most orthogonal numerical approach has made the analysis efficient enough to yield results within seconds, but to maintain timely data acquisition rates, the data acquisition and analysis have been kept separate nonetheless.

Data flow structure

The asynchronicity of the acquisition and analysis must be tackled to ensure all acquired data does get analyzed. While advanced database driven queue systems, such as SQL or Microsoft's Access, could have been used, a simple text-file approach to control this process flow does suffice, even with three different types of data is being handled by a single client:

- ▷ Passive die screening data (JDS Uniphase SWS)
- ▷ Relative photocurrent conversion to absolute responsivity (JDS Uniphase SWS)
- ▷ Responsivity data (dBm Optics Inc. CSA)

Some feedback is given to the operator, with minimal delay, to confirm the obtained results are valid, the largest part of the analysis burden is handled by the client.

Once a channel's spectrum is acquired, and the raw data files are saved to the network drive (and hence available to all connected computers throughout the corporate network), an analysis queue ***_todo.txt file** is updated by adding a new line to it, indicating where the last channel's raw data has been saved. Different text files are used for the three different types of data, as follows:

- ▷ (...)\Queue\AnalysisQueue_todo.txt
- ▷ (...)\Queue\AnalysisQueue_Responsivity_todo.txt
- ▷ (...)\Queue\AnalysisQueue_CSAResponsivity_todo.txt

[2] For more information on SETI@Home, please visit (42).

Each of these files is checked at a regular time interval to see if new data is ready to be analyzed, and if so, the appropriate analysis sub-routine is initiated to obtain the desired analysis results. If any error occurs, an additional text file is updated with a suffix ***_error.txt** instead of ***_todo.txt**, so that the error can be investigated and resolved as early as possible. An e-mail is also sent to the software maintainer when such events do occur, and a visible LED starts flashing on the Front Panel of all running copies of the client.

Once analyzed, individual raw data file paths are saved to different files to indicate what has been analyzed and when. This has proven useful to monitor workstation throughput and debug which channels in a multi-channel DUT had been analyzed before and/or after an error occurred.

- ▷ (...)\Queue\Analyzed\AnalysisQueue_done_MONTH.txt
- ▷ (...)\Queue\Analyzed\AnalysisQueue_Responsivity_done_MONTH.txt
- ▷ (...)\Queue\Analyzed\AnalysisQueue_CSAResponsivity_done_MONTH.txt

Other features added to the analysis client included the capability to monitor the content of the queue (***_todo.txt** file content) and to add to the queue by selecting individual files or by selecting entire folders for reanalysis.

This was especially useful when new criterion were being deployed after initial qualification or special analysis requests for large data sets, since large batch files containing hundreds of raw file paths could be added and analyzed overnight for review the following day.

Performance and algorithm details

While large channel data structures are loaded in parallel when multiple channels are compared to each other or during temperature tuning of the whole device (up to 20,000 wavelength points for each channel), several Megs of RAM are reserved for this process. The CPU cycles monitor utility still remains relatively flat, allowing normal daily use of the PC for other applications with little interference. The impact is minimal as originally desired.

Tuning of the analysis client settings to ensure the most efficient analysis process as well as continued qualification of the accuracy of the extracted Stokes vectors used to simulate the SoP_i corresponding spectra. The different settings used for the extreme centre frequency, insertion loss and normalized difference criteria were chosen after testing of the analysis client on different PCs, to avoid taking over too much resources on slower machines.

The Block Diagram of the analysis client is shown on a single page in landscape format, at the end of this chapter. Although more suited for electronic viewing, this code shows the flow for the Responsivity CSA data analysis. The algorithm in pseudo-code can be viewed in Algorithm 2 on the next page, only the details of the analysis of the CSA Responsivity results are shown, the passive insertion loss and relative SWS photocurrent are not detailed.

D.2 Centre frequency and insertion loss program

Details about the Extreme centre frequency and insertion loss criterion implementation in LabVIEW are contained herein. These two criterion were described separately in Sections

Algorithm 2 Analysis client algorithm

```
Check for new version of analysis client and

   ▷ if newer version available, stop client and install

Set default settings (set index=0)
Background processes/operator interaction

   ▷ Monitor newer version release at every 10minutes and install if found

   ▷ Monitor status bar update and options menu value change to add items or view queue
     content

Start loop, until Quit program button pressed
if (modulus(index/3))==0

     check if new passive die raw data available for analysis
     if so, run passive die analysis subroutine on data

          (details not laid out)

     else, do nothing
     index=index+1

if (modulus(index/3))==1

     check if new relative photocurrent SWS raw data available for analysis
     if so, run relative photocurrent SWS analysis subroutine on data

          (details not laid out)

     else, do nothing
     index=index+1

if (modulus(index/3))==2

     check if new responsivity CSA raw data available for analysis
     if so, run responsivity CSA analysis subroutine on data
          if (*.tmp) file
             ▷ create Mueller matrix terms from 4 or 6 SoP measured
             ▷ save to (*.raw) Mueller matrix terms file
             ▷ create responsivity extreme file (*.resp) from (*.tmp) file
          else, do nothing
          read (*.raw) file and run Numerical solution sub-routine
             ▷ check that obtained Stokes vector has same orientation as
               previous channel (except if first channel)
             ▷ simulate SoP_1 and SoP_2 spectrum, analyze spectrum and save to
               (*.dat) file
          Save summary (Analysis_*.txt) file containing:
             ▷ all channel summary of all parameters analyzed
             ▷ all channel ITU-tuning temperature and passband error
               optimization
             ▷ report damaged channels (shorts, opens and missing channels)
             ▷ extracted all dark current information and save to (Dark_*.txt)
               file
          Save (*.raw) file path to appropriate (Analy-
          sis_*_done_MONTH.txt) file
     else, do nothing

index=index+1
```

4.3.2 and 4.3.3 and then combined in Section 4.3.4 on page 57. The main program used is called the **Main PDLambda Analysis (tracking IL and fc).VI**.

For performance related issues, the insertion loss and centre frequency were extracted using both the 3dB and 10dB levels to avoid any ripple artifact from noise in our electrical photocurrent spectrum acquisition setup. This software combines both criteria, hence individual VIs showing the single criterion are not included to avoid any duplication.

This sub-VI was called from the analysis client for passive optical die screening. Given an input Mueller matrix array, this software would find an initial guess of centre frequency using a valid random (α, β) angle pair, and then initialize clusters with all the different variables required to track the following four variables, and the corresponding (α, β) angle pair which generate these results:

- ▷ 3dB level insertion loss extremes and corresponding (α, β) angle pair
- ▷ 3dB level centre frequency extremes and corresponding (α, β) angle pair
- ▷ 10dB level insertion loss extremes and corresponding (α, β) angle pair
- ▷ 10dB level centre frequency extremes and corresponding (α, β) angle pair

The Poincaré sphere sampling density is selected by setting the variable **step size**. Two nested for-loops are then used to vary the α and β angles to cover the Poincaré sphere one incident SoP at a time. For each step, the above mentioned parameters are evaluated and compared to the last stored extreme values in the 3 and 10dB data clusters. If new extremes are found, the cluster data is updated accordingly.

When all sampling steps are completed, the orthogonality factors for insertion loss and centre frequency are computed for each of the four variables and stored in a separate cluster. A timer is used to monitor the time taken for each channel to help any optimization efforts, as this sampling approach remains computationally intensive.

The code of the Main PDLambda Analysis (tracking IL and fc) VI is shown at the end of the chapter, the Front Panel and the Block Diagram each on a different page in landscape format. Although more suited for electronic viewing, this code shows the flow of a given input Mueller matrix data set to the final insertion loss and centre frequency extremes and corresponding (α, β) angle pair, defined at the 3 and 10dB level. The algorithm in pseudo-code can be viewed in Algorithm 3 on the next page.

D.3 Normalized difference program

Details about the normalized difference program are contained herein. The main program used for this criterion was called **Main Optical Analysis (most orthogonal).VI**. This subroutine, also called from the analysis client, uses Mueller matrix terms to extract the normalized difference term, as described in Section 4.4.1 on page 60.

The main subroutine of this VI is called **Compute T0 array (most orthogonal).VI** and is described in the Section D.3.1.

After setting the normalized difference indicator value to 1 (which indicates the equal orthogonal spectrum compared), this software reads the raw data file and parses the wavelength

Algorithm 3 Extreme centre frequency and insertion loss algorithm

```
Set timer to 0
Set all clusters to defaults values
Set step to specified step size (sampling density)
Read (*.raw) data file and parse λ or frequency array and Mueller matrix

      Create array subset using specified frequency range

Using random (α, β) angle pair, simulate full spectrum range

      Repeat until valid minimum insertion loss frequency found
      if more than 25 angle pairs attempted, stop program and return error

Use newfound fc, and corresponding (α, β) angle pair to populate clusters
Crop frequency array and Mueller matrix to cover specified range around newfound fc (±GHz)
for index_α = 0 : 1 : step

      set α = π*index_α / step
      for index_β = 0 : 1 : step/4

            set β = index_β*2π / step
            compute T_0 array
            extract all parameters listed below:
               ▷ 3dB level insertion loss and centre frequency
               ▷ 10dB level insertion loss and centre frequency

            if new parameters are smaller/larger than previous extreme values
            replace in cluster and update corresponding (α, β) angle pair

      end

end
Compute orthogonality factors for each parameter

Compute time taken to perform analysis using timer
```

and Mueller matrix arrays. In a fashion similar to the previous program a random (α, β) angle pair is used to find an initial guess of centre frequency for the subsequent array cropping to the desired range around this centre frequency approximation.

The Poincaré sphere sampling density is controlled through the setting of the variable **step size**. Two nested for-loops are used to vary the α and β angles to cover only half of the Poincaré sphere, since opposite Stokes vectors are compared to guarantee orthogonality of the resulting SoP_1 and SoP_2 incident Stokes vectors.

For each step, the normalized parameter is computed, and if a smaller value than the stored value is found, the stored (α, β) angle pair is replaced by the last (α, β) angle pair used.

A timer is used to monitor the time taken for each channel to help any optimization efforts since, even though only half the Poincaré sphere is sampled, this approach remains computationally intensive.

The code of the Main Optical Analysis (most orthogonal) VI is shown at the end of this chapter, the Front Panel and Block Diagram on a single page in landscape format. Although more suited for electronic viewing, this code shows the flow of a given input Mueller matrix data set to the final SoP_1 Stokes vector solution. The algorithm in pseudo-code can be viewed in Algorithm 4.

Algorithm 4 Normalized difference extreme evaluation algorithm

```
Set timer to 0
Set cluster to defaults values
Set Normalized difference indicator to 1
Set step to specified step size or sampling density
Read (*.raw) data file and parse frequency array and Mueller matrix

    Create array subset using specified frequency range

Using random (α, β) angle pair, simulate full spectrum range

    Repeat until valid minimum insertion loss frequency is found
    if more than 25 angle pairs attempted, stop program and return error

Crop frequency array and Mueller matrix to cover specified range around newfound fc
for index_α = 0 : 1 : step/2 % this will cover the bottom half of Poincaré sphere

    set α = π*index_α / step
    for index_β = 0 : 1 : step/4

        set β = index_β*2π / step
        call Compute T_0 array (most orthogonal).VI to:
           ▷ Compute T_0 (λ) and T'_0 (λ) spectrum
           ▷ Compute normalized difference for given (α, β)
        if new normalized difference is smaller than store smallest value
        then replace with new value and update cluster with (α, β) angle pair
        and Stokes vectors

    end

end

Compute time taken to perform analysis using timer
```

D.3.1 Computation of normalized difference of T_0 and T_0' for given (α, β)

This subroutine called by the Main Optical Analysis (most orthogonal).VI, is called **Compute T0 array (most orthogonal).VI**. It shows how the code is laid out to handle Stokes vector and implement one criterion, namely the normalized difference criterion described in Section 4.4.1 on page 60.

Given an (α, β) angle pair, and Mueller matrix terms array, this VI generates the corresponding Stokes vectors terms, namely the S_1, S_2 and S_3 terms, and for each wavelength, compute the $T_0(\lambda)$ spectrum using the following equation:

$$T_0(\lambda) = m_{00}(\lambda) S_0 + m_{01}(\lambda) S_1 + m_{02}(\lambda) S_2 + m_{03}(\lambda) S_3$$

Furthermore, the opposite/orthogonal spectrum, $T_0'(\lambda)$, using the inverse of the Stokes vectors used beforehand, namely $-S_1$, $-S_2$ and $-S_3$ is also computed. Upon completion of the simulation of these two spectra, the normalized difference value, ξ, is computed and returned to the calling VI for analysis.

The code of the Compute T0 array (most orthogonal) VI is shown at this end of the chapter, the Front Panel and Block Diagram are each shown on a single page in landscape format. Although more suited for electronic viewing, this code shows the flow of a given input Mueller matrix data set to the final orthogonal $T_0(\lambda)$ and $T_0'(\lambda)$ spectrum and corresponding normalized difference value, ξ. The algorithm in pseudo-code can be viewed in Algorithm 5.

Algorithm 5 Normalized difference for T_0 and T_0' for given (α, β) algorithm

```
Using (α,β) angle pair compute the S1, S2 and S3 Stokes vector terms
for each λ-step (λi)
Extract the m00(λi), m01(λi), m02(λi) and m03(λi)
Using T0(λ) = m00(λ)S0 + m01(λ)S1 + m02(λ)S2 + m03(λ)S3:
    ▷ Compute (λi) using S1, S2 and S3
    ▷ Compute T0'(λi) using -S1, -S2 and -S3
end
Using T0(λi) and T0'(λi) compute normalized difference
```

D.4 Numerical solution program

Main subroutine called by the analysis client for both the passive die screening data and responsivity measurement obtained by using the dBm Optics CSA unit. This VI called **Numerical Solution.VI** shows how by only using the input Mueller matrix terms, we can use the built-in LabVIEW eigenvalues solver to extract three eigenvectors and corresponding eigenvalues to solve our matrix equation system, as described in Section 4.4.3 on page 65.

This VI generates the six M_{ij} terms necessary to build the square symmetric matrix, $\mathbf{M}$, as seen in the following equation:

$$\psi = \begin{bmatrix} S_1 & S_2 & S_3 \end{bmatrix} \begin{bmatrix} M_{11} & M_{12} & M_{13} \\ M_{21} & M_{22} & M_{23} \\ M_{31} & M_{32} & M_{33} \end{bmatrix} \begin{bmatrix} S_1 \\ S_2 \\ S_3 \end{bmatrix} = \vec{S}^T \mathbf{M} \vec{S}$$

The eigenvector with the largest eigenvalue is chosen as it maximizes the difference between the spectra obtained from orthogonal Stokes vectors. An extra normalization step is added to ensure the same vector orientation is used and the length of the SoP_1 and opposite SoP_2 Stokes vectors are scaled to be of unit length, so that they fall upon the surface of the Poincaré sphere.

The code of the Numerical Solution VI is shown at this end of the chapter. The reduction in complexity of the Block Diagram shown in the following pages, in landscape format, should be evident, when compared to other criterion software implementations shown previously. The more advanced sub-routines used, such as the EigenValue and Vectors VI, help reduce the clutter of the main VI and ease software maintenance.

Although more suited for electronic viewing, this code shows the flow of a given input Mueller matrix data set, the creation of the matrix $\mathbf{M}$ and the extraction of the eigenvectors and eigenvalues, prior to the final assignment of the SoP_1 incident Stokes vectors. The algorithm in pseudo-code can be viewed in Algorithm 6.

Algorithm 6 Numerical solution evaluation algorithm

```
Set SoP_1 to nul vector as default
Read (*.raw) data file and parse frequency array and Mueller matrix
if Mueller matrix non-empty

    Compute M_11, M_12, M_13, M_22, M_23 and M_33 terms
    Build square symmetric M matrix

else, quit program and return error
Find eigenvalue and eigenvectors of M
Find largest eigenvalue

    Select eigenvector with corresponds to largest eigenvalue

Normalize eigenvector to have unit length %on surface of Poincaré sphere

    SoP_1 = normalized eigenvector

if S_3 < 0 % assign SoP_1 to southern hemisphere of Poincaré sphere

    SoP_1 = -SoP_1

else, do nothing
```

Analysis Client Software
P:\My Documents\Software\Labview programs\Analysis and File Moving\Analysis Client Program\Version 4.72\Analysis Client Software.vi
Last modified on 05/04/2004 at 1:21 PM
Printed on 05/04/2004 at 5:38 PM

Page 1

Analysis Client Software
P:\My Documents\Software\Labview programs\Analysis and File Moving\Analysis Client Program\Version 4.72\Analysis Client Software.vi
Last modified on 05/04/2004 at 1:21 PM
Printed on 05/04/2004 at 5:38 PM

Page 2

Block Diagram

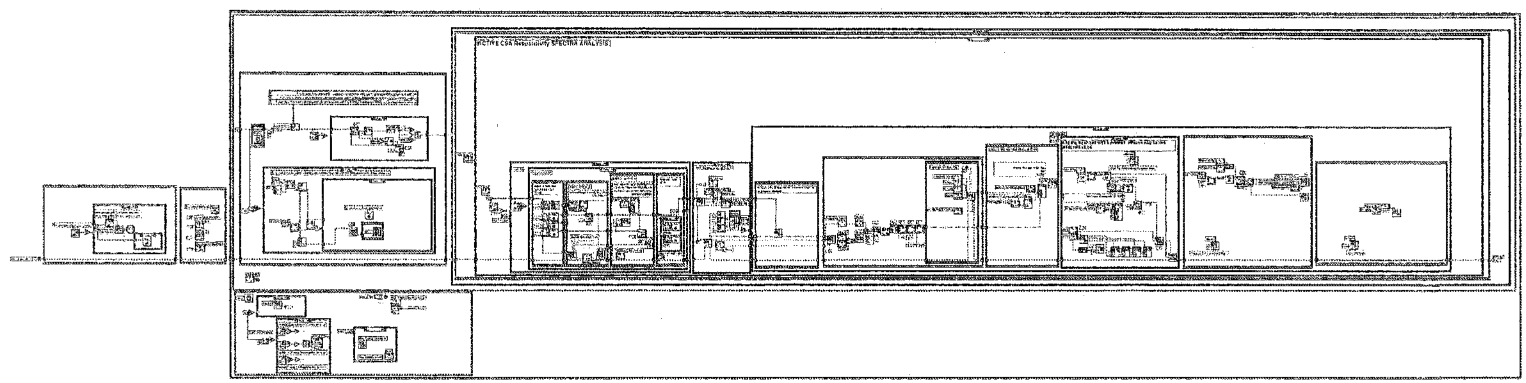

Main PDLambda Analysis (tracking IL and fc).vi
P:\My Documents\Software\Labview programs\PDlambda with Mueller\SWS PDLambda Analysis\Version 1.5\Main PDLambda Analysis (tracking IL and fc).vi
Last modified on 05/04/2004 at 11:56 AM
Printed on 05/04/2004 at 5:34 PM

Front Panel

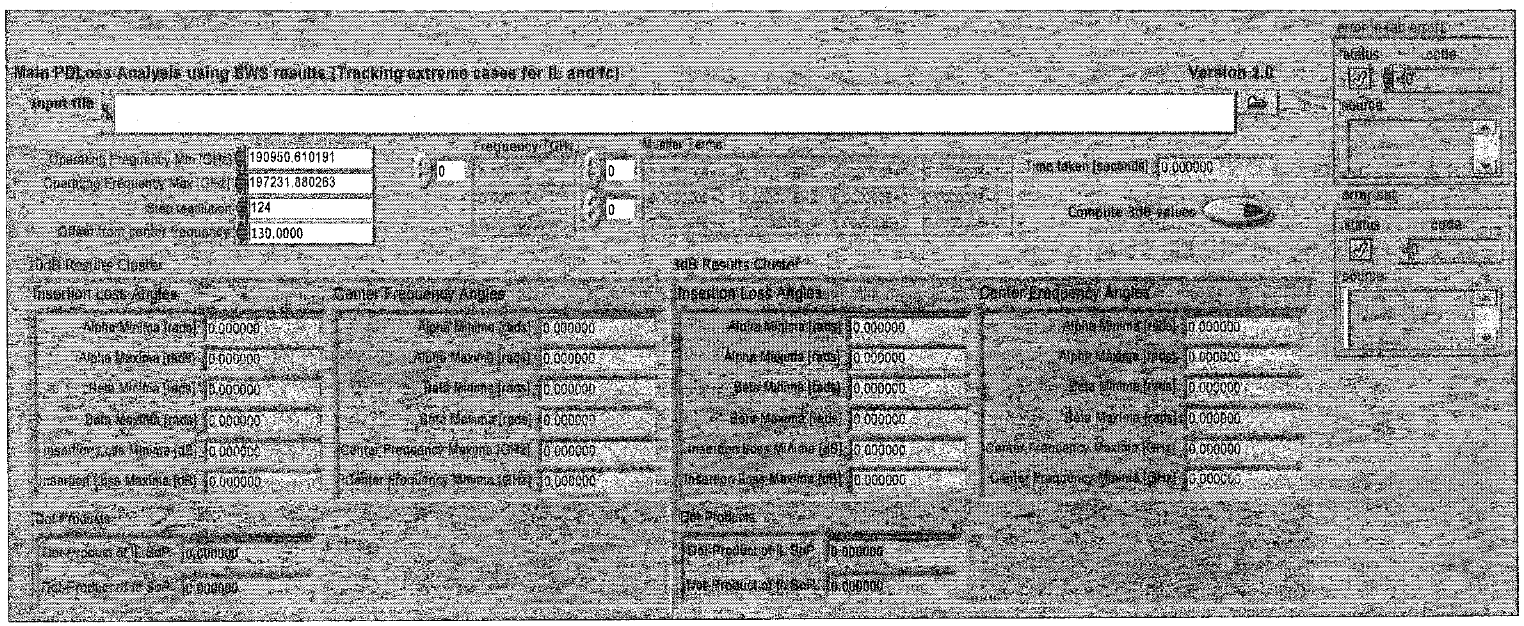

Main PDLambda Analysis (tracking IL and fc).vi
P:\My Documents\Software\Labview programs\PDlambda with Mueller\SWS PDLambda Analysis\Version 1.5\Main PDLambda Analysis (tracking IL and fc).vi
Last modified on 05/04/2004 at 11:56 AM
Printed on 05/04/2004 at 5:34 PM

Page 2

Main PDLambda Analysis (tracking IL and fc).vi
P:\My Documents\Software\Labview programs\PDlambda with Mueller\SWS PDLambda Analysis\Version 1.5\Main PDLambda Analysis (tracking IL and fc).vi
Last modified on 05/04/2004 at 11:56 AM
Printed on 05/04/2004 at 5:34 PM

Page 3

Block Diagram

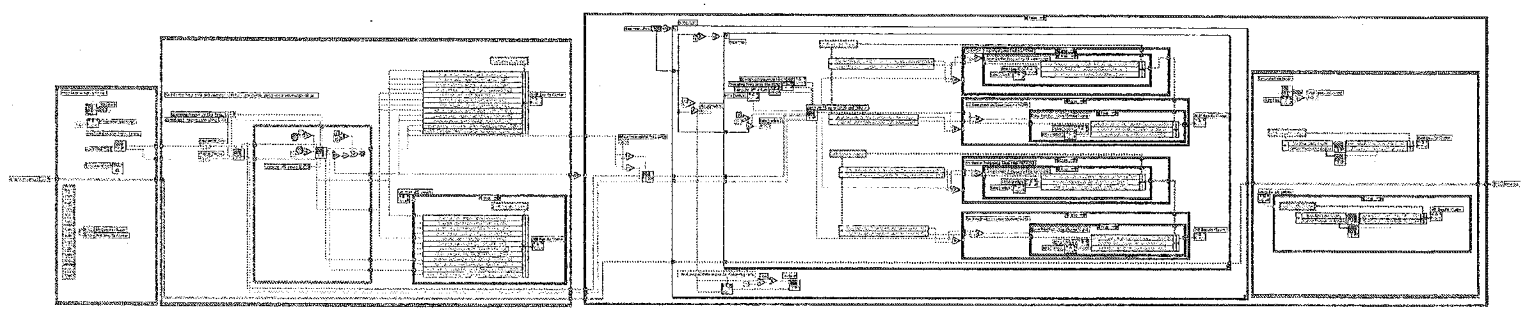

Main Optical Analysis (most orthogonal).vi
P:\My Documents\Software\Labview programs\PDlambda with Mueller\SWS PDLambda Analysis\Version 1.5\Main Optical Analysis (most orthogonal).vi
Last modified on 27/02/2003 at 1:39 PM
Printed on 05/04/2004 at 5:21 PM

Front Panel

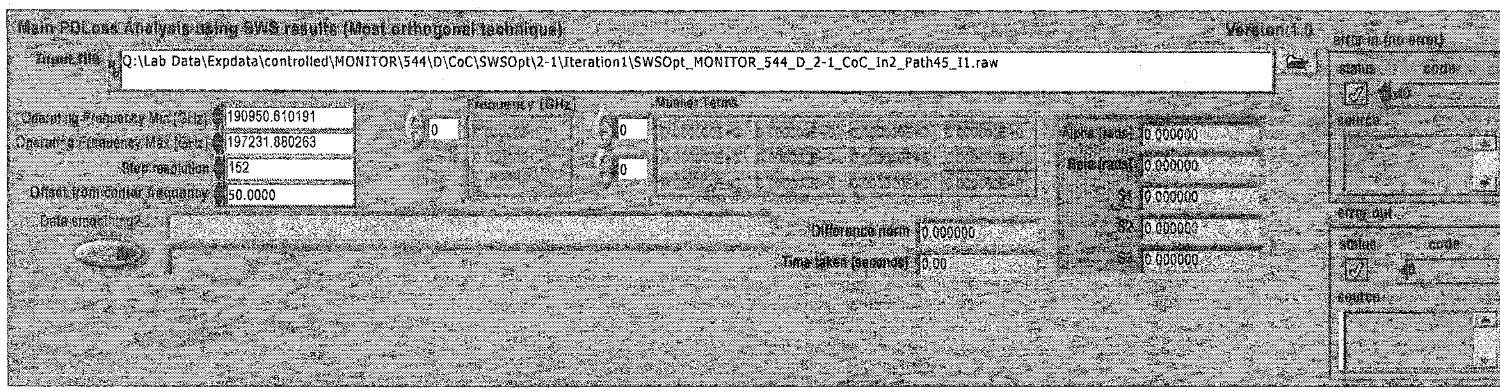

Block Diagram

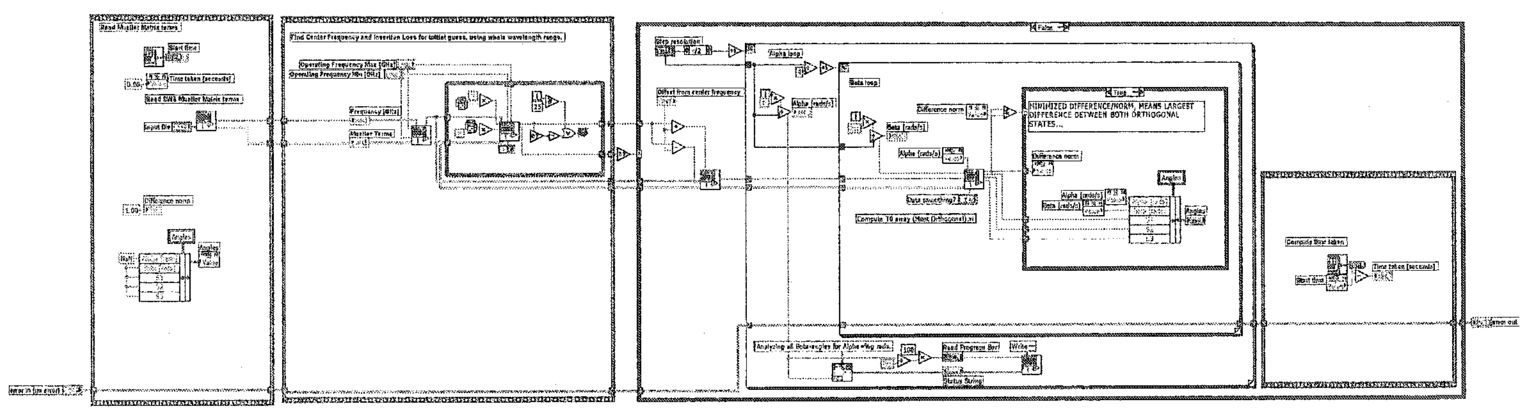

Compute T0 array (Most Orthogonal).vi
P:\My Documents\Software\Labview programs\PDlambda with Mueller\SWS PDLambda Analysis\Version 1.5\subVIs\Compute T0 array (Most Orthogonal).vi
Last modified on 05/04/2004 at 5:22 PM
Printed on 05/04/2004 at 5:30 PM

Front Panel

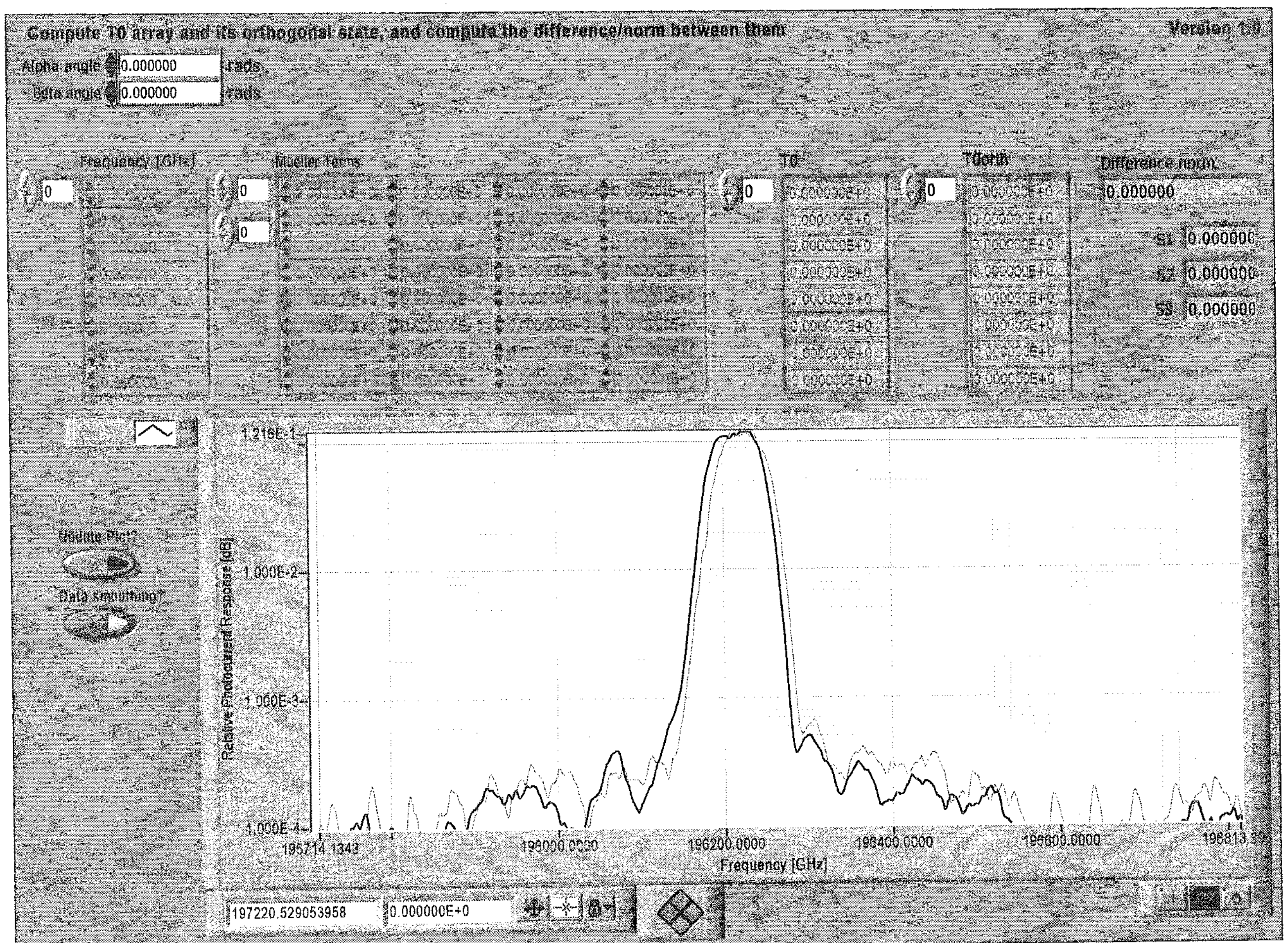

Page 2

Compute T0 array (Most Orthogonal).vi
P:\My Documents\Software\Labview programs\PDlambda with Mueller\SWS PDLambda Analysis\Version 1.5\subVIs\Compute T0 array (Most Orthogonal).vi
Last modified on 05/04/2004 at 5:22 PM
Printed on 05/04/2004 at 5:30 PM

Block Diagram

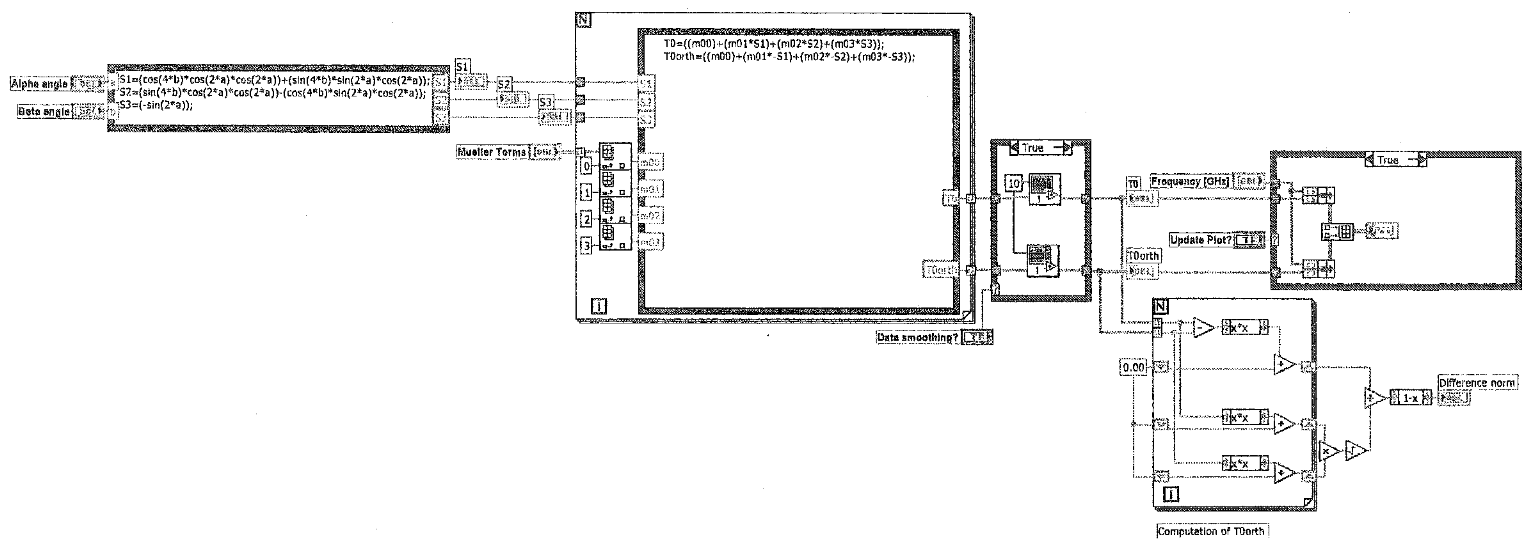

Page 1

Numerical Solution.vi
P:\My Documents\Software\Labview programs\PDlambda with Mueller\SWS PDLambda Analysis\Version 1.5\subVIs\Numerical Solution.vi
Last modified on 02/04/2004 at 9:15 AM
Printed on 05/04/2004 at 5:23 PM

Front Panel

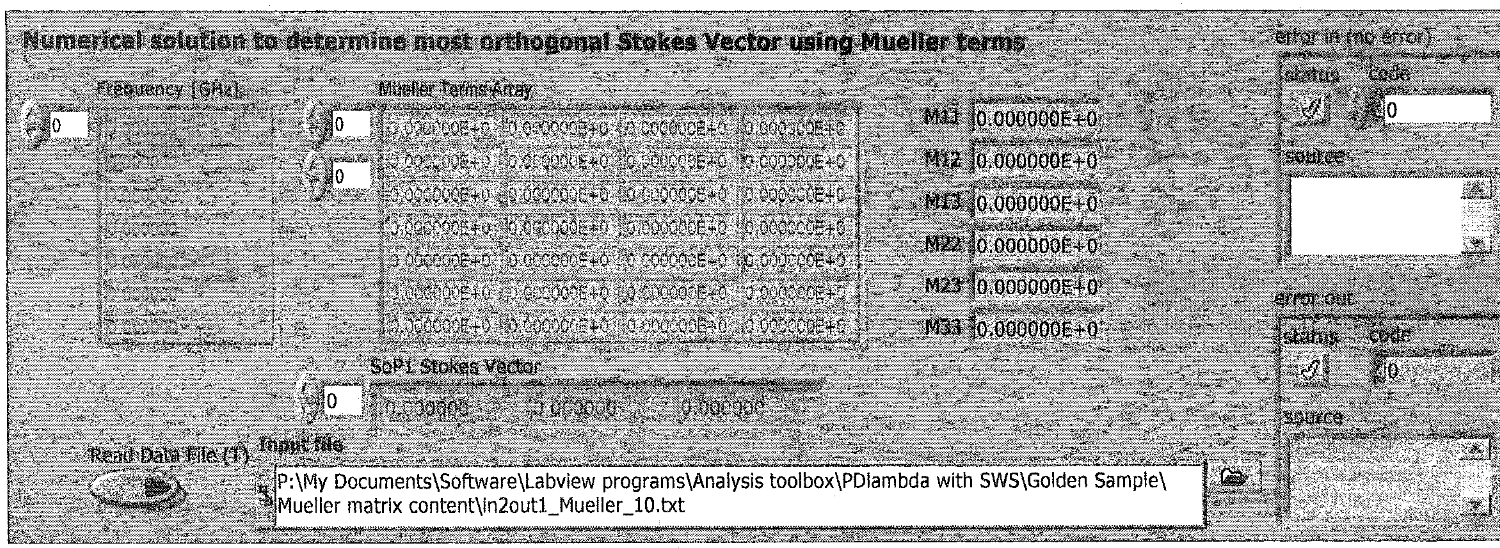

Block Diagram

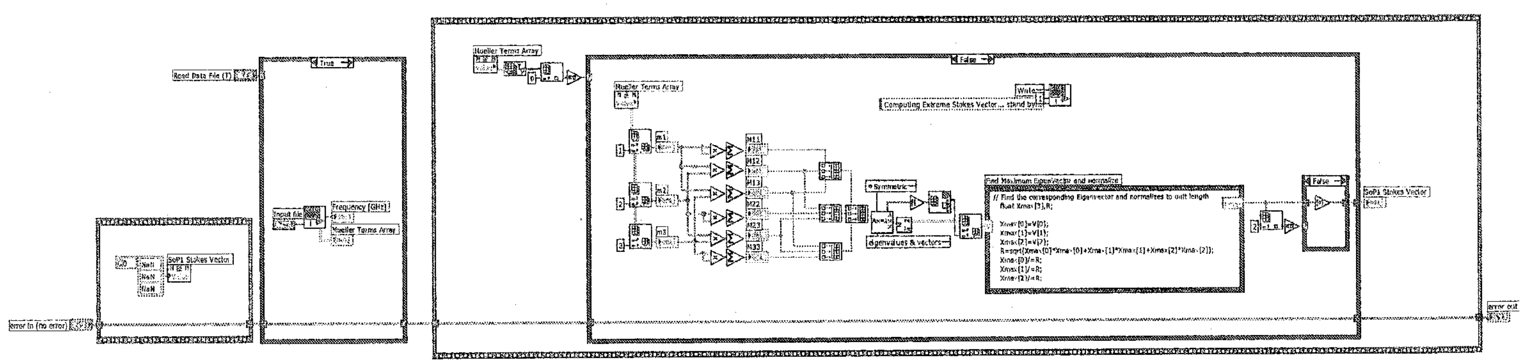

Appendix E

MetroPhotonics Inc. SurePath^{TM} portfolio data sheets and application notes

The following pages include some of the data sheets and application notes for the SurePath^{TM} portfolio and associated electronics discussed throughout the body of this document. More details can be found on the MetroPhotonics Inc. website (31).

List of documents included:

- ▷ SurePath Monitor^{TM} data sheet, from (32).
  - ⇒ Four pages, printed in landscape format
- ▷ SurePath Monitor^{TM} Evaluation fixture data sheet, from (33).
  - ⇒ Two pages, printed in landscape format
- ▷ SurePath Monitor^{TM} Controller data sheet, from (34).
  - ⇒ Two pages, printed in landscape format

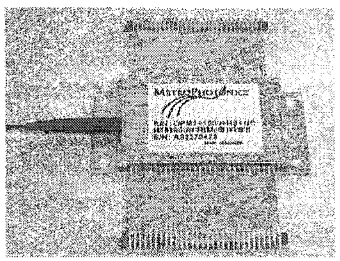

VOLUME PRODUCTION

SurePath Monitor™

Transforming Power Monitoring Economics

100GHz C-BAND

The MetroPhotonics SurePath Monitor™ redefines the network cost economics of optical power monitoring with an innovative, monolithically integrated planar lightwave circuit.

This unique solution introduces new, cost effective applications for power monitoring throughout Access, Metro and Long-Haul Networks. With this optical power monitoring solution carriers will achieve advanced quality of service and network management capability without a significant shift in capital and operational expenditures.

MetroPhotonics' SurePIC™ technology leverages the integration of Indium Phosphide material and Echelle Grating design to produce the industry's smallest footprint, lowest power consumption and fastest response times whilst standard semiconductor techniques provide a cost reduction to OEM's and Carriers.

Key Features

- Low Cost
- Small Footprint & Low Profile
- Fast Response Time
- Designed for 100GHz Spacing
- Available on 25GHz and 50GHz Offsets
- Low Power Consumption

Applications

- Power Monitoring at All Network Nodes
- Direct Integration with EDFA's, OADM's and other Network Elements
- PMD compensation

Performance

- 20ns Detector Response Time
- Max. 1.5W Power Consumption
- Channel Power Accuracy of ±0.5dB
- Power Range of -40dBm to 0dBm

V2-10.21.03

SUREPATH MONITOR™ – 100GHz C-BAND

Specifications

Parameter	Specification	Comments
Channels Detected	43	
Channel Spacing	100GHz	
Wavelength Range	1528.77 to 1562.23nm	
Channel Power Excursion	15dB	Max. power between channels
Input Power Range	-40dBm to 0dBm	Per channel
Power Error (Relative Accuracy)	±0.5dB	Over ITU passband, including PDL
Response Time	20ns	Rise time of detector from 10% to 90% of the input signal
Return Loss	35dB	
Power Consumption	1.5W	Over operating temperature range (Cold start power may be higher)
Temperature Sensor	1kW RTD	Alarm & Control
Operating Temperature	-5°C to 70°C	
Storage Temperature	-40°C to +85°C	
Dimensions: Discrete Package	58.00 x 28.70 x 8.00mm	Includes mounting brackets
Discrete Package with Heatsink	58.00 x 28.70 x 14.40mm	27.9mm Square Heatsink

Ordering Information

For more information on this or other products, including availability, please contact MetroPhotonics directly using the contact information outlined below.

OPM1 + XXXX + YY + ZZ

Starting Channel of Device	
1875	191.875THz
1900	191.900THz
1925	191.925THz
1950	191.950THz

Heatsink Options	
HS	27.9mm SQ Heatsink 6.4mm High
NO	No Heat Sink Supplied

Connector Format	
NC	No Connectors
FP	FC/SPC
FA	FC/APC
SC	SC/SPC
SA	SC/APC
LC	LC
E2	E2000
MU	MU

All statements, technical information, and recommendations related to the product herein are based upon information believed to be reliable or accurate. No responsibility is assumed for inaccuracies. The user assumes all risks and liability whatsoever in connection with the use of a product or its application. MetroPhotonics reserves the right to change at any time without notice the design, materials, processes specifications, function, fit, and form of the products described herein. MetroPhotonics further reserves the right to withdraw at any time said product offered for sale herein. MetroPhotonics makes no representations that the products herein are free from any intellectual property claims of others.

© 2003 MetroPhotonics Inc. MetroPhotonics is a registered trademark and the MetroPhotonics logo is a trademark of MetroPhotonics Inc.

V2-10.21.03

MetroPhotonics Inc., 1887 St. Joseph Blvd., Ottawa, Ontario, Canada K1C 7J2
Tel: 613 834 0035 Fax: 613 834 4891 sales@metrophotonics.com www.metrophotonics.com

SurePath Monitor™ – 100GHz C-Band

Mechanical Drawing

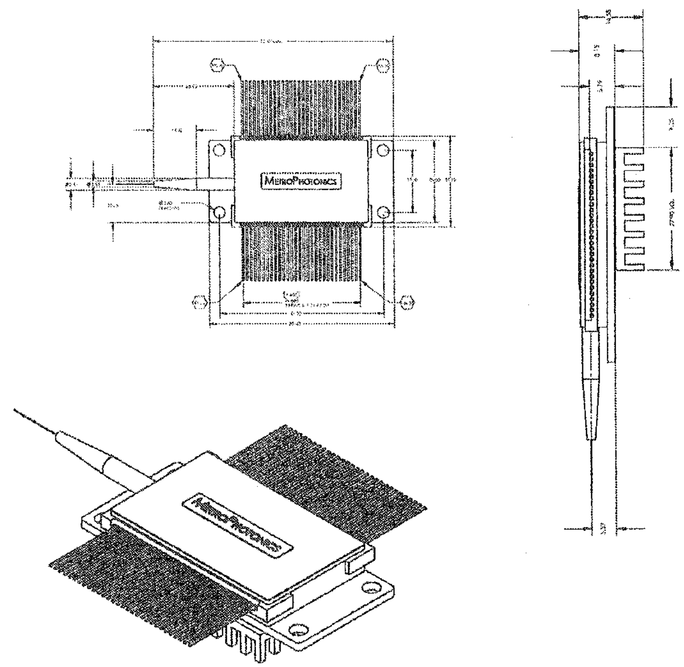

V2-10.21.03

DATA SHEET

SurePath Monitor™ – 100GHz C-Band

Pin Assignment

Pin	Assignment	Pin	Assignment	Pin	Assignment
1	Common C1	21	WPD Drive 3	41	WPD Drive 41
2	WPD Drive 22	22	WPD Drive 2	42	WPD Drive 40
3	WPD Drive 21	23	WPD Drive 1 [1]	43	WPD Drive 39
4	WPD Drive 20	24	Package Ground [3]	44	WPD Drive 38
5	WPD Drive 19	25	Control Sensor +ve	45	WPD Drive 37
6	WPD Drive 18	26	Control Sensor +ve	46	WPD Drive 36
7	WPD Drive 17	27	Control Sensor –ve	47	WPD Drive 35
8	WPD Drive 16	28	Control Sensor –ve	48	WPD Drive 34
9	WPD Drive 15	29	N/C	49	WPD Drive 33
10	WPD Drive 14	30	TEC –ve	50	WPD Drive 32
11	WPD Drive 13	31	TEC +ve	51	WPD Drive 31
12	WPD Drive 12	32	N/C	52	WPD Drive 30
13	WPD Drive 11	33	Alarm Sensor –ve	53	WPD Drive 29
14	WPD Drive 10	34	Alarm Sensor –ve	54	WPD Drive 28
15	WPD Drive 9	35	Alarm Sensor +ve	55	WPD Drive 27
16	WPD Drive 8	36	Alarm Sensor +ve	56	WPD Drive 26
17	WPD Drive 7	37	Package Ground [3]	57	WPD Drive 25
18	WPD Drive 6	38	N/C	58	WPD Drive 24
19	WPD Drive 5	39	WPD Drive 43 [2]	59	WPD Drive 23
20	WPD Drive 4	40	WPD Drive 42	60	Common C2

1. WPD 1 is the highest channel frequency.
2. WPD 43 is the lowest channel frequency.
3. Package Ground Pins are electrically shorted to package body.

CAUTION
STATIC SENSITIVE DEVICE
OBSERVE PRECAUTIONS

All statements, technical information, and recommendations related to the product herein are based upon information believed to be reliable or accurate. No responsibility is assumed for inaccuracies. The user assumes all risks and liability whatsoever in connection with the use of a product or its application. MetroPhotonics reserves the right to change at any time without notice the design, materials, processes, specifications, function, fit, and form of the products described herein. MetroPhotonics further reserves the right to withdraw at any time said product offered for sale herein. MetroPhotonics makes no representations that the products herein are free from any intellectual property claims of others.

© 2003 MetroPhotonics Inc. MetroPhotonics is a registered trademark and the MetroPhotonics logo is a trademark of MetroPhotonics Inc.

V2-10.21.03

MetroPhotonics Inc., 1887 St. Joseph Blvd., Ottawa, Ontario, Canada K1C 7J2
Tel: 613 834 0035 Fax: 613 834 4891 sales@metrophotonics.com www.metrophotonics.com

PRODUCT BULLETIN

METROPHOTONICS

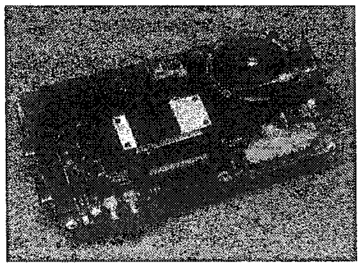

EVALUATION FIXTURE

SurePath Monitor™

100GHz C-Band Optical Performance Monitor with Control Electronics

OPM+EVAL+C01

The SurePath Monitor™ Evaluation Fixture allows customers to rapidly evaluate and assess the MetroPhotonics SurePath Monitor.

- User friendly GUI to customize and evaluate test results in a few minutes
- LabView™ drivers for embedding fixture into existing test-beds
- Incorporates high sensitivity, high speed analog front-end circuitry
- Digital post-processing via embedded firmware for conversion to optical power, including corrections for adjacent and non-adjacent channels under high power excursion
- RS232 Serial Communications port
- TEC control and RTD temperature alarms controlled by the DSP

The Evaluation Fixture provides for two configurations:

- (1) 43-channel power monitoring
- (2) 41-channel monitoring plus two channels direct read (bypass on-board data processing). High speed analog ports allowing the intrinsic response (<5ns) of the photodetector to be exploited for pilot tone /digital overhead extraction.

Key Features of SurePath Monitor

- Low Cost
- Small Footprint
- Channel Power Accuracy of ±0.5dB
- Wide Dynamic Range of −40dBm to 0dBm
- Fast Response Time (<5ns)
- Designed for 100GHz spacing
- Low Power Consumption (1.5W)

Applications of SurePath Monitor

- Power Monitoring at all Network Nodes
- Direct Integration with Network Elements
  - EDFA's
  - ROADM's, etc.
- High Speed Control of Network Elements
  - Dynamic Gain Equalizer
  - Dynamic Channel Equalizer
  - Variable Multiplexer
  - Reconfigurable Add-Drop Multiplexer
  - Optical Cross-connect etc.

V1-08.01.04

PRODUCT BULLETIN

SUREPATH MONITOR™ 100GHZ C-BAND EVALUATION FIXTURE WITH CONTROL ELECTRONICS (OPM + EVAL + C01)

Key Specifications of SurePath Monitor

Parameter	Specification	Comments
Channels Detected	43	
Channel Spacing	100GHz	
Wavelength Range	1528.77 to 1562.23nm	
Channel Power Excursion	15dB	Max. power difference between channels
Input Power Range	-40dBm to 0dBm	Per channel
Power Error (Relative Accuracy)	±0.5dB	Over ITU passband, including PDL
Return Loss	35dB	

Partial Command Set for SurePath Monitor Evaluation Fixture

Fixture Set-up	Power Monitoring
Get Temperature/Set Temperature	Get Corrected Power for Selected Channel
Set Temperature Set-point/Get Temperature Set-point	Get ADC Value for Selected Channel
Get TEC Voltage	Get Corrected Powers for all Channels
Set Crosstalk Calibration Array	Get ADC Values for All Channels
Get Crosstalk Calibration Array	Get Dark Powers for All Channels

Environmental

The SurePath Monitor Evaluation Fixture is designed to accelerate customer evaluation of the SurePath Monitor. While it is assembled and designed for components rated for operation from -5°C to +70°C, it has not been explicitly assessed under varying environmental conditions and as a result degraded performance may be obtained.

Ordering Information

For pricing and delivery information regarding the 100GHz C-band Evaluation Fixture with Control Electronics please contact MetroPhotonics directly and refer to part identity OPM+EVAL+C01 in your communications.

Configuration Options

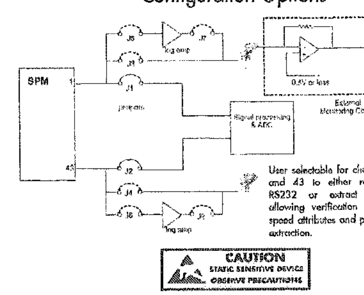

V1-08.01.04

MetroPhotonics Inc., 1887 St. Joseph Blvd., Ottawa ON Canada K1C 7J2
Tel 834 0035 • Fax 613 834 4891 • sales@metrophotonics.com • www.metrophotonics.com

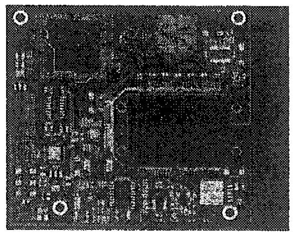

PRELIMINARY

SurePath Monitor™ High Speed Controller SPMc+1HS

The SurePath Monitor™ High Speed Controller provides complete control, interfacing and network reporting for the SurePath Monitor™ optical power monitor. Offered as a physical controller with the optical circuitry or as a reference design, the SPMc+1HS provides an update of all 40+ channels monitored in <5ms.

As such the controller provides supervisory monitoring to the network or direct fast control of network elements. In the latter scenario our solution maintains its accuracy even under excursion ratios of 15dB.

- High sensitivity, high speed analog front-end circuitry
- Digital post-processing via embedded firmware for conversion to optical power, including corrections for adjacent and non-adjacent channels under high power excursion
- Fully integrated temperature management
- RS232 & I²C Serial Communications ports

The SPMc+1HS is available additionally as a Rapid Prototyping Fixture (with GUI + LabView™ drivers) and as a reference design under license for direct integration with customer circuit electronics.

Key Features (in Operation with SurePath Monitor)

- Channel Power Accuracy of ±0.5dB
- Wide Dynamic Range of −40dBm to 0dBm
- Fast Monitoring (<5ms) of 43 Channels
- 100GHz Spacing
- High Channel Power Excursion (15dB)\
- Single +5V Power Rail
- RS232 & I²C Interfaces
- Rapid Module Development

Applications of SurePath Monitor

- Power Monitoring at All Network Nodes
- Direct Integration with Network Elements
  - EDFA's
  - ROADM's etc
- High Speed Control of Network Elements
  - Dynamic Gain Equalizer
  - Dynamic Channel Equalizer
  - Variable Multiplexer
  - Reconfigurable Add-Drop
  - Optical Cross-Connect etc

V1.1-16.02.04

SurePath Monitor™ High Speed Controller SPMc+1HS

Functional Schematic

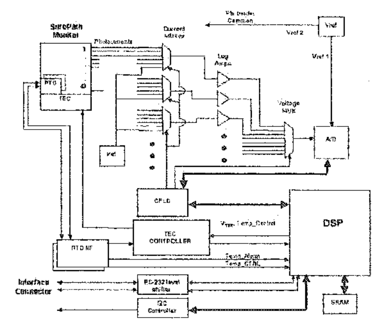

Pin Assignment

Pin	Description	Pin	Description
1	No connect	26	External I²C 5V
2	No connect	27	I²C serial data
3	No connect	28	I²C serial clock
4	No connect	29	No connect
5	Digital ground	30	No connect
6	Digital ground	31	No connect
7	RS232 TxA	32	No connect
8	RS232 TxB	33	No connect
9	RS232 RxA	34	No connect
10	RS232 RxB	35	No connect
11	N/C	36	No connect
12	N/C	37	No connect
13	No connect	38	No connect
14	No connect	39	External 5V
15	No connect	40	External 5V
16	No connect	41	External 5V
17	No connect	42	External 5V
18	No connect	43	External 5V
19	No connect	44	External 5V
20-25	No connect	45-50	Ground

Specifications

Parameter	Specification	Comments
Channels Detected	43	*Note 1
Channel Spacing	100GHz	*Note 1
Wavelength Range	1528.77 to 1562.23nm	*Note 1
Channel Power Excursion	15dB	*Note 1
Input Power Range	-40dBm to 0dBm	*Note 1
Power Error (Relative Accuracy)	±0.5dB	* Note 1
Return Loss	35dB	* Note 1
Dimensions	100x80x16.5mm	With SurePath Monitor heatsink, mounting etc
Power Supply	+5V	
Digital Interface	RS232	Maxim MAX3232 Dual RS-232 Transceiver
	I2C	Atmel Atmega128L-8MI Micro-Controller as Slave

* Note 1 : When assembled and calibrated with MetroPhotonics SurePath Monitor of OPM1 Series

Ordering Information

For pricing and delivery information regarding the SurePath Monitor Controller and the SurePath Monitor optical performance monitor please contact MetroPhotonics directly and refer to part identity SPMc+1HS in your communications.

MetroPhotonics Inc., 1887 St. Joseph Blvd., Ottawa, Ontario, Canada K1C 7J2
Tel: 613 834 0035 Fax: 613 834 4891 sales@metrophotonics.com www.metrophotonics.com

Redaction Notes

This thesis was typeset on both a Sony VAIO PXG-XG39 laptop and a Dell GX400 personal computer, both running Windows 2000 Professional as their main operating system.

Typesetting was performed using MikTex[1] , version 2.4, an implementation of TEX and related programs for Windows on x86 systems. TEX[2] is a typesetting system invented by Donald E. Knuth, to ease the creation of great-looking scientific papers, articles and other types of documents. Numerous add-in packages from CTAN[3] were used.

Text processing was performed using a native-win32 port of LYX[4] maintained by Ruurd Reitsma (version 1.3.3)[5] .

Commercial software packages used include the following:

- ▷ National Instruments' LabVIEW 6.0.2 and 7.0 Express[6] , used for all analysis and control of test and measurement equipment.
- ▷ MathWorks' Matlab 6.1 R12[7] , used for most data plots shown throughout this document.

The actual style of the thesis was largely inspired by the University of Colorado at Boulder LATEX thesis class[8] , version 1.10, released in January 2003, which was then modified to suit the University of Ottawa regulations.

I wish to express my heartfelt appreciation for the great work performed by all those involved in the maintenance and continued innovations found in all the above mentioned software. I could not have created this document nor the software used throughout this project in such an efficient fashion without all these tools.

I also wish to thanks all registered members of the **lyx-users@lists.lyx.org** mailing list for their help in debugging LATEX and LYX idiosyncrasies[9] .

---

[1] For more information, visit http://www.miktex.org
[2] For more information, visit http://www-cs-faculty.stanford.edu/~knuth/
[3] For more information, visit http://www.ctan.org
[4] For more information, visit http://www.lyx.org
[5] For more information, visit http://www.home.zonnet.nl/rareitsma/lyx
[6] For more information, visit http://www.ni.com/labview
[7] For more information, visit http://www.mathworks.com
[8] For more information, visit http://www.colorado.edu/ITS/docs/latex/thesis
[9] For mailing list archives, visit http://www.mail-archive.com/lyx-users@lists.lyx.org/